Adaptive planning strategies for MR-guided HDR prostate brachytherapy using a single needle MR-compatible robotic system

Maxence Borot de Battisti

Adaptive planning strategies for MR-guided HDR prostate brachytherapy using a single needle MR-compatible robotic system
PhD thesis, Utrecht University, The Netherlands

The research described in this thesis was performed at the Department of Radiotherapy of the University Medical Center Utrecht

Manuscript
Cover image: "Cercles dans un cercle" by Wassily Kandinsky (1923)
Cover layout: Proefschriftmaken
Cover idea: Adeline Borot and Maxence Borot de Battisti
Thesis layout: Maxence Borot de Battisti
Typeset in: LaTeX
Printed by: Proefschriftmaken

Financial support for this research was provided by Philips Medical Systems Nederland B.V. Printing of this thesis was financially supported by Nucletron (Elekta) and CIRS.

Adaptive planning strategies for MR-guided HDR prostate brachytherapy using a single needle MR-compatible robotic system

Strategieën voor het adaptief plannen van MR-geleide HDR prostaat brachytherapie met behulp van een MR-compatibel robotsysteem met een enkele naald

(met een samenvatting in het Nederlands)

Proefschrift

ter verkrijging van de graad van doctor aan de Universiteit Utrecht op gezag van de rector magnificus, prof. dr. G.J. van der Zwaan, ingevolge het besluit van het college voor promoties in het openbaar te verdedigen op vrijdag 20 oktober 2017 des middags te 2.30 uur

door

Maxence Etienne Pierre Marie Borot de Battisti
geboren op 1 november 1988 te Échirolles, Frankrijk

Promotor:	Prof. dr. ir. J.J.W. Lagendijk
Copromotoren:	Dr. ir. M.A. Moerland Dr. B. Denis de Senneville

Contents

List of acronyms

DVH Dose-Volume Histogram

FBG Fiber Bragg Grating

FIDO Fast Inverse Dose Optimization

HDR High Dose Rate

IGABT Image Guided Adaptive Brachytherapy

IPSA Inverse Planning Simulated Annealing

LDR Low Dose Rate

MRTR MR-TRacking

OAR Organ At Risk

OARs Organs At Risk

OSS Optical Shape Sensing

PSA Prostate Specific Antigen

PTV Planning Target Volume

TRUS TransRectal UltraSound

UMCU University Medical Center Utrecht

CHAPTER 1

Introduction

1.1 Prostate Cancer

Prostate cancer is one of the most commonly diagnosed male cancer in Europe and United States (Ferlay *et al* 2015, Siegel *et al* 2017). According to the World Cancer Research Fund International, more than 1.1 million cases of prostate cancer were recorded in 2012, accounting for around 8% of all new cancer cases and 15% in men. Furthermore, 161.360 new cases of invasive cancer and 26.730 estimated deaths are expected in 2017 in the United States. The number of accurately diagnosed prostate cancers tremendously increased in the recent years and this is largely because of the increased availability of screening for Prostate Specific Antigen (PSA) in men without symptoms of the disease. This test leads to the detection of many prostate cancers that are small and/or would otherwise remain unrecognized, and which may or may not develop further into higher stage disease (Loeb *et al* 2014).

1.2 MRI in prostate cancer

Visualization is important in the process of diagnosis, treatment and follow-up of prostate cancer. Thanks to its superior soft tissue contrast, the prostate and surrounding critical structures can be better discriminated using MRI compared to other imaging modalities such as ultrasound, or CT. Moreover, patients are not exposed to ionizing radiation during MRI examination. More recently, multiparametric-magnetic resonance imaging (mp-MRI) has shown promising results in diagnosis, localization, risk stratification and staging of clinically significant prostate cancer (Atalar and Ménard 2005, Groenendaal *et al* 2010). It has also opened up opportunities for focal therapy of prostate cancer, where the treatment is directed to the area of cancer and nearby tissue. By avoiding damage to the whole prostate, the risk of damage to the surrounding nerves, muscles, urinary sphincter, bladder, and rectum is greatly reduced. Multiple institutes intend to perform or are performing diagnostic and treatment interventions inside the MR scanner to have online MRI during the intervention. For example in external beam radiotherapy, special MR scanners are integrated with linear accelerators or cobalt sources to achieve this goal (Lamey *et al* 2010, Raaymakers *et al* 2006, Kron *et al* 2006). Other minimally invasive treatments, such as cryoablation, laser ablation and high intensity focused ultrasound are also currently being investigated for introduction into clinic.

1.3 Prostate brachytherapy

Different treatment possibilities are available for prostate cancer and the effectiveness depends, among other factors, on the tumour stage. For early stage prostate cancer, possible treatment options are radical prostatectomy, external beam radiation, and brachytherapy. Brachytherapy consists in the internal irradiation of the tumour with radioactive sources. Due to the sharp dose gradient, a high tumor dose may be delivered while minimizing exposure to the surrounding organs at risk (urethra, bladder and rectum). The two major methods of prostate brachytherapy

are (1) permanent Low Dose Rate (LDR) seed implantation and (2) temporary High Dose Rate (HDR) brachytherapy.

1.3.1 LDR vs. HDR brachytherapy

LDR prostate brachytherapy consists in the permanent placement of radioactive seeds (usually containing Iodine-125 or Palladium-103) in close proximity to the target, using typically needles or plastic catheters to insert the radioactive sources. LDR brachytherapy is often implemented in patients with low risk prostate cancer (Guedea *et al* 2010). Composed of 40-100 seeds, the implant emits radiation in the prostate at an energy of typically 28.37 KeV for Iodine-125 and 20.74 keV for Palladium-103. The intensity of the implant decreases over time, with a half-life of 59.4 days for Iodine-125 and 17.0 days for Palladium-103 (Rivard *et al* 2004).

In HDR brachytherapy, catheters are implanted into or close to the target, and a single, small (1 mm diameter and 4.5mm length), high-activity source (usually constituted of Iridium-192) that is attached with a steel wire to the afterloader, is temporarily placed inside the body through the implanted catheters. The source is remotely controlled by the afterloading device: It steps through the catheters to predefined positions (dwell positions) and remains in these dwell positions for a pre-calculated amount of time (dwell time). After delivery of the prescribed dose, the radioactive source is retracted back into the shielded safe. An important dosimetric advantage of a stepping source brachytherapy treatment is the possibility to optimize the dose distribution using different times in the dwell positions.

Whole-gland LDR brachytherapy is often implemented clinically in patients with favorable risk prostate cancer since it is a minimally invasive procedure with good long-term clinical outcomes (Zelefsky *et al* 2007, Henry *et al* 2010, Hinnen *et al* 2010, Chin *et al* 2017). However, toxicity such as acute urinary retention remains a concern with this treatment modality (Stone and Stock 2002, Roeloffzen *et al* 2011). To reduce toxicity in patients with localized prostate carcinoma, focal treatment has gained increasing interest as an alternative to whole-gland therapy. This may be achieved with focal HDR brachytherapy (Banerjee *et al* 2015).

1.3.2 Current practice of focal HDR prostate brachytherapy

In the current practice of focal HDR prostate brachytherapy for localized prostate cancer, catheters are inserted manually under TransRectal UltraSound (TRUS) guidance in a parallel configuration with the support of a template brachytherapy grid (Hoskin *et al* 2013). After completion of the implant procedure, needle reconstruction, dose planning and needle position verification are assessed using TRUS, CT or MRI (Figure 1.1). The dose delivered cannot be measured directly: the dose deposition relies on model-based dose calculation methods (Beaulieu *et al* 2012) which requires, as input, tumor, Organs At Risk (OARs), needle and source localization.

This procedure is not optimal for several reasons. First, errors in the delivered

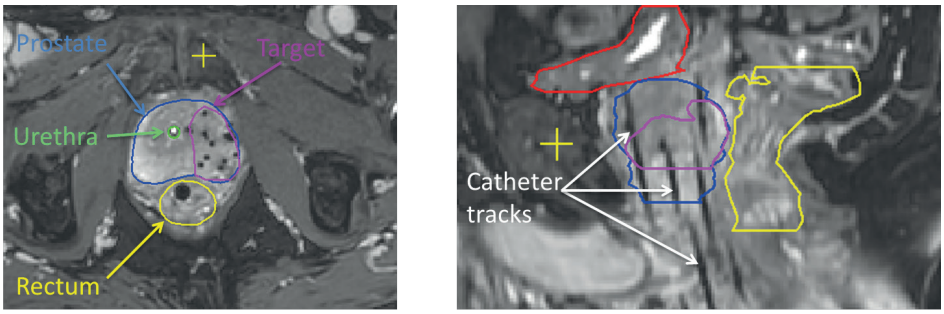

Figure 1.1: Transverse and sagital MRI of a patient after completion of the implant procedure.

dose can occur due to two unpredictable events as follows:

1. **Needle positioning errors**: US-guided manual insertion of needles may lead to sub-optimal needle configurations due to the shadowing effect behind the implant needles which decreases the image quality.

2. **Intra-operative internal organ motion** such as swelling, displacement (Stone *et al* 2002) or rotation (Lagerburg *et al* 2005) of the prostate (related to the trauma caused by the needle insertion) or intra-procedural changes in rectum or bladder filling may also induce errors in the deposited dose.

Second, the procedure can be relatively time consuming ($\sim$ few hours) if two imaging modalities are used (TRUS for insertion of the needle and CT or MRI for the needle reconstruction). Consequently, a complete MR-guided focal HDR prostate brachytherapy procedure is currently being investigated.

1.4 MRI-brachytherapy hybrid system

Although MRI presents advantages for prostate brachytherapy, there are also some difficulties. In particular, the major issue in MRI-guided procedures is the limited space inside the closed bore which prevents the manual needle insertion. Therefore, to enable HDR prostate brachytherapy treatment under MR-guidance, MR-compatible robotic methods have been developed in several institutes (Muntener *et al* 2006, Fischer *et al* 2007 and 2008 and DiMaio *et al* 2007). These systems have to deal with technical difficulties, such as the restriction to use only non-ferromagnetic materials.

At the University Medical Center Utrecht (UMCU), a novel hybrid system, which combines a 1.5T MR scanner and a brachytherapy robotic device to support needle insertion in the MR bore (Figure 1.2) is currently being developed (Van den Bosch *et al* 2010). With this system, the anatomy and needle can be visualized in

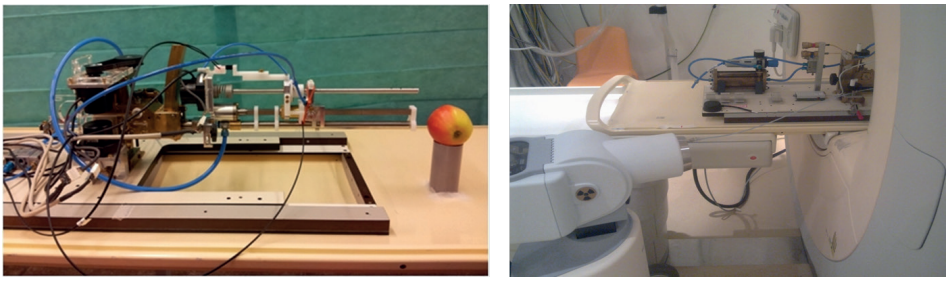

Figure 1.2: Pictures of the robotic device which supports needle insertion in the MR-bore.

real-time with MRI, during the HDR brachytherapy intervention. This hybrid system may change drastically the interventional paradigm in brachytherapy since it allows accurate needle guidance and monitoring of the changing patient anatomy during treatment. A planning system should be developed that accommodates the continuous update of changing anatomy and accumulation of dose. Furthermore, the treatment time may reduce since MRI is the only imaging device used during the intervention. The robot is made of polymers and non-ferromagnetic materials, such as copper, titanium and aluminum. It has five degrees of freedom: four passive and one active (the needle insertion). Placed between the legs of the patient, the robot inserts the needle transperineally under MR-guidance into the prostate. Due to limited space in the MR-bore, the needle is inserted in a divergent configuration (i.e. under different angles with a point of rotation situated at the perineum). That way, the dose is delivered needle-per-needle. Moreover, a tapping mechanism is used for needle insertion to restrict prostate movement and tissue deformation (Lagerburg *et al* 2006).

The ultimate goal is therefore to develop a fully automatic control system, where the dose plan and the needle insertion sequence are re-optimized during the intervention according to the two aforementioned perturbations (needle positioning errors and intra-operative internal organ motion). This fully automatic control system would require (1) to localize accurately the tumor and OARs (those can be provided by the MRI), (2) to localize accurately the needle with MRI or other MR compatible localization methods such as fiber Bragg gratings-based technology (Borot de Battisti 2016b), (3) to calculate and update the dose plan and (4) the needle insertion sequence during the procedure.

1.5 Outline of thesis

The goal of this thesis is to make a step toward a fully automatic control system, where the dose plan and the needle insertion sequence are re-optimized during the intervention.

In **chapter 2**, a fast optimization planning method is proposed for this MR-brachytherapy setup with divergent needle configuration. The parameters which

are optimized in order to determine the optimal dose plan are (1) the center of rotation of the setup, (2) the angulations of the needle tracks, (3) the dwell positions and (4) the dwell times. The proposed algorithm is then assessed in a planning study on 10 patients.

In **chapter 3**, a pipeline is proposed to update the dose plan with feedback on the needle positioning errors. A dose plan is made at the beginning of the interventional procedure and updated after each needle insertion to compensate for possible needle deviations. The proposed feedback strategy is evaluated by simulating HDR prostate brachytherapy involving needle-by needle dose delivery on 8 patients.

In **chapter 4**, a prototype system for needle tracking based on fiber Bragg gratings (FBG) sensing is investigated: the system involves a MR-compatible stylet composed of three optic fibers with nine sets of embedded FBG sensors each. This stylet can be inserted into brachytherapy needles and allows a fast measurement of the needle deflection. In this study, we assess the potential of FBG-based sensing for real-time needle (including catheter or tube) tracking during MR-guided intervention.

In **chapter 5**, a new automatic needle sequencing strategy for MR-guided HDR prostate brachytherapy is proposed. The sequencing strategy involves inserting each needle into the most sensitive (in terms of the impact of positioning errors on dose distribution) needle track. To predict track sensitivities, a stochastic method based on needle insertion simulations is used. The proposed sequencing strategy is then assessed by simulating of HDR prostate brachytherapy involving needle-by needle dose delivery on 11 patients.

In **chapter 6**, a new paradigm is investigated for intrafraction update of the dose plan and sequence, based on incoming anatomy deformations from MRI. The proposed strategy is evaluated by verifying if, given a set of anatomy deformations during treatment, the prescribed dose can be delivered to the target while minimizing the dose to the surrounding structures: For this purpose, MR-guided HDR prostate brachytherapy performed with the UMCU robotic set-up is simulated on 15 patients, where intrafraction motion is mimicked.

Chapter 7 discusses the impact of the various studies of the thesis and the future application of the MR-brachytherapy hybrid system.

CHAPTER 2

An automated optimization tool for high-dose-rate (HDR) prostate brachytherapy with divergent needle pattern

The following chapter is based on:
Borot de Battisti M, Maenhout M, Denis de Senneville B, Hautvast G, Binnekamp D, Lagendijk J J W, Van Vulpen M and Moerland M A 2015 An automated optimization tool for high-dose-rate (HDR) prostate brachytherapy with divergent needle pattern *Phys. Med. Biol.* **60** 7567–83

Abstract

Focal HDR for prostate cancer has gained an increasing interest as an alternative to whole gland therapy as it may contribute to reduction of treatment related toxicity. For focal treatment, optimal needle guidance and placement is warranted. This can be achieved under MR guidance. However, MR-guided needle placement is currently not possible due to space restrictions in the closed MR bore. To overcome this problem, a MR-compatible, single-divergent needle-implant robotic device is under development at the UMCU: placed between the legs of the patient inside the MR bore, this robot will tap the needle in a divergent pattern from a single rotation point into the tissue. This rotation point is just beneath the perineal skin to have access to the focal prostate tumor lesion. Currently, there is no treatment planning system commercially available which allows optimization of the dose distribution with such needle arrangement. The aim of this work is to develop an automatic inverse dose planning optimization tool for focal HDR prostate brachytherapy with needle insertions in a divergent configuration. A complete optimizer workflow is proposed which includes the determination of (1) the position of the center of rotation, (2) the needle angulations and (3) the dwell times. Unlike most currently used optimizers, no prior selection or adjustment of input parameters such as minimum or maximum dose or weight coefficients for treatment region and organs at risk is required. To test this optimizer, a planning study was performed on 10 patients (treatment volumes ranged from $8.5cm^3$ to $23.3cm^3$) by using 2 to 14 needle insertions. The total computation time of the optimizer workflow was below 20 minutes and a clinically acceptable plan was reached on average using only four needle insertions.

2.1 Introduction

Focal-HDR has gained an increasing interest as an alternative to whole-gland therapy in patients with localized prostate cancer. Focal therapy aims at reducing treatment related side effects and toxicity (Pieters *et al* 2009). The success of focal therapy will depend on the efficiency of tumour localization and dose delivery. Imaging, pathology and dose delivery studies have shown the value of multi-parametric MR-imaging for tumour localization (Groenendaal *et al* 2010). Furthermore, Polders *et al* (2015) showed an adequate dose coverage is obtained if a 5 mm margin is applied to the MR based tumour delineations. Therefore, a MR-guided focal-HDR procedure is under investigation. In the daily practice at the UMCU, needles are inserted under ultrasound guidance while needle reconstruction, dose planning and needle position verification are based on MRI. For optimal MR guidance during therapy, needle insertion should also be under MR guidance, which is not currently possible due to access restrictions in a closed MR-bore system. To enable MR-guided needle insertion in the space restricted MR

environment, MR-compatible robotic devices have been developed at several institutes: Fischer *et al* (2007 and 2008) and DiMaio *et al* (2007) have designed robotic assistants for transperineal prostate needle placement. At the UMCU, a robotic device that can automatically insert needle into the patients prostate under MR guidance is currently under development (Van den Bosch *et al* 2010). This robot is placed between the legs of the patients inside the MR bore. A tapping mechanism is used for needle insertion to restrict prostate movement and tissue deformation (Lagerburg *et al* 2006). Furthermore, needles are inserted under different angles in a divergent way, from a single rotation point. This rotation point is placed just beneath the perineal skin to have access to the whole gland. With this method, it is warranted to deliver the irradiation dose, needle per needle, guided by an adaptive planning system that takes anatomy changes and needle deviations into account. The ultimate goal is therefore to develop a procedure where the parameters of the dose plan are re-optimized after each needle insertion according to the perturbations of the set-up (change of anatomy, needle bending,...). For this purpose, a fast, accurate and stable optimization algorithm is important for inverse planning, enabling the implementation of dose-adaptive focal-HDR brachytherapy in the future. Currently, there is no commercial treatment planning system available which allows divergent needle insertion and adaptive planning. The development of such a treatment planning method is of great importance to find the most optimal implant in regard to planning target volume (PTV) coverage and sparing of organs at risk.

For the planning of brachytherapy intervention, various optimization methods have been developed. The most common algorithms deal with the dwell-times distribution within already implanted catheters such as geometrical optimization (GO) (Kolkman-Deurloo *et al* 1994) or inverse planning simulated annealing (IPSA) (Lessard and Pouliot 2008, Alterovitz *et al* 2006). Some algorithms have been developed to determine the distribution of catheters within the prostate such as the 2D Centroidal Voronoi Tesselations (CVT) algorithm (Poulin *et al* 2013). This CVT algorithm optimizer has been described only for parallel needle configurations. Siauw *et al* (2012) described a needle planning by integer program (NPIP) algorithm to generate needle configurations that avoid critical structures near the penile bulb and other healthy structures, and avoid needle collisions inside the body. It was not applied for a divergent needle pattern with a single rotation point. More recently, hybrid algorithms which optimize the catheter positions and the dwell times have been under investigation. Holm *et al* (2013) has developed a heuristics method for catheter positioning and dwell time distribution for parallel needle pattern with a runtime of 1h without constraints regarding the non-perforation of urethra by the needles. Gorissen *et al* (2013) has developed a hybrid optimizer by using mixed integer programming with a runtime of several minutes.

All mentioned optimizers have certain drawbacks: First, most of them use parallel needle insertions and are not applicable for divergent needle insertion with a single point of insertion. Therefore, they cannot be used to determine the needle angulations or the position of the center of insertion. Second, they usually require

numerous iterations and may produce sub-optimal dose results due to the trapping in local minima regions of the cost function landscape. Third, most optimizers require the manual determination of several input parameters as minima or maxima for PTV and organs at risk. In clinical practice however, dose coverage to the PTV and dose to the organs at risk are used to evaluate if the plan is clinically acceptable and therefore it is desirable to perform an optimization based on these parameters. Fourth, most optimizers usually require weight penalties (or importance coefficients) as input (see Alterovitz *et al* 2006 and Hsu *et al* 2004). These values depend on the patient anatomy. Therefore, weight penalties are not intuitive for a clinician and often need individual adjustment to obtain an acceptable plan. It is therefore necessary to generate a dose plan which will minimize the dose deposition error resulting from the weight penalty dependencies. Finally, in order to be eligible for intra-operative use, the total calculation time to obtain a clinically acceptable plan must be less than several minutes. This is usually not the case for most optimizers.

The aim of this article is to describe the development of a fully automatic inverse dose planning optimization tool for MR-guided focal-HDR brachytherapy on prostate with a divergent needle pattern. Its goal is to determine the optimal center of rotation, needle angulations, source positions and dwell times within a reasonable time needed for intra-operative use. The optimizer will be tested in a planning study by assessing the dose volume parameters.

2.2 Methods

2.2.1 Specification of the optimizer

The coordinate system for the anatomy, the needle and the source positions is defined as follows. Let $\boldsymbol{r} = (x, y, z)$ be the spatial coordinate where x, y and z correspond to the positions in the left-right, the anteroposterior and the inferior-superior direction, respectively. For this divergent needle technique with the needle tracks coming from a single entry point, let $\boldsymbol{r}_{rot} = (x_{rot}, y_{rot}, z_{rot})$ be the position of the center of rotation of the set-up and (θ_i, ϕ_i) the angle of the i^{th} needle insertion in the spherical coordinate system. In the common practice of HDR brachytherapy, the distance Δ between the dwell positions along the needle is constant. Due to the finite size of the needle, the number N_{source} of possible dwell positions of the source along the needle is limited. The dwell positions $\boldsymbol{r}_k^i(\boldsymbol{r}_{rot}, \theta_i, \phi_i),\ k \in [1, N_{source}]$ of the i^{th} needle insertion can then be expressed in Cartesian coordinates as follows:

$$\boldsymbol{r}_k^i(\boldsymbol{r}_{rot}, \theta_i, \phi_i) = \begin{bmatrix} x_{rot} + k\Delta \sin(\theta_i)\cos(\phi_i) \\ y_{rot} + k\Delta \sin(\theta_i)\sin(\phi_i) \\ z_{rot} + k\Delta \cos(\theta_i) \end{bmatrix} \tag{2.1}$$

To develop a fully automatic optimizer for a given number of divergent needle insertions (referred to as N_{needle} needles in the scope of this study), the following parameters need to be optimized: (1) the position of the center of rotation $\boldsymbol{r}_{rot} =$

$(x_{rot}, y_{rot}, z_{rot})$; (2) the angles of the needle tracks $(\theta_{1\cdots N_{needle}}, \phi_{1\cdots N_{needle}})$ in the spherical coordinate system; and (3) the dwell times of the sources t_k^i at the source position k ($k \in [1, N_{source}]$) of the i^{th} needle insertion ($i \in [1, N_{needle}]$).

Let $p = (\boldsymbol{r}_{rot}, \theta_{1\cdots N_{needle}}, \phi_{1\cdots N_{needle}}, t^1_{1\cdots N_{source}}, \cdots, t^{N_{needle}}_{1\cdots N_{source}})$ be the vector containing the parameters of the set-up to be optimized and Ω its corresponding set of feasible solutions.

Finally, for a given dose plan, let $D_{95\%\ PTV}$, $D_{10\%\ Ur}$, $D_{1cc\ Rec}$ and $D_{1cc\ Bl}$ be the dose received by 95% of the PTV, by 10% of the urethra and by $1cm^3$ of rectum and bladder respectively. The optimizer must fulfill the following objectives: 1) highest coverage of the PTV (*i.e.* a large $D_{95\%\ PTV}$) and 2) dose on defined organs at risks (OAR) as low as possible (*i.e.* a small $D_{10\%\ Ur}$, $D_{1cc\ Rec}$ and $D_{1cc\ Bl}$).

The goal of the proposed optimizer is to determine the optimal set of parameters, as follows:

$$p_{optimal} = (\boldsymbol{r}_{rot}, \theta_{1\cdots N_{needle}}, \phi_{1\cdots N_{needle}}, t^1_{1\cdots N_{source}}, \cdots, t^{N_{needle}}_{1\cdots N_{source}})_{optimal} \quad (2.2)$$

to obtain the desired coverage in the PTV without exceeding the constraints of the organs at risk. Therefore, the following constraints function as input of the optimizer: $D^{min}_{95\%\ PTV}$, $D^{max}_{10\%\ Ur}$, $D^{max}_{1cc\ Rec}$ and $D^{max}_{1cc\ Bl}$. They correspond to the minimum value of $D_{95\%\ PTV}$ and the maximum value of $D_{10\%\ Ur}$, $D_{1cc\ Rec}$ and $D_{1cc\ Bl}$ respectively in order to obtain a clinically acceptable and optimal dose plan. Concretely, a dose plan is clinically acceptable when: $D_{95\%\ PTV} > D^{min}_{95\%\ PTV}$,$D_{10\%\ Ur} < D^{max}_{10\%\ Ur}$, $D_{1cc\ Rec} < D^{max}_{1cc\ Rec}$ and $D_{1cc\ Bl} < D^{max}_{1cc\ Bl}$.

As output, the optimizer should give the optimal parameters of the set-up $p_{optimal}$ which corresponds to the maximum $D_{95\%\ PTV}$ in combination with the minimization of $D_{10\%\ Ur}$, $D_{1cc\ Rec}$ and $D_{1cc\ Bl}$.

2.2.2 Dose computation and proposed optimization workflow

According to the guideline of the AAPM Task group No. 43 (Nath *et al* 1995, Rivard *et al* 2004), the dose $D(\boldsymbol{r}, p)$ received at $\boldsymbol{r}$ is expressed as the sum of the contribution of all source positions:

$$D(\boldsymbol{r}, p) = \sum_{i=1}^{N_{needle}} \sum_{k=1}^{N_{source}} d^i_k(\boldsymbol{r}, \boldsymbol{r}_{rot}, \theta_i, \phi_i) t^i_k \quad (2.3)$$

where $d^i_k(\boldsymbol{r}, \boldsymbol{r}_{rot}, \theta_i, \phi_i)$ is the dose-rate of source position k of the i^{th} needle insertion and, depending on the model of the dose distribution chosen (point source, line source,...), is usually a complex non-linear function of $\boldsymbol{r}$, $\boldsymbol{r}_{rot}$, θ_i and ϕ_i.

A way to obtain the desired dose plan is to approach the dose to a given value $D_{opt}(\boldsymbol{r})$ for all points $\boldsymbol{r}$ by solving the following equations:

$$p_{optimal} = \underset{p \in \Omega}{\operatorname{argmin}}[C(p)] \quad (2.4)$$

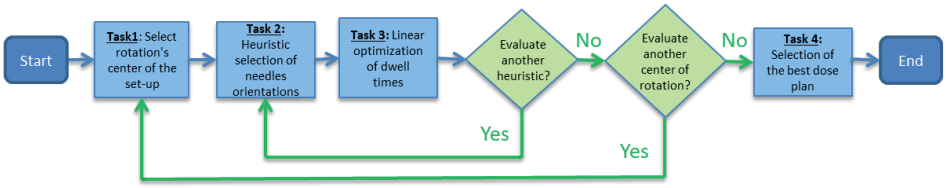

Figure 2.1: Complete optimization workflow for the determination for the position of the center of rotation, the needle orientations and the dwell times of the source.

with

$$C(p) = \iiint_{\boldsymbol{r}\in\mathbb{R}} \omega(\boldsymbol{r})[D(\boldsymbol{r},p) - D_{opt}(\boldsymbol{r})]^2 d\boldsymbol{r} \tag{2.5}$$

where $C(p)$ is called the cost function, $p_{optimal}$ are the optimal parameters defined previously and $\omega(\boldsymbol{r})$ is the weight coefficient at the point $\boldsymbol{r}$ which will be detailed in section 2.2.5.

The strategy of the proposed optimizer benefits from the linear impact of the dwell times on the deposited dose. If the center of rotation and the angles of the needle tracks are fixed, determining the value of t_k^i reverts to solving a set of linear equations and it is thus feasible to find a direct and efficient solution. However, solving Eq. 2.4 for the variables of the needle positioning ($\boldsymbol{r}_{rot}$, $\theta_{1\cdots N_{needle}}$ and $\phi_{1\cdots N_{needle}}$) is highly non-convex and consequently difficult to overcome. Therefore, the proposed method relies on the exact determination of the optimal dwell times using the resolution of linear equations while the remaining variables (position of center of rotation and angulations of needles) are deduced using heuristic or exhaustive searches. Since the area of insertion of the needle is reduced to several square centimeters in order of magnitude, an exhaustive enumeration of $\boldsymbol{r}_{rot}$ is employed. However, regarding the determination of the needle orientations (θ_i, ϕ_i) , an exhaustive optimization is highly time-consuming in practice. Therefore, the idea of evaluating a certain number of heuristics N_{heur} for each center of rotation selected was employed to accomplish this task. The complete workflow of the optimizer is depicted in Figure 2.1.

2.2.3 Task 1: Exhaustive enumeration of the rotation center of the set-up

The first task in the workflow is to select the position of the rotation center of the set-up (*i.e.* $\boldsymbol{r}_{rot}$).

The robotic device currently in development at the UMCU for HDR brachytherapy with divergent needle pattern is made such that the center of rotation should be placed at the perineum (to avoid multiple insertion points and to have full access to the prostate). Therefore, $\boldsymbol{r}_{rot}$ is supposed fixed in the inferior-superior direction

(*i.e.* z-axis) such that z_{rot} is determined by the perineum. Furthermore, the ranges of robot movement are $2cm$ along the x and y-axis due to the restricted space between the legs. Thus, the values of x_{rot} and y_{rot} are initially chosen such that the point P is in line with the center of the largest PTV contour in the transversal plane. An exhaustive search for the optimal center of rotation was performed by evaluating 9 possible candidates on a $1cm$ grid (see Figure 2.2(a)).

2.2.4 Task 2: Heuristic approach of the needle orientations

At this point, the center of rotation is fixed. The next step is to construct several heuristics for the needle orientations. The heuristic approach proposed in this manuscript consists in finding a uniform needle distribution in space with the additional condition that none of the needle tracks perforates the urethra.

For this purpose, the method of Poulin *et al* (2013) for parallel needle set-up was adapted as follows: the PTV and urethra volume are projected from the center of rotation on a transverse plane behind the PTV (see Figure 2.2(a)). The latter projections are noted P_{PTV} and $P_{Urethra}$ respectively. The aim is to find a uniform distribution of N_{needle} points in P_{PTV} without any of those points inside $P_{Urethra}$.

First, N_{needle} initial generators are positioned randomly in P_{PTV}. Then, k-means clustering is applied on the indices of the surface P_{PTV} with the additionnal condition that no cluster centers must stand in $P_{Urethra}$. The final cluster centers reflect the positions of the needle (see Figure 2.2(b)).

This method of heuristic selection relies on a random initial needle set up, therefore several heuristics were evaluated. The number of heuristics evaluated N_{heur} in section 2.2.7.2.

2.2.5 Task 3: Linear optimization of dwell times

While entering this step, the center of rotation and the needle orientations are fixed. The determination of the dwell times can now be expressed using a linear optimization problem as follows.

In the following, N_{source}^{tot} is the total number of active source positions and t_m and $d_m(\boldsymbol{r})$ ($m \in [1, N_{source}^{tot}]$) are the dwell time and dose rate at each active source position respectively.

The final objective is a high PTV coverage while the OAR are spared as much possible. A way to reach this goal is to approach the dose to a certain value D_{PTV} in the PTV and to 0 in the organs at risk. Considering a number N_{OAR} organs at risk, the weight coefficients are supposed constant for the PTV and $OAR_l, l \in [1, N_{OAR}]$ and are noted ω_{PTV} and ω_{OAR_l} respectively in the following. In a discrete space, the cost functions of the PTV and the OAR_l can be defined

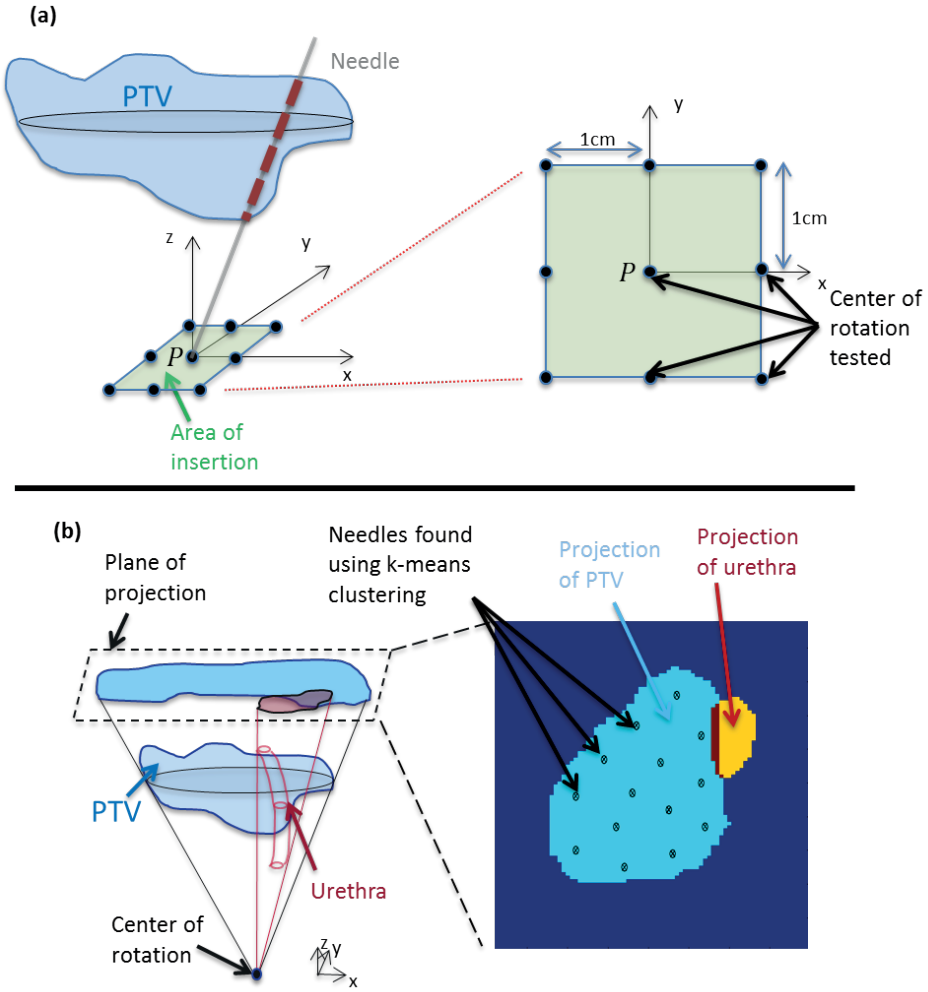

Figure 2.2: Figure 2.2(a) depicts the schematic representation of the exhaustive search of the position of the center of rotation. The area of insertion is represented in light green and the center of rotation evaluated are represented by the black dots. Figure 2.2(b) describes the proposed heuristics for the determination of needle orientations. First, the PTV and the urethra are projected from the center of rotation onto a transverse plane (cf. schematic on the left). A uniform distribution of needles is then found by applying k-means clustering on P_{PTV} until no clusters are found in the urethra zone (cf. schematic on the right).

by referring to the definition of $C(p)$ in Eq. 2.5, as follows:

$$C_{PTV}(p) = \frac{\omega_{PTV}}{V_{PTV}} \sum_{\boldsymbol{r} \in PTV} [D(\boldsymbol{r}, p) - D_{PTV}]^2 \tag{2.6}$$

$$\forall l \in [1, N_{OAR}],\ C_{OAR_l}(p) = \frac{\omega_{OAR_l}}{V_{OAR_l}} \sum_{\boldsymbol{r} \in OAR_l} D(\boldsymbol{r}, p)^2 \tag{2.7}$$

These cost functions were divided by the volume of the organs to avoid volume dependency in the optimization.

Therefore the basic cost function could be expressed as:

$$C(p) = C_{PTV}(p) + \sum_{l=1}^{N_{OAR}} C_{OAR_l}(p) \tag{2.8}$$

The optimal values of $\omega_{OAR_{l \cdots N_{OAR}}}$, ω_{PTV} and D_{PTV} are obviously dependent of the anatomy of the patient. Therefore, in the following sections, the algorithm to minimize $C(p)$ for a given value of $\omega_{OAR_{l \cdots N_{OAR}}}$, ω_{PTV} and D_{PTV} is presented (section 2.2.5.1). In section 2.2.5.2, the method to determine the optimal values of $\omega_{OAR_{l \cdots N_{OAR}}}$, ω_{PTV} and D_{PTV} according to the patients anatomy is described.

2.2.5.1 Solution using matrix inversion

In this section, a direct and fast method to determine the dwell times of the source without unrealistic negative values is described for fixed values of $\omega_{OAR_{l \cdots N_{OAR}}}$, ω_{PTV} and D_{PTV}. This problem of finding the optimal source dwell times for fixed needle positions is analogous to finding the optimal beam intensities in external beam radiotherapy: This reverts to finding a solution of the inverse problem which does not yield unphysical negative values. Therefore, a similar algorithm described by Goldman *et al* (2005 and 2009) in the case of Intensity Modulated Radiation Therapy (IMRT) known as Fast Inverse Dose Optimization (FIDO) is used. Goldman described a method to obtain a direct solution of the inverse problem that avoids negative beamlet weights. It involves reformulating the organs at risk cost functions $C_{OAR_l}(p)$: in Eq. 2.7, $D(\boldsymbol{r}, p)^2$ is replaced by $\sum_{m=1}^{N_{source}^{tot}} [d_m(\boldsymbol{r}) t_m]^2$. By modifying the organs at risk cost functions, $C_{OAR_l}(p)$ will not be null through destructive interference effects between dwell times and most of the unphysical negative solutions are therefore excluded. Furthermore, the optimization problem is reduced to a set of linear equations.

With this method, the optimal dwell times are obtained by the matrix inversion:

$$T = \alpha^{-1} \beta \tag{2.9}$$

with $T = (t_m)_{m \in [1, N_{source}^{tot}]}$ is the vector of N_{source}^{tot} elements containing the dwell times at all active source positions. β is also a vector of N_{source}^{tot} elements and α is a $N_{source}^{tot} \times N_{source}^{tot}$ matrix defined respectively as follows:

$$\forall m \in [1, N_{source}^{tot}],\ \beta_m = \frac{\omega_{PTV} D_{PTV}}{V_{PTV}} \sum_{\boldsymbol{r} \in PTV} d_m(\boldsymbol{r}) \tag{2.10}$$

$$\forall m, n \in [1, N_{source}^{tot}],\ \alpha_{mn} = \frac{\omega_{PTV}}{V_{PTV}} \sum_{\boldsymbol{r} \in PTV} d_m(\boldsymbol{r}) d_n(\boldsymbol{r}) + \sum_{l=1}^{N_{OAR}} \frac{\omega_{OAR_l}}{V_{OAR_l}} \sum_{\boldsymbol{r} \in OAR_l} d_m(\boldsymbol{r}) d_n(\boldsymbol{r}) \delta_{mn} \tag{2.11}$$

where δ_{mn} is the Kronecker delta function.

2.2.5.2 Exhaustive search of the weight coefficients (ω_{PTV}, $\omega_{OAR_{1 \cdots N_{OAR}}}$) and the dose approached for the PTV (D_{PTV})

As the matrix inversion in Eq. 2.9 is little time consuming to execute, it is possible to obtain the overall results by an exhaustive search of $\omega_{OAR_{l \cdots N_{OAR}}}$, ω_{PTV} and D_{PTV}. Consequently, no individual adjustment of these parameters is needed to obtain an acceptable plan and the dwell times found will be optimal for any anatomy. The exhaustive optimization of $\omega_{OAR_{l \cdots N_{OAR}}}$, ω_{PTV} and D_{PTV} will be investigated in section 2.2.7.1.

2.2.6 Task 4: Selection of the best dose plan

The exhaustive enumeration of Task 1 (center of rotation of set-up), the several heuristics generated in Task 2 (needle orientations) and the exhaustive search $\omega_{OAR_{l \cdots N_{OAR}}}$, ω_{PTV} and D_{PTV} in Task 3 (dwell times) will gives several dose plans. The objective is now to select the best plan. The following criterion is proposed: the best plan has the highest value of energy E (in Gy) defined as:

$$E = \min(A, B, C, D) \tag{2.12}$$

with the relative parameters:

$$\begin{cases} A = D_{95\%\ PTV} - D_{95\%\ PTV}^{min} \\ B = D_{10\%\ Ur}^{max} - D_{10\%\ Ur} \\ C = D_{1cc\ Rec}^{max} - D_{1cc\ Rec} \\ D = D_{1cc\ Bl}^{max} - D_{1cc\ Bl} \end{cases}$$

The parameters A, B, C and D represent the relative difference between the dose coverage parameters and the clinical constraints (set as input) of the PTV, the urethra, the rectum and the bladder, respectively. The higher the value of A, the better the dose coverage of the PTV. Moreover, the clinical constraint at the PTV is achieved if, and only if $A > 0$. Consequently, the minimum value over A, B, C and D in Eq. 2.12 corresponds to the maximal dose covering error with respect to

the clinical constraints within the region that receives the "worst" dose deposition. E therefore represents the quality of the dose plan: the greater E is, the better the dose plan becomes (the dose plan is clinically acceptable if, and only if $E > 0$).

In conclusion, by maximizing E, the plan which has all parameters optimized (maximum $D_{95\%\ PTV}$ in combination with minimization of $D_{10\%\ Ur}$, $D_{1cc\ Rec}$ and $D_{1cc\ Bl}$) is selected.

2.2.7 Experimental validation

The different steps in the optimizer workflow were assessed before the complete optimizer workflow was validated. In the first experiment, the dwell time optimization (see section 2.2.5) was analyzed by assessing the automatic search of $\omega_{OAR_{l\cdots N_{OAR}}}$, ω_{PTV} and D_{PTV}. In the second experiment, regarding the determination of the needle angulations (see section 2.2.4), the required number N_{heur} of heuristic to evaluate was analyzed. The last experiment consisted in testing the complete optimizer workflow in a planning study by assessing the dose volume parameters.

The experiments were performed in a retrospective evaluation using clinical data from 10 patients. The delineations of the prostate tumors and the OAR considered (urethra, bladder, rectum and rest of the tissues) were made on a $1mm^3$ resolution MRI image by an experienced oncologist. The PTV volumes ranged from $8.5cm^3$ to $23.3cm^3$ with a median of $16.1cm^3$. For all experiments, the clinical values as input were: $D^{min}_{95\%\ PTV} = 19Gy$, $D^{max}_{10\%\ Ur} = 21Gy$, $D^{max}_{1cc\ Rec} = 12Gy$ and $D^{max}_{1cc\ Bl} = 12Gy$. Those are the clinical constraint values for single fraction HDR brachytherapy as monotherapy used at the UMCU. For all experiments, varying numbers of needle insertions (from 2 to 14) were tested.

Regarding the source position the common procedure at the UMCU was adopted: for each needle insertion, the active source center positions were separated by a step-size of $\Delta = 2.5mm$ and situated inside the PTV with an extra margin of $3mm$.

For dose calculation, the dose rate was calculated using the Task Group No. 43 one-dimensional formalism incorporating a point source approximation due to the minimum time of computation, with a small adaptation as follows to avoid over-optimization of the dose close to the source:

$$\begin{aligned} d^i_k(\boldsymbol{r}, \boldsymbol{r}_{rot}, \theta_i, \phi_i) = \\ S_K \Lambda g_P[R^i_k(\boldsymbol{r}, \boldsymbol{r}_{rot}, \theta_i, \phi_i)] \Phi_{an}[R^i_k(\boldsymbol{r}, \boldsymbol{r}_{rot}, \theta_i, \phi_i)] \\ \times \frac{{R_0}^2}{R^i_k(\boldsymbol{r}, \boldsymbol{r}_{rot}, \theta_i, \phi_i)^2 + \exp[-R^i_k(\boldsymbol{r}, \boldsymbol{r}_{rot}, \theta_i, \phi_i)^2]} \end{aligned} \tag{2.13}$$

where S_K is the air-kerma strength, Λ the dose-rate constant in water, $\Phi_{an}(R)$ the one-dimensional anisotropy factor, R_0 denotes the reference distance which

is specified to be $10mm$, $g_P(R)$ corresponds to the radial dose function in the case of point source approximation model and $R_k^i(\boldsymbol{r}, \boldsymbol{r}_{rot}, \theta_i, \phi_i)$ is the distance (in millimeters) between the source position $\boldsymbol{r}_k^i(\boldsymbol{r}_{rot}, \theta_i, \phi_i)$ and $\boldsymbol{r}$ ($R_k^i(\boldsymbol{r}, \boldsymbol{r}_{rot}, \theta_i, \phi_i) = ||\boldsymbol{r}_k^i(\boldsymbol{r}_{rot}, \theta_i, \phi_i) - \boldsymbol{r}||_2$). With this adaptation of the point source model, the dose has an upper limit value close to the source, therefore it reduces the numeric instabilities for $R_k^i(\boldsymbol{r}, \boldsymbol{r}_{rot}, \theta_i, \phi_i)$ approaching 0.

TG43 constants, anisotropy factor and radial dose function for the microSelectron (Elekta/Nucletron, Veenendaal, The Netherlands) HDR 192-Iridium source were taken from a study of Daskalov *et al* (1998) (Λ=1.108$cGy.h^{-1}.U^{-1}$) and an arbitrary source strength $S_K = 40.80mGy.h^{-}1.m^2$ was chosen. The multiplication of the radial dose function $g_P(R)$ and the anisotropy factor $\Phi_{an}(R)$ were approximated by a 2^{nd} order polynomial fit ($g_P(R) \cdot \Phi_{an}(R) = a_0 + a_1 R + a_2 R^2$). The coefficients for the fit were $a_0 = 1.11$, $a_1 = -3.30 \cdot 10^{-3}$ and $a_2 = 3.12 \cdot 10^{-6}$, where R is in millimeters.

As well as an evaluation of dose to target and OAR, dose homogeneity and conformity were also investigated. The parameters homogeneity ($HI_{150\%}$ and $HI_{200\%}$) and conformal index ($COIN$) are defined respectively as:

$$HI_{i\%} = \frac{V_{100\%\ PTV} - V_{i\%\ PTV}}{V_{100\%\ PTV}} \ with\ i \in \{150, 200\} \tag{2.14}$$

$$COIN = \frac{(V_{100\%\ PTV})^2}{V_{PTV} V_{100\%\ body}} \tag{2.15}$$

where $V_{i\%\ PTV}$ ($V_{100\%\ body}$ respectively) is the volume inside the PTV (the total volume respectively) that receive $i\%$ (100% respectively) of the prescribed dose *i.e.* $D_{95\%\ PTV}^{min}$). The $HI_{i\%}$ measures the volumes fraction that receives between 100% and $i\%$ ($i \in \{150, 200\}$) of the prescribed dose and the $COIN$ compares the reference dose coverage in the PTV with the total volume in the reference isodose volume.

2.2.7.1 Assessment of the exhaustive search of ω_{PTV}, $\omega_{OAR_{1\cdots N_{OAR}}}$ and D_{PTV}) for the dwell times optimization (Task 3)

In this experiment, the automatic search of $\omega_{OAR_{l\cdots N_{OAR}}}$, ω_{PTV} and D_{PTV} is assessed. The center of rotation was fixed in line with the center of the largest PTV contour in the transversal plane and the mid-plane of the tumor. A heuristic for the needle orientations was determined as described in section 2.2.4. The dwell times for all source positions were calculated using Eq. 2.9 for all possible combinations of weights coefficients of PTV, urethra, bladder, rectum and other tissues (respectively ω_{PTV}, ω_{Ur}, ω_{Bl}, ω_{Rec} and ω_{tissue}), and D_{PTV} such that:

$$D_{PTV} \in \{20, 21, \cdots, 79, 80\} \tag{2.16}$$

$$\log_{10}(\omega_{PTV}) \in \{0, 0.001, \cdots, 9.999, 10\} \tag{2.17}$$

$$(\log_{10}(\omega_{Ur}), \log_{10}(\omega_{Bl}), \log_{10}(\omega_{Rec}), \log_{10}(\omega_{tissue})) \in \{0, 1, \cdots, 9, 10\}^4 \tag{2.18}$$

with the additional condition that:

$$log_{10}(\omega_{PTV}) + \log_{10}(\omega_{Ur}) + \log_{10}(\omega_{Bl}) + \log_{10}(\omega_{Rec}) + \log_{10}(\omega_{tissue}) = 10 \tag{2.19}$$

to avoid redundancy of results.

From all resulting dose plans, the best one was selected with the selection criterion defined in section 2.2.6

In the following experiments (described in section 2.2.7.2 and 2.2.7.3), to obtain the optimal dwell time, the optimal values of ω_{PTV}, ω_{Ur}, ω_{Bl}, ω_{Rec} and ω_{tissue} and D_{PTV} were determined by applying the same exhaustive search. However, in order to decrease the time of calculation, the exhaustive search range of ω_{PTV} was reduced to:

$$\log_{10}(\omega_{PTV}) \in \{0, 1, \cdots, 9, 10\} \tag{2.20}$$

2.2.7.2 Analysis of the required number of heuristic for the needle angulations to be evaluated in Task 2

In this experiment, the number of heuristic evaluated N_{heur} in Task 2 was assessed. The complete optimizer workflow was performed several times without an exhaustive search of the center of rotation (which was fixed in line with the center of the largest PTV contour in the transverse plane and the mid-plane of the tumor) for N_{heur} varying from 1 to 80. The energy, E, of the final dose plan was determined as a function of N_{heur}.

For the following experiment described in section 2.2.7.3, N_{heur} was fixed to 10 to limit the time of calculation.

2.2.7.3 Analysis of the number of inserted needles

In this experiment, the optimizer was tested in a planning study by assessing the dose volume parameters. $p_{optimal}$ was determined to obtain the desired coverage without exceeding the constraints of the organs at risk for 2, 4, 6, 8, 10, 12 and 14 needle insertions by using the earlier mentioned constraints as inputs.

2.3 Results

In this section, the results of the experiment described in section 2.2.7 are presented below. Firstly, the results of the exhaustive search of ω_{PTV}, ω_{Ur}, ω_{Bl}, ω_{Rec} and ω_{tissue} and D_{PTV} to obtain optimal dwell times are described in section 2.3.1. Regarding the optimization of the needle angulations, the results of the analysis of the required number N_{heur} of heuristic evaluations are described in section 2.3.2. Finally, the results of the planning study for one typical patient and afterwards, for all patients are shown in section 2.3.3.

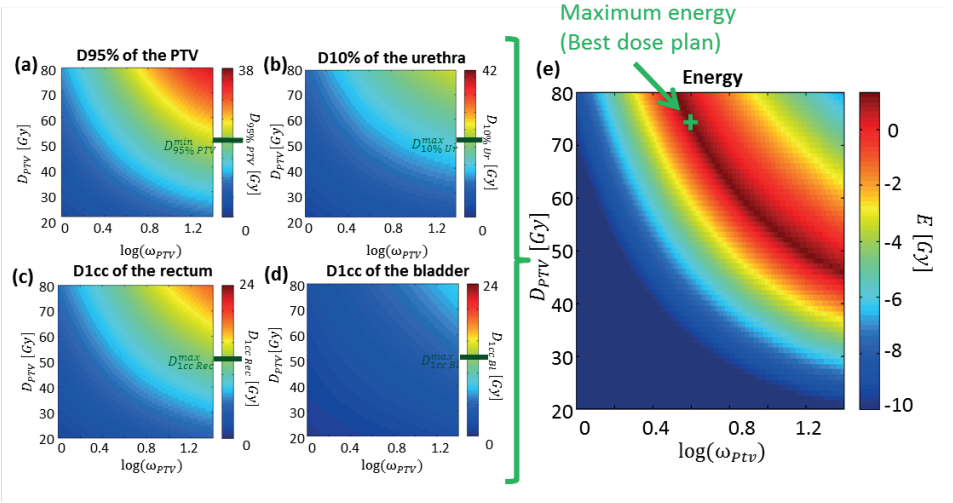

Figure 2.3: Results of the simulation obtained on a typical patient with 10 needle insertions. The values of $D_{95\%\ PTV}$, $D_{10\%\ Ur}$, $D_{1cc\ Rec}$, $D_{1cc\ Bl}$ and E (computed from Eq. 2.12) are presented as function of $\log_{10}(\omega_{PTV})$ and D_{PTV} (Figure 2.3(a), 2.3(b), 2.3(c), 2.3(d) and 2.3(e) respectively). $\log_{10}(\omega_{tissue})$ was deducted from Eq. 2.19. On figure 2.3(a), 2.3(b), 2.3(c) and 2.3(d), the horizontal green lines represent the clinical constraints set as input.

2.3.1 Assessment of the exhaustive search of ω_{PTV}, $\omega_{OAR_{1\cdots N_{OAR}}}$ and D_{PTV}) for the dwell times optimization (Task 3)

In this section, the results of the experiment described in section 2.2.7.1 are presented in Figure 2.3 for one patient with 10 needle insertions as a typical example.

The best dose plan (*i.e.* the one maximizing E) was found with the following parameters:

$$\{D_{PTV}, \omega_{PTV}, \omega_{Ur}, \omega_{Bl}, \omega_{Rec}, \omega_{tissue}\} = \{75, 10^{0.587}, 10^2, 10^4, 10^2, 10^{1.413}\} \quad (2.21)$$

The values of $D_{95\%\ PTV}$, $D_{10\%\ Ur}$, $D_{1cc\ Rec}$, $D_{1cc\ Bl}$ and E are plotted in Figure 2.3 as a function of D_{PTV} and $\log_{10}(\omega_{PTV})$. For the representation, $\{\omega_{Ur}, \omega_{Bl}, \omega_{Rec}\}$ were set to their optimal values $\{10^2, 10^4, 10^2\}$ and ω_{tissue} was deducted from Eq. 2.19.

Figure 2.3(a), 2.3(b), 2.3(c) and 2.3(d) show an increase of the dose deposition in all the different volumes considered (PTV, urethra, bladder and rectum) for increasing D_{PTV} and $\log_{10}(\omega_{PTV})$. In Figure 2.3(e), the best solutions (where E is maximal) are located on a continuous line.

For $\log_{10}(\omega_{PTV}) > 1.42$, one or more dwell times found with FIDO had negative

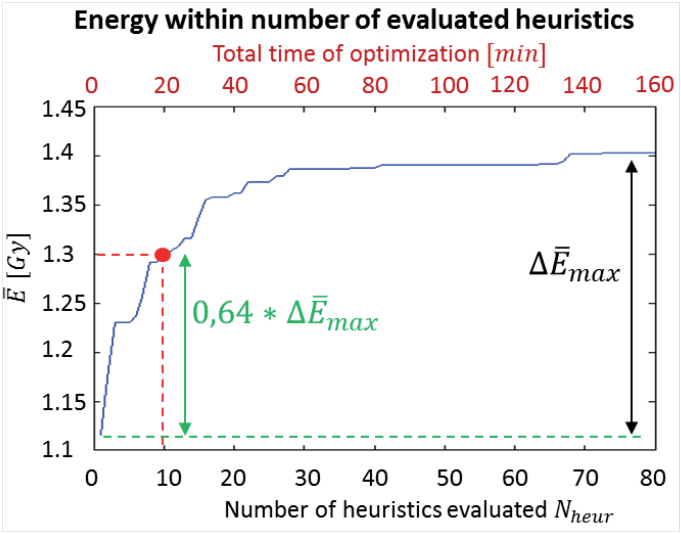

Figure 2.4: Energy of the selected dose plan averaged on ten patients as a function of the number of heuristics evaluated. The total computation time of the optimizer (linear with the number of heuristics evaluated) is depicted in red.

values. These nonphysical solutions are due to the resolution of the equation: by modifying the organ at risk cost functions in FIDO, most of the solutions which give negative dwell times are removed but not all of them.

2.3.2 Analysis of the required number of heuristic for the needle angulations to be evaluated in Task 2

In this section, the results of the experiment described in section 2.7.2 are presented in a situation of a large number of needle insertions ($N_{needle} = 14$): This corresponds to the worst case scenario where the calculations are the most time-consuming. For each patient, the energy E of the selected dose plan was calculated within the number of heuristics evaluated. The average energy $\overline{E}$ on all 10 patients was plotted as a function of N_{heur} (Figure 2.4 and the calculation time of the complete optimization workflow was also represented.

Figure 2.4 shows a fast initial increase of $\overline{E}$ with the number of evaluated heuristics. Afterwards, the gradient decreases progressively. For $N_{heur} = 10$, $\overline{E}$ achieves 64% of its value for $N_{heur} = 80$. Furthermore, the number of heuristics evaluated in Task 2 is directly proportional to the calculation time of the complete optimization workflow. The time of optimization for $N_{heur} = 10$ was approximatly 20 minutes on a PC with a 3.10GHz Intel®CoreTM i5-2400 processor and 8GB RAM using MATLAB R2013a.

2.3.3 Analysis of the number of inserted needles

The dose distribution was calculated on 10 patients (PTV volumes ranged from ranged from $8.5cm^3$ to $23.3cm^3$ with a median of $16.1cm^3$) for 2, 4, 6, 8, 10, 12 and 14 needle insertions by using the earlier mentioned constraints as input. For each case, $D_{95\%\ PTV}$, $D_{10\%\ Ur}$, $D_{1cc\ Rec}$, $D_{1cc\ Bl}$, $HI_{150\%}$, $HI_{200\%}$ and $COIN$ was computed.

The result for one typical patient is shown in Figure 2.5(a)(b)(c) and (d). The dose constraints set as input are also represented. $D_{95\%\ PTV}$ increased with the number of needle insertions, and $D_{1cc\ Rec}$ and $D_{1cc\ Bl}$ decreased. Furthermore, for this patient, $D_{10\%\ Ur}$ did not seem to have a clear trend. All the dose constraints were already reached at four needle insertions. Moreover, $HI_{200\%}$ and $COIN$ increased with the number of needle insertions, but the influence of N_{needle} on $HI_{150\%}$ was relatively small.

Figure 2.5(c) shows the MRI image of a sagittal plane of the same patient with delineations and figure 2.5(d) and 2.5(e) show the dose distribution in this same sagittal plane for 2 and 10 needle insertions respectively. The cold spots in the PTV and the hot spots in the rectum were significantly reduced for $N_{needle} = 10$ compared to $N_{needle} = 2$.

For 2, 4, 6, 8, 10, 12 and 14 needle insertions the averaged parameters on all patients $\overline{D_{95\%\ PTV}}$, $\overline{D_{10\%\ Ur}}$, $\overline{D_{1cc\ Rec}}$, $\overline{D_{1cc\ Bl}}$, $\overline{HI_{150\%}}$, $\overline{HI_{200\%}}$ and $\overline{COIN}$ are presented in Figure 2.5(g) and (h).

Once again, $\overline{D_{95\%\ PTV}}$ increased on average with the number of needle insertions, while $\overline{D_{10\%\ Ur}}$, $\overline{D_{1cc\ Rec}}$ and $\overline{D_{1cc\ Bl}}$. The large ranges of values were due to the different anatomies of the 10 patients tested. $\overline{HI_{200\%}}$ and $\overline{COIN}$ also increased with the number of needle insertions but $\overline{HI_{150\%}}$ did not show any clear trend. On average, a clinical acceptable plan is already reached by using four needle insertions.

2.4 Discussion

In this manuscript, an automatic inverse dose planning optimization tool for MRI-guided focal-HDR brachytherapy on prostate with divergent needle pattern is proposed. The aim was to determine the optimal parameters of the set-up (point of rotation, needles angles and dwell times) which corresponds to the maximization of $D_{95\%\ PTV}$ in combination with minimization of $D_{10\%\ Ur}$, $D_{1cc\ Rec}$ and $D_{1cc\ Bl}$. For that, the linear impact of the dwell times on the deposited dose was exploited and the remaining variables were determined by evaluating several heuristics for the needle angulations and by an exhaustive search for the position of the point of rotation.

Unlike most optimizers such as HIPO or IPSA, the proposed method does not require individual adjustments of several input parameters such as minimum dose, maximum dose or weight coefficients for PTV and organs at risk to obtain an

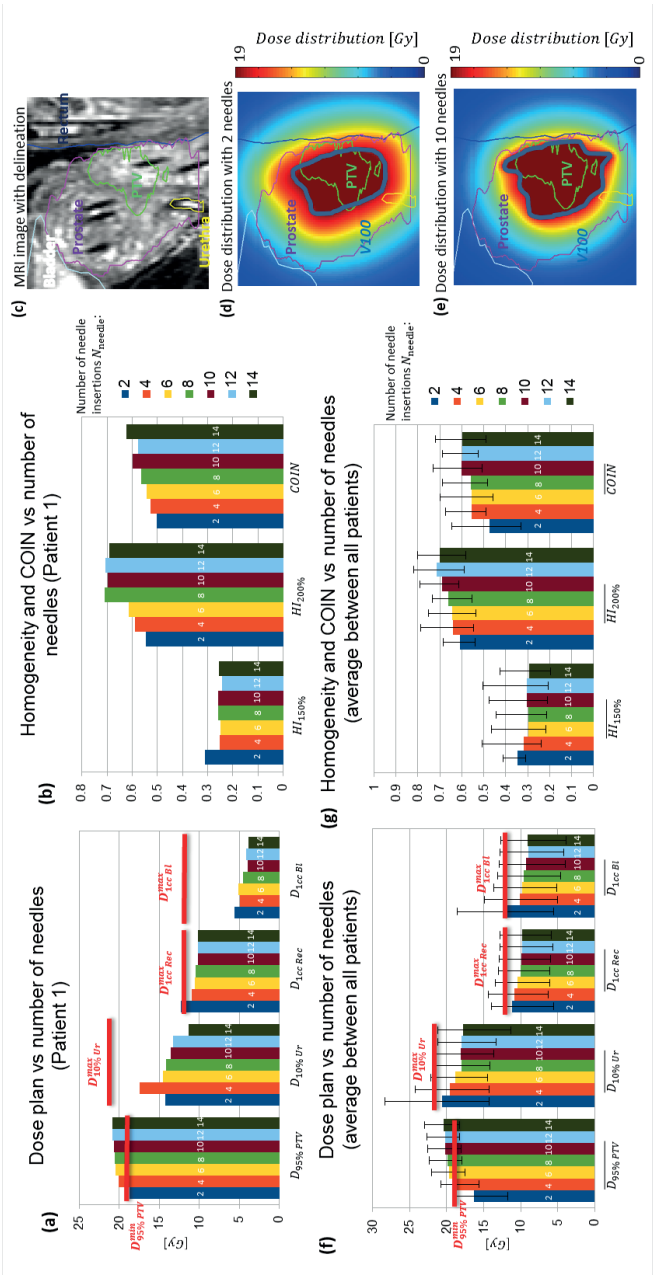

Figure 2.5: Results of the planning study for using 2, 4, 6, 8, 10, 12 and 14 needle insertions. Figure 2.5(a)(b)(c)(d) and (e) present the optimization results for a typical patient case. Figure 2.5(a) shows the output parameters ($D_{95\%\ PTV}$, $D_{10\%\ Ur}$, $D_{1cc\ Rec}$ and $D_{1cc\ Bl}$). Figure 2.5(b) shows the Homogeneity ($HI_{150\%}$ and $HI_{200\%}$) and the conformal index ($COIN$). Figure 2.5(c) presents a slice of MRI image in the sagittal plane with the delineations of the volumes of interest. Figures 2.5(d) and (e) present the corresponding dose distributions for 2 and 10 needle insertions respectively on the same sagittal slice. Figure 2.5(f) and (g) present the optimization results for 10 different patients. Figure 2.5(f) shows, the average output parameters on all patients $\overline{D_{95\%\ PTV}}$, $\overline{D_{10\%\ Ur}}$, $\overline{D_{1cc\ Rec}}$ and $\overline{D_{1cc\ Bl}}$.Figure 2.5(g) represents the average on all patients of homogeneity and conformal index ($\overline{HI_{150\%}}$, $\overline{HI_{200\%}}$ and $\overline{COIN}$ respectively). For the two latter graphs, the whole range of values is represented by the solid vertical line. For Figure 2.5(a)(b)(f) and (g), The red solid lines represent the clinical constraints set as input ($D^{min}_{95\%\ PTV}$, $D^{max}_{10\%\ Ur}$, $D^{max}_{1cc\ Rec}$ and $D^{max}_{1cc\ Bl}$ respectively)

acceptable plan (Dinkla *et al* 2014). Figure 2.3 illustrates the importance of an exhaustive optimization of the weight coefficients and approached dose at the PTV to determine the optimal dwell times. It shows that the dose deposition is made at the expense of all the other regions. In particular for this patient, the rectum played a very important role in the dose deposition. However, the dose deposition is a little less critical for the urethra and has little impact for the bladder. Thus, it is difficult to predict how the weight coefficients influence the overall dose plan. As an example, increasing ω_{PTV} will certainly increase $D_{95\%\ PTV}$, but its influence on $D_{10\%\ Ur}$, $D_{1cc\ Rec}$ or $D_{1cc\ Bl}$ is unknown: it could be insignificant or dramatic depending on the anatomy of the patient. However, the gain in energy would not significantly drop by using a larger step in the exhaustive search of $\log_{10}(\omega_{PTV})$. Therefore, $\log_{10}(\omega_{PTV})$ is varied from 0 to 10 with a step of 1 in order to reduce the time of optimization and still obtain a good dose plan.

An important step in brachytherapy and thus in the optimizer workflow is to find the optimal needle positions. The algorithms developed recently are usually based on iterative methods (Holm *et al* 2013, Gorissen *et al* 2013 and Siauw *et al* 2012) which cause two problems. First, such algorithms strongly depend on the initialization and therefore could produce sub-optimal solutions due to the trapping in local minima regions of the cost function landscape. The second problem is that, due to the high non-convexity of the problem, the optimization may require a long calculation time. To avoid these problems, a different approach was chosen: The angulation of the needle tracks is determined by evaluating several heuristics chosen carefully using the k-means clustering. According to Figure 2.4, for a given point of rotation, evaluating 10 heuristics already gives a good dose plan compared to 80 heuristics and a significantly better dose plan compared to one heuristic. By evaluating 10 heuristics, the total time of the optimization for a given number of needle insertions is below 20min. It is important to note that the program has been developed on Matlab and has not been optimized for speed. The proposed pipeline and the employed numerical schemes thus show great perspectives for a further reduction of the computation time using Graphical Processing Units (GPU's) in a parallel architecture. This will be studied in future work.

Finally, the planning study of the proposed optimizer workflow shows promising results. The clinical constraints set as input were reached on average with 4 needle insertions which is better compared to the current clinical procedure where 13 to 17 needles are usually inserted (see Hsu *et al* 2004, Menard *et al* 2004). More precisely, the increase of $D_{95\%\ PTV}$ as well as the decrease of $D_{1cc\ Rec}$ or $D_{1cc\ Bl}$ with the number of needle insertions for the patient shown in Figure 2.5(a) was expected. $D_{10\%\ Ur}$ did not depict a trend with the number of needle insertions: it already fulfilled by far the constraints for the urethra set as input ($D^{max}_{10\%\ Ur} = 21Gy$) and therefore it was not the parameter to be optimized in priority. Moreover, $HI_{200\%}$ and $COIN$, expressing the dose homogeneity and conformity respectively, increased with the number of needle insertions as expected. $HI_{150\%}$ did not show a clear trend. In this study, the PTV volumes had a median of $16.1cm^3$ and all the dose constraints were already reached at 4 needle insertions on average. Therefore,

those results are in line with the study of Steggerda *et al* (2010) which shows, in the case of LDR brachytherapy, satisfactory dose coverage for, on average, 0.3 needles per cm^3 prostate volume. Furthermore, Vargas *et al* (2004) and Boyea *et al* (2007) showed the urinary toxicity following HDR brachytherapy is significantly increased by using more than 14 needle insertions. The cold spot in the PTV for 2 needle insertions as presented on Figure 2.5(d) was reduced by an increasing number of needle insertions (see Figure 2.5(e)). This illustrates how the number of needle insertions could improve the dose distribution. Figures 2.5(g) and 2.5(f) confirms the observation shown in Figures 2.5(a) and 2.5(b) for a typical patient. $\overline{D_{95\%\ PTV}}$ increased with the number of needle insertions, whereas $\overline{D_{10\%\ Ur}}$, $\overline{D_{1cc\ Rec}}$ and $\overline{D_{1cc\ Bl}}$ decreased. The large range between the maximum and minimum values is explained by the different anatomy of each patient especially the position of the tumor with respect to the other organs at risk. $\overline{HI_{150\%}}$, $\overline{HI_{200\%}}$ and $\overline{COIN}$ showed the same trend as in Figures 2.5(a) and 2.5(b).

A limitation in using less needle insertions is that the robustness of the dose plan may drop. It must be kept in mind that these are only simulations: in practice, there may be errors in needle positioning or in the position of the rotation point which may lead to modifications in the dose distribution. The impact of an error in position of one needle on the dose plan must be studied in future work. Furthermore, it is important to note that in this study, no modification of the anatomy (for example due to the insertion of the needle) was taken into account. Lagerburg *et al* (2006) however showed that the prostate motion was significantly less when using a robotic device that taps the needle compared to hand insertion.

A way to further increase the quality of the dose plan would be to couple this method with a gradient-based optimizer on all parameters at the same time (point of rotation, needles angles and dwell times) based on the cost function described in Eq. 2.5. However, the dose distribution may not be drastically changed because it would only improve locally the parameters. Since on average, a clinically acceptable plan is already reached by using four needle insertions, coupling this method with a gradient-based optimization might not be necessary.

Moreover, the pipeline proposed is compatible with a re-optimization of the dose plan parameters after each insertion of the needle thanks to the proposed experimental set-up: in terms of hardware, the robotic device developed in our institution is such that the needle can be inserted needle under MR guidance, and, in terms of software, the calculation time of the optimizer could be further reduced to make it eligible for intra-operative use. The development of a procedure which re-optimize of the dose plan parameters after each insertion of the needle will be also studied in future work.

Although the optimizer described here was implemented with the point source approximation for simplicity of calculation, the proposed method allows the use of more precise source models such as the line source approximation.

This optimizer workflow completes all objectives: it is developed for divergent

needle patterns with a single rotation point and it optimizes the clinically relevant dose parameters of HDR brachytherapy for prostate cancer, specifically $D_{95\%\ PTV}$, $D_{10\%\ Ur}$ $D_{1cc\ Rec}$ and $D_{1cc\ Bl}$. Unlike most optimizers such as HIPO (Karabis *et al* 2009) and IPSA (Hsu *et al* 2004), no manual determination of several input parameters as minima or maxima dose for PTV and organs at risk is necessary. Moreover, most optimizers require weight coefficients to be defined (see Dinkla *et al* 2014), whereas the proposed optimizer workflow does not since an automatic exhaustive search for optimal coefficient values is performed. The results prove that the optimizer workflow presented is able to obtain a clinically accepted plan with a few needle insertions already, whereas during the current clinical procedure, 13 to 17 needles are usually inserted. However, the impact of practical error in needle positioning must be studied to find the optimal number of needle insertions for real clinical procedures. Finally, the proposed optimizer took less than 20 minutes to compute although it has not been optimized in speed. Therefore, it shows great perspectives for a further reduction of the computation time by parallelizing the calculation in order to be eligible for intra-operative use.

2.5 Conclusion

In this paper, a complete inverse dose planning optimization workflow for focal-HDR prostate brachytherapy with a divergent needle pattern was presented. It can determine the optimal center of rotation, needle positioning (thus source positions) and dwell times of the sources in order to deliver the desired dose distribution for a given number of needle insertions. The optimization is made on the dose coverage (meaning the $D_{95\%\ PTV}$, $D_{10\%\ Ur}$ $D_{1cc\ Rec}$ and $D_{1cc\ Bl}$) and does not need to set importance factors for the organ doses considered as input. Clinically accepted plans were obtained for on average 4 needle insertions for the 10 patients tested.

CHAPTER 3

Adaptive planning strategy for HDR prostate brachytherapy - a simulation study on needle positioning errors

The following chapter is based on:
Borot de Battisti M, Denis de Senneville B, Maenhout M, Hautvast G, Binnekamp D, Lagendijk J J W, Van Vulpen M and Moerland M A 2016 Adaptive planning strategy for high dose rate prostate brachytherapy - a simulation study on needle positioning errors *Phys. Med. Biol.* **61** 2177-95

Abstract

The development of MR-guided HDR brachytherapy for prostate cancer has gained an increasing interest for delivering a high tumor dose safely in a single fraction. To support needle placement in the limited workspace inside the closed-bore MRI, a single-needle MR-compatible robot is currently under development at the UMCU. This robotic device taps the needle in a divergent way from a single rotation point into the prostate. With this setup, it is warranted to deliver the irradiation dose needle per needle. Although robot-assisted needle placement is expected to be more accurate than manual template guided insertion, needle positioning errors may occur and are likely to modify the pre-planned dose distribution.

In this paper, we propose a dose plan adaptation strategy for HDR prostate brachytherapy with feedback on the needle position: a dose plan is made at the beginning of the interventional procedure and updated after each needle insertion in order to compensate for possible needle positioning errors. The introduced procedure can be used with the single needle MR-compatible robot developed at the UMCU. The proposed feedback strategy was tested by simulating complete HDR procedures with and without feedback on 8 patients with different number of needle insertions (varying from 4 to 12). In 97% of the cases tested, the number of clinically acceptable plans obtained at the end of the procedure was larger with feedback compared to the situation without feedback. Furthermore, the computation time of the feedback between each insertion was below $100s$ which makes it eligible for intra-operative use.

3.1 Introduction

Whole-gland LDR brachytherapy is often implemented in patients with favourable risk prostate cancer since it is a minimally invasive procedure with good long-term clinical outcome (Hinnen *et al* 2010, Henry *et al* 2010 and Zelefsky *et al* 2007). However, toxicity such as acute urinary retention remains a concern with this treatment modality (Stone and Stock 2002, Roeloffzen *et al* 2011). To reduce toxicity in patients with localized prostate carcinoma, focal treatment has gained an increasing interest as an alternative to whole-gland therapy. This may be achieved with focal-HDR brachytherapy (Banerjee *et al* 2015).

Focal-HDR brachytherapy requires high precision of tumor localization, OARs localization and dose delivery in order to deliver the high tumor dose safely in a single fraction. In the current practice at the UMCU, needles are manually inserted under TRUS guidance, in a parallel configuration based on a template grid, while needle reconstruction, dose planning and needle position verification are assessed using MR imaging. This procedure is not optimal since the use of two imaging modalities, US for needle insertion and afterwards MRI for final needle reconstruction, is time consuming. Furthermore, the US-guided manual insertion

of needles leads to suboptimal configurations due to prostate deformations and swelling. As a consequence, the US-based implant configuration may be less optimal when reconstructed using MR imaging. Therefore, a complete MR-guided focal-HDR procedure is under investigation. For optimal MR guidance during therapy, MR-guided needle insertion is required. This is currently impossible due to space restrictions in a closed bore MR system.

To support needle placement in the limited workspace inside the closed-bore MRI, MR-compatible robotic devices are being developed at several institutes (Podder *et al*, 2014): Fischer *et al* (2007 and 2008) and DiMaio *et al* (2007) have designed robotic assistants for transperineal prostate needle placement. At the UMCU, a single needle robotic device is currently under development. This robotic device is placed between the legs of the patient inside the MR bore and can automatically insert, under MR guidance, the needle into the prostate (Van den Bosch *et al* 2010). A tapping mechanism is used for needle insertion to restrict prostate movement and tissue deformation (Lagerburg *et al* 2006). Furthermore, the needle is inserted under different angles in a divergent way, from a single rotation point. This rotation point is placed just beneath the perineal skin to have access to the whole gland. Therefore, it is warranted to deliver the irradiation dose needle per needle. Recently, a fast optimization planning method was proposed for this setup (Borot de Battisti, 2015).

However, two major events are likely to modify the pre-planned dose distribution during the interventional process:

Event 1 **Needle deviations**. Although the robot-assisted needle placement for HDR brachytherapy is expected to be more accurate than the manual template guided needle placement, some errors in needle positioning may persist: Straßmann *et al* (2011) showed that the average needle positioning accuracy for the robot-assisted method on a prostate model was $1.8 \pm 0.6mm$.

Event 2 **Unpredictable anatomy modifications**. Swelling, displacement (Stone *et al* 2002) or rotation (Lagerburg *et al* 2005) of the prostate (related to the trauma caused by the needle insertion) or intra-procedural changes in rectum or bladder filling can cause anatomical modifications during the intervention. As an example, Lagerburg *et al* (2005) showed that the needle insertion could cause a prostate rotation up to $13.8°$.

Needle deviations or anatomy modifications during treatment can lead to dramatic changes in dose distribution. With feedback on needle position and anatomy, it is possible to optimize and update the irradiation dose after each needle insertion.

This paper aims to take a step towards MR-guided dose-adaptive focal HDR brachytherapy. A dose plan adaptation strategy is proposed to address the first aforementioned step (**Event 1**): A dose plan is made at the beginning of the interventional procedure and updated after each needle insertion to compensate for

possible needle deviations. The proposed feedback strategy was evaluated by simulating complete single fraction HDR brachytherapy on 8 patients with different number of needle insertions (varying from 4 to 12).

3.2 Methods

The aim of focal single fraction prostate HDR brachytherapy is to obtain the prescribed dose in the complete PTV without exceeding the constraints of the organs at risk. At the UMCU, a dose plan is considered clinically acceptable when:

$$\begin{cases} D_{95\%\ PTV} > D^{min}_{95\%\ PTV} \\ D_{10\%\ Ur} < D^{max}_{10\%\ Ur} \\ D_{1cc\ Rec} < D^{max}_{1cc\ Rec} \\ D_{1cc\ Bl} < D^{max}_{1cc\ Bl} \end{cases} \tag{3.1}$$

where $D_{95\%\ PTV}$, $D_{10\%\ Ur}$, $D_{1cc\ Rec}$ and $D_{1cc\ Bl}$ are the dose received by 95% of the PTV, by 10% of the urethra and by $1cc$ of rectum and bladder respectively. $D^{min}_{95\%\ PTV}$, $D^{max}_{10\%\ Ur}$, $D^{max}_{1cc\ Rec}$ and $D^{max}_{1cc\ Bl}$ correspond to the minimal accepted value of $D_{95\%\ PTV}$ and the maximal accepted value of $D_{10\%\ Ur}$, $D_{1cc\ Rec}$ and $D_{1cc\ Bl}$ in order to obtain a clinically acceptable and optimal dose plan.

In this manuscript, we propose a dose plan adaptation strategy with feedback on the needle position. The proposed strategy is based on the re-optimization of the dose plan after each needle insertion. The question is: how to deliver a clinically acceptable dose distribution knowing that we may have needle position deviations? For that, a feedback strategy is proposed which aims to determine the dose plan including the determination of, the center of rotation of the setup, the position of the needle tracks, the dwell positions and the dwell times. An initial dose plan is calculated at the beginning of the procedure. Subsequently, the dose plan is adjusted after each needle insertion.

To achieve a re-optimization strategy, the following tasks are proposed (see Figure 3.1):

Task 1 At the beginning of the treatment, the initial dose plan for a given number of needle insertions N_{needle} is determined: This corresponds to the dose plan in case no needle deviations occur during treatment.

Task 2 In general, the needle must follow several tracks to complete the treatment. The user selects the first, or next, needle track to be placed and delivered.

Task 3 After selection of the needle track, the needle is inserted. An error in needle positioning may occur during insertion.

Task 4 The position of the needle is measured. At this point, the needle has been placed without insertion of the source.

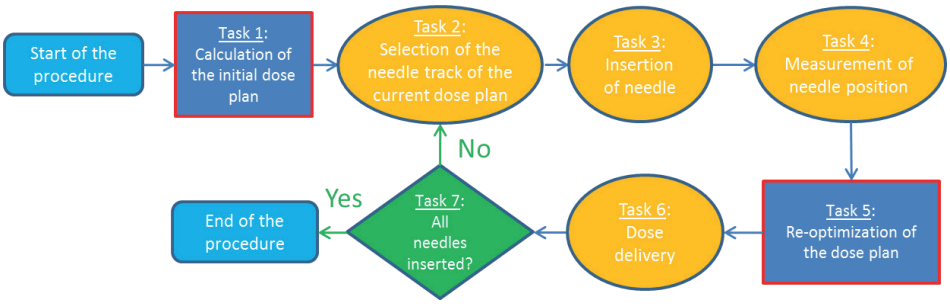

Figure 3.1: Schematic of the dose plan adaptation strategy with feedback on the needle deviation.

Task 5 A re-optimization of the dose plan is performed considering the deviation of the inserted needle. Consequently, (1) the angulation, dwell positions and times of the remaining needle tracks and (2) the dwell positions and times corresponding to the inserted needle are updated.

Task 6 The source is inserted in the needle following the updated dose plan. After irradiation, the needle is retracted.

Task 7 As long as the complete dose plan is not delivered, **Task 2**, **Task 3**, **Task 4**, **Task 5** and **Task 6** are repeated (the dose plan and the sequence of insertion are updated at each iteration).

The different tasks can be separated in two categories: optimization tasks (*i.e.* **Task 1** and **Task 5** represented by the blue rectangles in Figure 3.1) and interventional tasks (*i.e.* **Task 2**, **Task 3**, **Task 4** and **Task 6** represented by the yellow ovals in Figure 3.1). In this study, we will focus on the optimization tasks *i.e.* **Task 1** and **Task 5**, and simulate the interventional tasks.

To clarify the benefits of the proposed method on the overall results, the anatomy of the patient (which is delineated before **Task 1**) is supposed to remain constant throughout the procedure in order to exclude possible artifacts and uncertainties of image registration or dose accumulations. Therefore, only needle positioning errors are taken into account in the scope of this study. The manual needle track selection of **Task 2** is simulated according a well defined strategic intent to place and deliver needle tracks which may have the most negative impact on dose quality first (this needle track is referred to as "the most sensitive needle track" in this manuscript), such that re-optimization of the subsequent needles has the best possibility to compensate for needle placement errors. Furthermore, needle tracks are supposed to be straight (no bending of the needle) and the errors in needle positioning will be approximated by an angulation error (the depth of the needle and the center of rotation are according to the initial dose plan in **Task 1**).

3.2.1 Assessment of the quality of the dose plan

Throughout **Task 1** and **Task 5**, there is the requirement to select automatically the best dose plan among several others. Therefore the quality of a dose plan must be quantified. For that, the energy E proposed by Borot de Battisti *et al* (2015) defined as:

$$E = \min(A, B, C, D) \tag{3.2}$$

with:

$$\begin{cases} A = D_{95\%\ PTV} - D^{min}_{95\%\ PTV} \\ B = D^{max}_{10\%\ Ur} - D_{10\%\ Ur} \\ C = D^{max}_{1cc\ Rec} - D_{1cc\ Rec} \\ D = D^{max}_{1cc\ Bl} - D_{1cc\ Bl} \end{cases} \tag{3.3}$$

is used. The parameters A, B, C and D represent the differences between the dose coverage parameters and the clinical constraints (set as input) of the Planning Target Volume (PTV), the urethra, the rectum and the bladder, respectively. For example, if A is positive, the dose plan reached the clinical prescribed dose of the PTV. Conversely, if A is negative, the clinical prescribed dose of the PTV was not achieved. More precisely, the higher the value of A is, the higher the dose coverage of the PTV becomes. Consequently, the minimum value over A, B, C and D in Eq. 3.2 corresponds to the "worst" error in dose deposition between the different regions of interest (PTV and OARs). E represents therefore the quality of the dose plan: the larger E, the better the dose plan in terms of quality (if $E > 0$ all clinical constraints are fulfilled, conversely if $E < 0$ they are not).

3.2.2 Calculation of the initial dose plan (Task 1)

Let $\boldsymbol{r}_{rot} = (x_{rot}, y_{rot}, z_{rot})$ be the position of the center of rotation of the setup and (θ_i, ϕ_i) the angle of the i^{th} needle track in the spherical coordinate system. In common practice of HDR brachytherapy, the distance Δ between the dwell positions along the needle is constant. Due to the finite size of the needle, the number N_{source} of possible dwell positions of the source along the needle is limited. The dwell positions $\boldsymbol{r}^i_k(\boldsymbol{r}_{rot}, \theta_i, \phi_i),\ k \in [1, N_{source}]$ of the i^{th} needle insertion can then be expressed in the Cartesian coordinates as follows:

$$\boldsymbol{r}^i_k(\boldsymbol{r}_{rot}, \theta_i, \phi_i) = \begin{bmatrix} x_{rot} + k\Delta \sin(\theta_i)\cos(\phi_i) \\ y_{rot} + k\Delta \sin(\theta_i)\sin(\phi_i) \\ z_{rot} + k\Delta \cos(\theta_i) \end{bmatrix} \tag{3.4}$$

To calculate the initial dose plan for a given number N_{needle} of divergent needle insertions, the following parameters must be optimized:

- The position of the center of rotation of the setup $\boldsymbol{r}_{rot}$.

- The angle of the i^{th} needle track (θ_i, ϕ_i) $(i \in [1, N_{needle}])$.
- The dwell time t_k^i of the source position k of the i^{th} needle track ($i \in [1, N_{needle}]$ and $k \in [1, N_{source}]$).

Borot de Battisti *et al* (2015) described a way to determine those parameters, but other methods can also be applied.

3.2.3 Simulating selection of the needle track (Task 2)

At **Task 2**, the needle that is about to be inserted is selected by the user. In our simulations, we try to mimic a strategic intent of the user to place the most sensitive needle track first, such that potential errors can still be compensated by the re-optimization of the subsequent needles. To determine the most sensitive needle track, a criterion, which quantifies the impact of an inaccurate needle insertion on the dose plan quality, is introduced. More precisely, the needle track chosen is the one which may have the most negative impact on the dose plan quality if a deviation occurs during insertion of the needle: Inserting the needle into this track leaves the best possibility to compensate for needle placement error by re-optimizing the dose plan for the remaining needle tracks.

Practically, the most sensitive needle track can be selected using a stochastic approach based on simulations as follows:

For all remaining needle tracks i $(i \in [1; N_{tracks}])$:

(1) Starting from the current dose plan, a random change of angulation of needle track i is simulated. A random angulation change modeled by a Gaussian distribution with a standard deviation of $0.015rad$ was found to be a good representation of a typical insertion error ($0.015rad$ corresponds to a deviation of $3mm$ at a distance of $200mm$ from the center of rotation).

(2) Without any re-optimization, the value of E corresponding to the resulting dose plan is calculated.

(3) Step (1) and (2) are repeated N_{angle} times (with N_{angle} an integer big enough to be statistically acceptable). After investigation, a typical value of $N_{angle} = 100$ was found to be a good compromise between speed and accuracy

(4) The 5 percentiles (noted $E_{5\%}(i)$) of the values of E obtained in step (2) are calculated: it quantifies how negative is potentially the impact of an inaccurate needle insertion in needle track i on the dose plan quality.

The selected most sensitive needle track is therefore $i_{selected}$ such that:

$$i_{best} = \underset{i \in [1; N_{tracks}]}{\operatorname{argmin}} [E_{5\%}(i)] \tag{3.5}$$

3.2.4 Re-optimization of the dose plan (Task 5)

At **Task 5**, the recently inserted needle underwent a potential deviation as compared to the targeted dose plan. A re-optimization of the remaining parameters (angles of the needle tracks and dwell times) is thus mandatory to compensate for this deviation and to achieve the clinical prescription. This section presents the method of re-optimization of these remaining parameters.

Supposing that the recently inserted needle is associated to the ${N_{ins}}^{th}$ needle insertion ($N_{ins} \leq N_{needle}$), the following parameters need to be re-optimized:

- The angle of the remaining needle tracks $(\theta_i, \phi_i)_{N_{ins}<i\leq N_{needle}}$.
- The dwell times $(t_k^i)_{N_{ins}\leq i\leq N_{needle}}^{1\leq k\leq N_{source}}$ of the needle which has just been inserted ($i = N_{ins}$) and the dwell times of the remaining needle tracks ($N_{ins} < i \leq N_{needle}$).

Let $p = (\theta_{N_{ins}+1\cdots N_{needle}}, \phi_{N_{ins}+1\cdots N_{needle}}, t_{1\cdots N_{source}}^{N_{ins}}, \cdots, t_{1\cdots N_{source}}^{N_{needle}})$ be the vector containing the parameters of the setup to re-optimize and Ω its corresponding set of feasible solutions. According to the guideline of the AAPM Task group No. 43 (Nath *et al* 1995, Rivard *et al* 2004), the dose $D(\boldsymbol{r}, p)$ received at $\boldsymbol{r}$ can be expressed as the sum of the contribution of all source positions:

$$D(\boldsymbol{r}, p) = D_{deliv}(\boldsymbol{r}) + \sum_{i=N_{ins}}^{N_{needle}} \sum_{k=1}^{N_{source}} d_k^i(\boldsymbol{r}, \boldsymbol{r}_{rot}, \theta_i, \phi_i) t_k^i \tag{3.6}$$

where $D_{deliv}(\boldsymbol{r})$ is the already delivered dose to the patient.

A way to determine the optimal parameters $p_{optimal} \in \Omega$ is to approach the dose to a given value $D_{opt}(\boldsymbol{r})$ for all points $\boldsymbol{r}$. The determination of $p_{optimal}$ is therefore a multi-objective optimization and can be determined by solving the following equations:

$$p_{optimal} = \underset{p\in\Omega}{\operatorname{argmin}}[C(p)] \tag{3.7}$$

with

$$C(p) = \iiint_{\boldsymbol{r}\in\mathbb{R}} \omega(\boldsymbol{r})[D(\boldsymbol{r}, p) - D_{opt}(\boldsymbol{r})]^2 d\boldsymbol{r} \tag{3.8}$$

where $C(p)$ is the cost function and $\omega(\boldsymbol{r})$ is a spatial weight function (the latter will be detailed in section 3.2.4.2).

The strategy for the resolution benefits from the linear impact of the dwell times on the deposited dose. If $(\theta_{N_{ins}+1\cdots N_{needle}}, \phi_{N_{ins}+1\cdots N_{needle}})$ are fixed, the determination of t_k^i reverts to solving a set of linear equations and it is thus feasible to

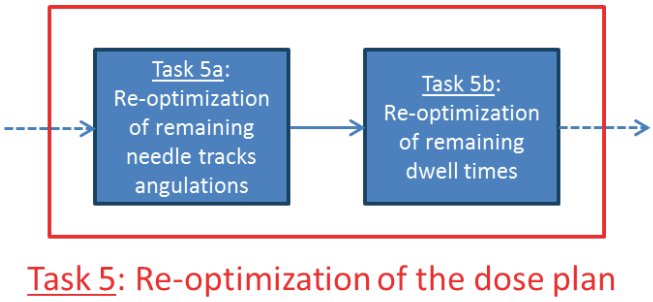

Figure 3.2: Steps for the re-optimization of the dose plan (**Task 5**). This consists in first re-optimizing the needle tracks angulations (**Task 5a**), then the remaining dwell times (**Task 5b**).

find a direct and efficient solution. However, solving Eq. 3.7 for the variables of the needle positioning ($\theta_{N_{ins}+1\cdots N_{needle}}, \phi_{N_{ins}+1\cdots N_{needle}}$) is highly non-convex and consequently difficult to overcome. The workflow of the dose plan re-optimization is depicted in Figure 3.2. The proposed method relies on the determination of the optimal angulations of the remaining needle tracks and are deduced using heuristic searches (**Task 5a**) while the optimal dwell times are determined by the resolution of linear equations (**Task 5b**).

3.2.4.1 Re-optimization of the position of remaining needle positions (Task 5a)

In this section, the heuristic approach to re-optimize the remaining needle positions of the dose plan is described. We seek an uniform distribution in space of needle tracks that will cover the PTV without crossing the urethra.

For that, the PTV and the urethra are projected from the center of rotation on a transverse plane behind the PTV (see Figure 3.3). The projection of the needle tracks on the same plane can be represented by N_{needle} points. To determine a uniform distribution of points, an extension of the procedure described by Borot de Battisti *et al* (2015) is applied: k-means clustering with the additional constraints of immobility of the cluster centers corresponding to the tracks where the needle was already inserted. Figure 3.3 shows a typical example of re-optimization of the needle track positions using this method.

Consequently, with this method, we can re-optimize the positions of the needle tracks in order to obtain a distribution as uniform as possible and the errors in angulation during insertion of the needle can be thus compensated.

3.2.4.2 Re-optimization of the remaining dwell times (Task 5b)

At this point, the position of the needle tracks are fixed. The distance Δ between the dwell positions along the needle remains the same (the coordinate of

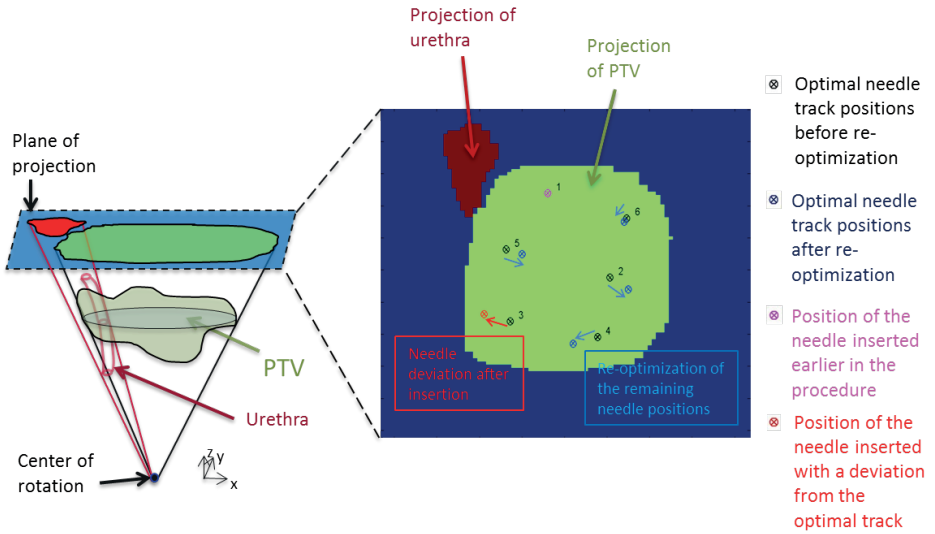

Figure 3.3: The schematic of the projection of the PTV and the urethra are depicted on the left, the result of the k-means algorithm to re-optimize the needle positions on the right schematic. *needle* 1 was already inserted and dose was delivered and thus, its position is fixed (cf. pink target). Positions of *needle track* 2, 4, 5, 6 change after re-optimization due to error in positioning *needle* 3

the source positions are derived from Eq. 3.4). The remaining dwell times must then be determined to complete the re-optimization of the dose plan. To insure that, the method of dwell times determination described by Borot de Battisti *et al* (2015) is adapted considering the dose already distributed by the previous needle insertions. Mathematically, the approach consists in slightly modifying the cost function $C(p)$ (defined by Eq. 3.8) in order to determine the dwell times by solving linear equations while excluding unphysical negative results. The numerical implementation of this method is presented in the Appendix.

3.2.5 Validation study of the proposed re-planning tool

A planning study was performed to test our re-optimization procedure. The approach consists in comparing the dose distribution obtained in the scenario with and without feedback of the needle position. For that, complete single fraction HDR brachytherapy procedures with and without the proposed feedback strategy were simulated. In the situation without feedback, no re-optimization of the dose plan was done after the insertion of the needle (*i.e.* **Task 5** was skipped).

The simulations were done on 8 patients, with various number of needle insertions (N_{needle} varying from 4 to 12). The anatomy of the patients was obtained using the delineations of the prostate tumors and the OAR considered (urethra, bladder,

rectum and rest of the tissues) on $1mm^3$ resolution MR image by an experienced oncologist.

For all patients, the clinical constraints were:

$$\begin{cases} D_{95\%\ PTV} > 19Gy \\ D_{10\%\ Ur} < 21Gy \\ D_{1cc\ Rec} < 12Gy \\ D_{1cc\ Bl} < 12Gy \end{cases} \tag{3.9}$$

Those constraints are in line with the study of Hoskin *et al* (2014) and Prada *et al* (2012) who showed that HDR brachytherapy as monotherapy is feasible with acceptable levels of acute complications by delivering a single fraction dose of $19Gy$ to the target. All the MR images used for the simulations of this study are intra-operative images of patients who underwent HDR prostate brachytherapy as monotherapy in a single fraction at the UMCU. These were patients with localized prostate cancer, a prostate-specific antigen (PSA) level lower than $10\,\mathrm{ng\,ml^{-1}}$ and a Gleason score of 7 or less. The PTV volumes ranged from $20.7cm^3$ to $31.3cm^3$ with a median of $24.75cm^3$. The acquisition of patient MR images used in this study was approved by the Institutional Review Board (IRB).

To simulate the positioning error during the insertion of the needle, we modeled it by a random angulation error described by a Gaussian distribution with a standard deviation of $0.015rad$. Moreover, we supposed that no error occurred in the measurement of the needle position. In that way, only the contribution of the proposed feedback strategy on the needle positioning errors is assessed.

Source positions were chosen according to the common procedure at the UMCU: for each needle insertion, the active source center positions were separated by a step-size of $\Delta = 2.5mm$ and situated inside the PTV with margin of $3mm$.

To simulate the irradiation and calculate the dose delivered to the patient, the dose rate was calculated using the point source approximation model because of its minimum time of computation, with a small adaptation as follows to avoid over-optimization of the dose close to the source:

$$d_i(\boldsymbol{r}) = S_K \Lambda g_P[R_i(\boldsymbol{r})] \Phi_{an}[R_i(\boldsymbol{r})] \frac{{R_0}^2}{R_i(\boldsymbol{r})^2 + \exp[-R_i(\boldsymbol{r})^2]} \tag{3.10}$$

where S_K is the air-kerma strength, Λ the dose-rate constant in water, $\Phi_{an}(R)$ the one-dimensional anisotropy factor, R_0 the reference distance which is specified to be $10mm$, $g_P(R)$ to the radial dose function in the case of the point source approximation model and $R_i(\boldsymbol{r})$ the distance (in millimeters) between the i^{th} source position at coordinate $\boldsymbol{r}_i$ and $\boldsymbol{r}$ ($R_i(\boldsymbol{r}) = ||\boldsymbol{r}_i - \boldsymbol{r}||_2$). With this adaptation of the point source model, the dose has an upper limit value close to the source, therefore it reduces the numeric instabilities for $R_i(\boldsymbol{r})$ approaching 0. TG43 constants, anisotropy factor and radial dose function for the microSelectron-HDR

(Elekta/Nucletron, Veenendaal, The Netherlands) 192-Iridium source were taken from a study of Daskalov *et al* (1998) ($\Lambda = 1.108 cGy.h^{-1}.U^{-1}$) and an arbitrary source strength $S_K = 40.80 mGy.h^{-}1.m^2$ was chosen. The multiplication of the radial dose function $g_P(R)$ and the anisotropy factor $\Phi_{an}(R)$ was approximated by a 2^{nd} order polynomial fit ($g_P(R) \cdot \Phi_{an}(R) = a_0 + a_1 R + a_2 R^2$). The coefficients for the fit were $a_0 = 1.11$, $a_1 = -3.30 \cdot 10^{-3}$ and $a_2 = 3.12 \cdot 10^{-6}$, where R is in millimeters.

Due to the randomness of the needle deviations during insertions, both simulations with and without feedback were repeated 100 times to verify the robustness of both procedures.

The dose parameters obtained at the end of the procedure were compared to the aforementioned clinical constraints to verify if the dose distributions were clinically acceptable.

3.3 Results

In section 3.3.1, **Task 2** is assessed: a typical situation is presented where a needle track must be selected for insertion among the several possibilities proposed by the dose plan. In section 3.3.2, the results of the planning study are presented : the dose parameters ($D_{95\%\ PTV}$, $D_{10\%\ Ur}$, $D_{1cc\ Rec}$ and $D_{1cc\ Bl}$) of two typical cases (patient 1 with $N_{needle} = 6$ and patient 4 with $N_{needle} = 4$) are presented. Furthermore, the percentages of clinically acceptable final dose plans obtained for all cases described in the planning study are depicted.

3.3.1 Assessment of the proposed feedback criterion for the needle track selection

As a typical example of **Task 2**, patient 1 of the planning study with 6 needle insertions ($N_{needle} = 6$) is detailed in Figure 3.4. We first focus our interest on the specific instant of the interventional procedure for which the 2nd insertion of the needle must be simulated (the needle track corresponding to the 1^{st} needle insertion is noted *needle track* 1). The most sensitive needle track of the current dose plan must be selected. For that, the method described in section 3.2.3 is applied in order to predict the impact of an inaccurate needle insertion for each individual needle track. The value of E corresponding to each individual needle track (*needle tracks* 2 to 6) is presented in Figure 3.4(a).

The distribution of energy values is different from one needle track to another. For this case, the median(minimum,maximum) of energy corresponding to *needle track* 2, 3, 4 and 5 are $0.9(-0.4, 1.2)Gy$, $0.5(-1.3, 1.2)Gy$, $0.7(-0.9,\ 1.2)Gy$, $1.0(0.0, 1.2)Gy$ and $1.1(0.9, 1.2)Gy$ respectively. The 5th percentile of energy was $0.1Gy$, $-0.8Gy$, $-0.5Gy$, $0.7Gy$ and $1.0Gy$ for *needle track* 2, 3, 4 and 5 respectively. The energy value in case of insertions without error was $1.2Gy$. The most sensitive needle track is therefore *needle track* 3 (conversely, *needle track* 6 is the

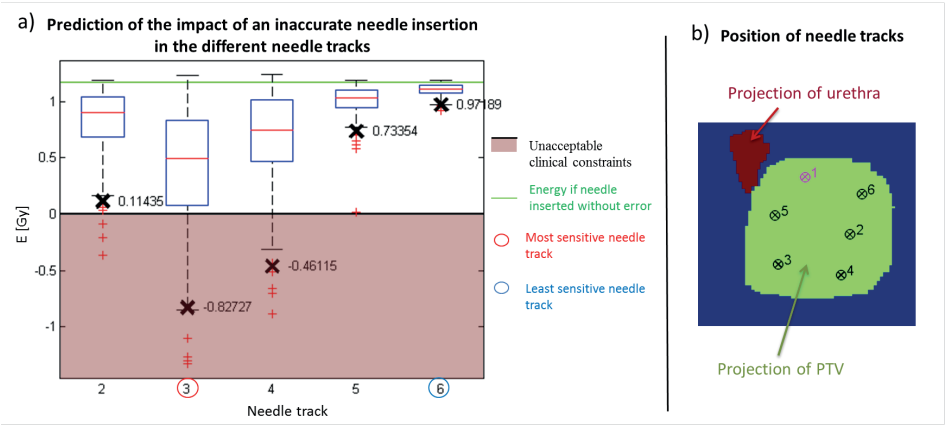

Figure 3.4: Prediction of the impact of an inaccurate needle insertion in the different needle tracks. Figure (a) corresponds to the dispersion of the energy E of each needle track. The most sensitive and least sensitive needle tracks are represented by the red and blue circle respectively. For each needle track, the black crosses correspond to the 5 percentiles values of E. Figure (b) represents the position of the needle tracks projected in the transversal plane (same as Figure 3.3).

least sensitive needle track). Consequently, the needle track selected for insertion is *needle track* 3 in that case.

3.3.2 Assessment of the proposed feedback strategy

For all tested patients, the percentages of clinically acceptable plans for the procedures with and without feedback are presented in Table 3.1. When the value is not presented (for example patient 5 for $N_{needle} = 4$), it corresponds to the case where the initial dose plan (without errors in needle placement) obtained at **Task 1** did not achieve the clinical constraints: in those cases there was no point to perform the experiment since the dose plan quality will only decrease due to error in needle positioning at each insertion. In all other cases, the dose plan without error in needle placement achieved the clinical constraints.

The results presented in Table 3.1 show that in 36 of the 37 cases tested (97%), the number of clinically acceptable plans obtained at the end of the procedure was larger with feedback as compared to the scenario without feedback. The only exception was for patient 5 with $N_{needle} = 6$: the values in that case were quite similar (7% and 9% with and without re-optimization respectively). Furthermore, the percentage of clinically acceptable dose plans tended to increase with the number of needle insertions employed in both situations with and without re-optimization.

The dose parameters of two typical examples (patient 1 with $N_{needle} = 6$ and

Table 3.1: Percentage of clinically acceptable dose plans obtained for 8 patients with $N_{needle} = 4$, 6, 8, 10 and 12. Prostate and PTV volumes are depicted in bottom lines.

	Clinically acceptable plan (%)															
	Pat. 1		Pat. 2		Pat. 3		Pat. 4		Pat. 5		Pat. 6		Pat. 7		Pat. 8	
Number of needle insertions	without re-opt.	with re-opt.	without re-opt.	with re-opt.	without re-opt.	with re-opt.	without re-opt.	with re-opt.	without re-opt.	with re-opt.	without re-opt.	with re-opt.	without re-opt.	with re-opt.	without re-opt.	with re-opt.
4	39	99	32	79	14	60	47	93	-	-	-	-	80	99	19	53
6	53	100	31	94	32	94	42	94	9	7	-	-	89	100	11	49
8	68	100	40	100	40	97	52	97	17	51	-	-	100	100	16	58
10	71	100	78	100	63	90	47	100	25	78	10	71	97	100	22	85
12	76	100	53	100	43	98	78	100	31	80	62	96	97	100	35	90
Prostate (cm^3)	102.5		84.7		54.2		65.8		68.5		50.2		85		76.5	
PTV (cm^3)	26.0		22.8		25.2		24.3		22.8		20.7		30.7		31.3	

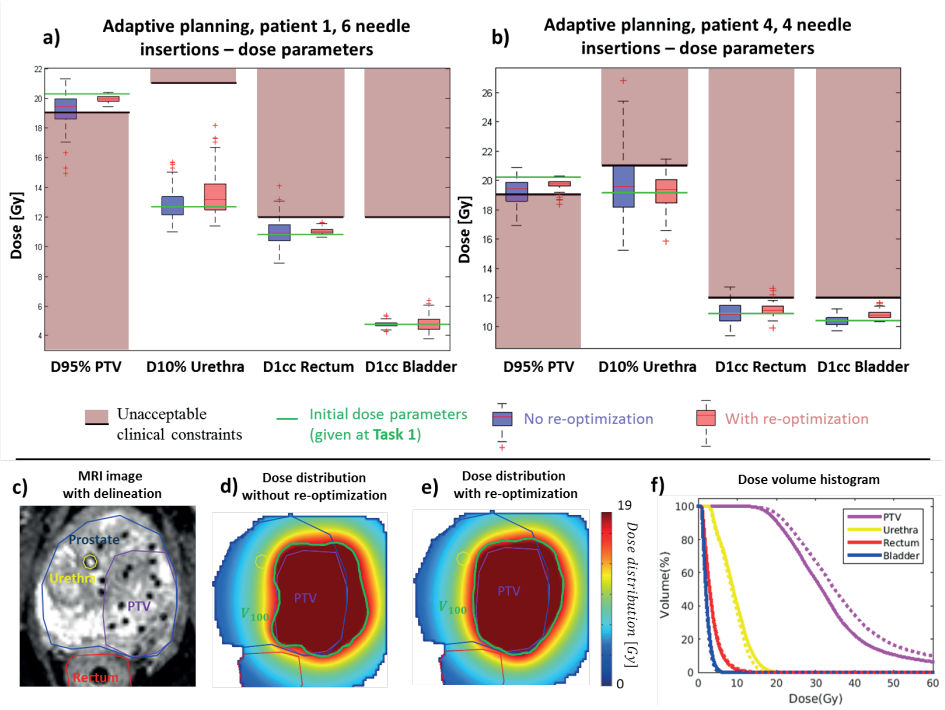

Figure 3.5: Dose parameters resulting from simulations of HDR brachytherapy on patient 1 with $N_{needle} = 6$ (Figure (a) and patient 4 with $N_{needle} = 4$ (Figure (b)) Blue: without re-optimization, red: with re-optimization. The dose parameters of the dose plan without error in needle placement are represented by the green horizontal lines. Figures (c)–(e) present, in the case of Patient 1 with $N_{needle} = 6$, a slice of MRI image in the transverse plane (with the delineations of the volumes of interest) and an example of the corresponding dose distribution without and with re-optimization respectively. Figure (f) shows the associated DVH in the situation without (solid line) and with re-optimization (dashed line). This MR data comes from a patient who underwent a HDR brachytherapy procedure with 16 needles in a parallel pattern, which explains the needle tracks in figure (c).

patient 4 with $N_{needle} = 4$) are depicted in figure 3.5(a) and 3.5(b). Typical dose distributions and the Dose-Volume Histogram (DVH) obtained from the simulations are shown in figures 3.5(c)–(f) for patient 1 with $N_{needle} = 6$. Both the situations with and without re-optimization are presented.

For patient 1 with $N_{needle} = 6$, the dose parameters ($D_{95\%\ PTV}$, $D_{10\%\ Ur}$, $D_{1cc\ Rec}$ and $D_{1cc\ Bl}$) of the dose plan without error in needle placement were $20.3Gy$, $12.7Gy$, $10.8Gy$ and $4.8Gy$ respectively. The distributions (median(minimum, maximum)) of $D_{95\%\ PTV}$, $D_{10\%\ Ur}$, $D_{1cc\ Rec}$ and $D_{1cc\ Bl}$ in the case with error

in needle placement were $19.4(14.9, 21.3)Gy$, $12.7(11.0, 15.7)Gy$, $10.9(8.9, 14.1)Gy$ and $4.8(4.3, 5.4)Gy$ respectively without re-optimization and $19.9(19.4, 20.3)Gy$, $13.2(11.4, 18.1)Gy$, $11.0(10.6, 11.6)Gy$ and $4.8(3.8, 6.4)Gy$ respectively with re-optimization. Moreover, without re-optimization, 53% of the dose plans with error in needle placement did not achieve the clinical constraints whereas 100% of them did with re-optimization (those values are reported in Table 3.1). The example presented in figures 3.5(d), (e) and (f) show better PTV coverage for the plans with reoptimisation compared to the plans without.

For patient 4 with $N_{needle} = 4$, the dose parameters of the dose plan without error in needle placement were $20.2Gy$, $19.1Gy$, $10.9Gy$ and $10.4\ Gy$ respectively. The distributions (median(minimum,maximum)) of $D_{95\%\ PTV}$, $D_{10\%\ Ur}$, $D_{1cc\ Rec}$ and $D_{1cc\ Bl}$ in the case with error in needle placement were $19.4(16.9, 20.9)Gy$, $19.5(15.2, 26.8)Gy$, $10.9(9.4, 12.7)Gy$ and $10.5(9.7, 11.3)Gy$ respectively without re-optimization and $19.7(18.4, 20.3)Gy$, $19.4(15.8, 21.4)Gy$, $11.1(9.9, 12.6)Gy$ and $10.8(10.4, 11.7)Gy$ respectively with re-optimization. Without re-optimization, 42% of the dose plan with error in needle placement were clinically acceptable without re-optimization, as compared to 94% for the scenario with re-optimization (values depicted in Table 3.1).

3.4 Discussion

In this article, a dose plan adaptation strategy for MR-guided HDR prostate brachytherapy with feedback on the needle positioning errors is presented. Before each insertion, a needle track is selected among the ones proposed by the dose plan. Furthermore, after each needle insertion (and possible deviation of the needle during insertion), a re-optimization of the dose plan (remaining needle track angulations, dwell positions and dwell times) is performed.

The development of adaptative planning in brachytherapy is recent: in locally advanced cervical cancer, Image Guided Adaptive Brachytherapy (IGABT) has shown promising impact on treatment outcome, and is currently being implemented in several medical centers (Pötter *et al* 2006, Pötter *et al* 2011, Lindegaard *et al* 2013) with MRI as the imaging modality of choice. Regarding prostate cancer, Cunha *et al* (2010) developed a workflow incorporating a MR stealth robot and an Inverse Planning Simulated Annealing (IPSA) algorithm for permanent seed-implants.

Regarding the selection of the needle tracks, it is interesting to note that the impact of an inaccurate needle insertion on the dose plan quality may be different depending on the needle track chosen. In the case presented in Figure 3.4, although the dose plan without error during insertion is clinically acceptable (see green horizontal line), an error of angulation during insertion of the needle may result in a great decrease of the dose plan quality: in particular, if the needle is inserted with an error in *needle track* 2, 3 or 4, the dose plan after insertion may become not clinically acceptable if no re-optimization of the dose plan parameters is done. In addition, these simulation results indicate that the order in which needles are

inserted may play a crucial role. A complete comparison of different strategies with respect to needle selection is beyond the scope of the current work, but should be addressed to achieve robust and reproducible adaptive dose delivery.

Furthermore, the study shows that the proposed re-optimization strategy on the needle positioning results in dose plans with a significantly better quality compared to the scenario without re-optimization. The values of the dose parameters presented for the two cases in Figure 3.5 showed a better distribution with re-optimization compared to the situation without re-optimization: fewer cases showed dose parameters outside of the clinical constraints in the situation with re-optimization compared to the case without re-optimization. Furthermore, for all cases of the planning study, the percentages of clinically acceptable dose plans were on average 47.8% without re-optimization and 86.4% with re-optimization (*cf.* Table 3.1). This points out that the re-optimization procedure is able to compensate for the angulation error during insertion. Finally, all the simulations and dose re-plannings of the validation study were done completely automatically (no human was involved in the process). The algorithm was implemented in Matlab 2015. The computation time of the selection of the needle (**Task 2**) and the re-optimization of the dose plan (**Task 5**) took less than $100s$. The re-optimization procedure is therefore eligible for intra-operative use.

It is also relevant to note that the MR images used for the simulations of this study are intra-operative images of patients who underwent HDR prostate brachytherapy as monotherapy in a single fraction at the UMCU. Therefore, the large prostate and PTV volumes depicted in Table 3.1 are due to swelling of the prostate after insertion of the needles.

In the presented study, an open number of needle insertions was chosen. In practice, a compromise has to be found: It is clear that the more needle insertions there are, the better the dose distribution will be. However, the influence of adding one or more needle insertions may lead to additional toxicity: Vargas *et al* (2005) and Boyea *et al* (2007) showed the urinary toxicity following HDR brachytherapy is significantly increased by using more than 14 needle insertions. For those reasons, we think that an automatic determination of the number of needle insertions requires additional works and we decided to perform the simulations for different number of needle insertions (from 4 to 12). A range of 4–12 needle insertions was chosen because, for this range, clinically acceptable dose plans for all patients were obtained.

The strategy proposed in this manuscript supposed that the position of the needle at **Task 4** can be measured. For that, Bergeles *et al* (2012) proposed a needle tracking method using MRI: needle tracking is achieved using non-selective radio frequency pulses and balanced gradient readouts. Furthermore, Henken *et al* (2013) showed that Optical Shape Sensing (OSS) could be a good alternative to MR-based needle tracking when the update rate in MRI is too low for high-precision robotic needle steering. OSS may also be valuable in case signal voids from blood vessels, calcifications or other artefacts make image interpretation dif-

ficult.

Although the optimizer described here was implemented with the point source approximation for simplicity of calculation (cf. Eq. 3.10), the proposed method allows the use of more precise source models such as the line source approximation.

In practice of HDR brachytherapy using parallel template geometry, bones interferences can impose restrictions in the prostate gland volume. A limitation of this study is that the problem of bones interference has not been taken into account. However, since the center of rotation of the setup can be chosen such that the divergent needle tracks avoid the bones to have maximal access to the prostate gland, the authors expect less restriction in prostate gland volume using a divergent needle pattern in comparison to a parallel needle geometry.

Moreover, only the needle angulation errors were taken into account in this study although more complex problems may occur during insertion such as needle bending or modification of the patient anatomy during treatment. However, the proposed pipeline is compatible with a re-optimization of the dose plan parameters after each insertion of the needle while taking into account those issues thanks to the proposed experimental setup: in terms of hardware, the robotic device developed in our institution is designed such that the needle can be inserted under MRI guidance, and, in terms of software, the calculation time of the optimizer is eligible for intra-operative use. The development of such feedback strategy for both needle positioning and anatomy changes will be studied in future work.

3.5 Conclusion

A dose plan adaptation strategy for HDR prostate brachytherapy with feedback on the needle position was proposed in this manuscript. This procedure can be used with the single needle MR-compatible robot developed at the UMCU. The validation study of this strategy, based on simulations, shows the importance of evaluating and compensating the needle positioning errors during HDR prostate brachytherapy intervention. Without dose plan adaptation, the dose delivered to the patients may not reach the clinical constraints. Finally, the MR-guidance setup and the computation time of the re-optimization procedure (less than $100s$) are eligible for intra-operative use.

Appendix. Numerical implementation of the re-optimization of the dwell times

For mathematical simplification, we will consider in this Appendix an anatomy composed by the PTV and a single Organ At Risk (OAR). The extension to multiple OARs will then be straightforward. In the following, N_{source}^{tot} is the total number of active source positions of the dose plan, t_n and $d_n(\boldsymbol{r})$ ($n \in [1, N_{source}^{tot}]$) are the dwell time and dose rate at each active source position, respectively. Let sup-

pose N_{source}^{opt} is the total number of dwell-times to re-optimize and $(t_1 \cdots t_{N_{source}^{opt}})$ are the dwell times to optimize $((t_{N_{source}^{opt}+1} \cdots t_{N_{source}^{tot}})$ are therefore fixed).

The dose $D(\boldsymbol{r}, p)$ received at $\boldsymbol{r}$ can be expressed as follows:

$$D(\boldsymbol{r}, p) = \sum_{n=1}^{N_{source}^{opt}} d_n(\boldsymbol{r}) t_n + \sum_{n=N_{source}^{opt}+1}^{N_{source}^{tot}} d_n(\boldsymbol{r}) t_n \tag{3.11}$$

The approach takes into account the already delivered dose as follows: the final objective is a high PTV coverage while the OAR is spared as much possible. A way to reach this goal is to approximate the dose to a certain value D_{PTV} in the PTV and to 0 in the OAR. That way, the dose distribution will tend to be as homogeneous as possible in the PTV. Consequently, this strategy will contribute to limit the hotspots. The weight coefficients are supposed constant for the PTV and OAR: They are noted ω_{PTV} and ω_{OAR_l} respectively. In a discrete space, the cost functions $C_{PTV}(p)$ and $C_{OAR}(p)$ of the PTV and the OAR can be defined by referring to the definition of $C(p)$ in Eq. 3.8, as follows:

$$C_{PTV}(p) = \frac{\omega_{PTV}}{V_{PTV}} \sum_{\boldsymbol{r} \in PTV} [D(\boldsymbol{r}, p) - D_{PTV}]^2 \tag{3.12}$$

$$C_{OAR}(p) = \frac{\omega_{OAR}}{V_{OAR}} \sum_{\boldsymbol{r} \in OAR} D(\boldsymbol{r}, p)^2 \tag{3.13}$$

These cost functions were divided by the volume of the organs (V_{PTV} and V_{OAR} to avoid volume dependency in the optimization. Furthermore, the basic cost function could be expressed as:

$$C(p) = C_{PTV}(p) + C_{OAR}(p) \tag{3.14}$$

The optimal values of ω_{OAR}, ω_{PTV} and D_{PTV} are obviously dependent of the anatomy of the patient. Therefore, in the following sections, the algorithm to minimize $C(p)$ for a given value of ω_{OAR}, ω_{PTV} and D_{PTV} is presented. Then, the method to determine the optimal values of ω_{OAR}, ω_{PTV} and D_{PTV} according to the patients anatomy is described.

3.A.1 Solution using matrix inversion

To find $(t_1 \cdots t_{N_{source}^{opt}})$ which minimizes $C(p)$ with the additional condition that for all $n \in [1, N_{source}^{opt}]$, $t_n \geq 0$, we modify the cost function of the OAR as follows:

$$C_{OAR}(p) = \frac{\omega_{OAR}}{V_{OAR}} \sum_{\boldsymbol{r} \in OAR} \left(\sum_{n=1}^{N_{source}^{opt}} [d_n(\boldsymbol{r}) t_n]^2 + \sum_{n=N_{source}^{opt}+1}^{N_{source}^{tot}} [d_n(\boldsymbol{r}) t_n]^2 \right) \tag{3.15}$$

By modifying the OARs cost function, $C_{OAR}(p)$ will not be null through "destructive interference" effects between the dwell times and most of the unphysical negative results solutions are therefore excluded.

From now, we note $\tilde{\omega}_{PTV} = \frac{\omega_{PTV}}{V_{PTV}}$, $\tilde{\omega}_{OAR} = \frac{\omega_{OAR}}{V_{OAR}}$ and the already delivered dose $D_{deliv}(\boldsymbol{r}) = \sum_{n=N_{source}^{opt}+1}^{N_{source}^{tot}} d_n(\boldsymbol{r})t_n$. We then develop the same demonstration described by Goldman *et al* (2009). The minimum of $C(p)$ is obtained by the following condition:

$$\forall j \in [1, N_{source}^{opt}],\ \frac{\partial C(p)}{\partial t_j} = 0 \tag{3.16}$$

Using Eq. 3.14, we obtain $\forall j \in [1, N_{source}^{opt}]$:

$$\begin{aligned} 0 = 2\tilde{\omega}_{PTV} \sum_{\boldsymbol{r}\in PTV} d_j(\boldsymbol{r}) \left[\sum_{n=1}^{N_{source}^{opt}} d_n(\boldsymbol{r})t_n + D_{deliv}(\boldsymbol{r}) - D_{PTV} \right] \\ + 2\tilde{\omega}_{OAR} \sum_{\boldsymbol{r}\in OAR} d_j(\boldsymbol{r})^2 t_j \end{aligned} \tag{3.17}$$

By exchanging the order of summations, Eq. 3.17 becomes:

$$\begin{aligned} \sum_{n=1}^{N_{source}^{opt}} t_n \left[\tilde{\omega}_{OAR} \sum_{\boldsymbol{r}\in OAR} d_j(\boldsymbol{r})d_n(\boldsymbol{r})\delta_{nj} + \tilde{\omega}_{PTV} \sum_{\boldsymbol{r}\in PTV} d_j(\boldsymbol{r})d_n(\boldsymbol{r}) \right] \\ = \tilde{\omega}_{PTV} \sum_{\boldsymbol{r}\in PTV} d_j(\boldsymbol{r})[D_{PTV} - D_{deliv}(\boldsymbol{r})] \end{aligned} \tag{3.18}$$

where δ_{nj} is the Kronecker delta function. Therefore, the values of dwell times can be determined by a matrix inversion:

$$T = \alpha^{-1}\beta \tag{3.19}$$

where $T = (t_j)_{j\in[1,N_{source}^{opt}]}$ is the vector of dwell times (vector of N_{source}^{opt} elements), α is a square symmetrical positive matrix of $[N_{source}^{opt}, N_{source}^{opt}]$ elements, and β is a vector of N_{source}^{opt} elements such that:

$$\begin{aligned} &\forall (j,n) \in [1, N_{source}^{opt}]^2, \\ &\quad \alpha_{jn} = \tilde{\omega}_{OAR} \sum_{\boldsymbol{r}\in OAR} d_j(\boldsymbol{r})d_n(\boldsymbol{r})\delta_{nj} + \tilde{\omega}_{PTV} \sum_{\boldsymbol{r}\in PTV} d_j(\boldsymbol{r})d_n(\boldsymbol{r}) \end{aligned} \tag{3.20}$$

$$\begin{aligned} &\forall j \in [1, N_{source}^{opt}], \\ &\quad \beta_j = \tilde{\omega}_{PTV} \sum_{\boldsymbol{r}\in PTV} d_j(\boldsymbol{r})[D_{PTV} - D_{deliv}(\boldsymbol{r})] \end{aligned} \tag{3.21}$$

3.A.2 Exhaustive search of the weight coefficients (ω_{PTV}, $\omega_{OAR_{1\cdots N_{OAR}}}$) and the dose approached for the PTV (D_{PTV})

It is interesting to note that the matrix inversion in Eq. 3.19 is low time consuming. It is therefore possible to find the optimal value of $(\omega_{OAR_l})_{l\in[1,N_{OAR}]}$, ω_{PTV} and D_{PTV} using an exhaustive search. Therefore, we propose to calculate the dwell times using Eq. 3.19 for different combinations of $(\omega_{OAR_l})_{l\in[1,N_{OAR}]}$, ω_{PTV} and D_{PTV} within the same ranges described by Borot de Battisti *et al* (2015) which are:

$$\begin{cases} D_{PTV} \in \{20, 21, \cdots, 79, 80\} \\ \log_{10}(\omega_{PTV}) \in \{0, 1, \cdots, 9, 10\} \\ \forall l \in [1, N_{OAR}],\ \log_{10}(\omega_{OAR_l})\{0, 1, \cdots, 9, 10\} \\ \sum_{l=1}^{N_{OAR}} \log_{10}(\omega_{OAR_l}) + log_{10}(\omega_{PTV}) = 10 \end{cases} \tag{3.22}$$

The exhaustive search of $(\omega_{OAR_l})_{l\in[1,N_{OAR}]}$, ω_{PTV} and D_{PTV} provides several dose plans. For each obtained dose plan, the metric E, which represents the quality of the dose plan, is calculated (see Eq. 3.2). The optimal dose plan is then automatically determined by selecting the dose plan with the highest value of E.

CHAPTER 4

Fiber Bragg gratings (FBG)-based sensing for real-time needle tracking during MR-guided brachytherapy

The following chapter is based on:
Borot de Battisti M, Denis de Senneville B, Maenhout M, Hautvast G, Binnekamp D, Lagendijk J J W, Van Vulpen M and Moerland M A 2016 Fiber Bragg gratings-based sensing for real-time needle tracking during MR-guided brachytherapy *Med. Phys.* **43** 5288–97

Abstract

The development of MR-guided HDR brachytherapy is under investigation due to the excellent tumor and OARs visualization of MRI. However, MR-based localization of needles (including catheters or tubes) has inherently a low update rate and the required image interpretation can be hampered by signal voids arising from blood vessels or calcifications limiting the precision of the needle guidance and reconstruction. In this manuscript, a new needle tracking prototype is investigated using Fiber Bragg Grating (FBG)-based sensing: this prototype involves a MR-compatible stylet composed of three optic fibers with nine sets of embedded FBG sensors each. This stylet can be inserted into brachytherapy needles and allows a fast measurement of the needle deflection.This study aims to assess the potential of FBG-based sensing for real-time needle (including catheter or tube) tracking during MR-guided intervention. First, the MR compatibility of FBG-based sensing and its accuracy was evaluated. Different known needle deflections were measured using FBG-based sensing during simultaneous MR-imaging. Then, a needle tracking procedure using FBG-based sensing was proposed. This procedure involved a MR-based calibration of the FBG-based system performed prior to the interventional procedure. The needle tracking system was assessed in an experiment with a moving phantom during MR imaging. The FBG-based system was quantified by comparing the gold-standard shapes, the shape manually segmented on MRI and the FBG-based measurements. The evaluation of the MR compatibility of FBG-based sensing and its accuracy shows that the needle deflection could be measured with an accuracy of $0.27mm$ on average. Besides, the FBG-based measurements were comparable to the uncertainty of MR-based measurements estimated at half the voxel size in the MR image. Finally, the mean(standard deviation) Euclidean distance between MR and FBG-based needle position measurements was equal to $0.79mm(0.37mm)$. The update rate and latency of the FBG-based needle position measurement were $100ms$ and $300ms$ respectively. The FBG-based needle tracking procedure proposed in this manuscript is able to determine the position of the complete needle, under MR-imaging, with better accuracy and precision, higher update rate and lower latency compared to current MR-based needle localization methods. This system would be eligible for MR-guided brachytherapy, in particular for an improved needle guidance and reconstruction.

4.1 Introduction

HDR brachytherapy involves placement of needles (including catheters or tubes) into or close to the tumor, through which a radioactive source (*e.g.* Ir-192) irradiates the tumor for certain times at different positions according to a calculated dose plan (Venselaar *et al* 2012). In usual clinical practice, a dose plan is made at the beginning of the brachytherapy procedure (Borot de Battisti *et al* 2015, Gorissen *et al* 2013, Holm *et al* 2013). This process involves selecting the appropriate needle positions in order to achieve an optimal dose distribution with a high irradiation dose to the tumor and the lowest possible dose to surrounding healthy tissues. However, two major events are likely to modify the pre-planned dose distribution during the interventional process. First, needle positioning errors may occur: In the case of HDR prostate brachytherapy, Straßmann *et al* (2011) showed that the average needle positioning accuracy on prostate was $2.7 \pm 0.7mm$ with

manual template-guided insertion and $1.8 \pm 0.6mm$ with robot-assisted positioning. Second, accidental shift (movement of patient), peristaltic change, bladder filling (Cengiz *et al* 2008, Hung *et al* 2012) or internal movement of organs and tissue edema related to the trauma of the needle insertion (Hoskin *et al* 2003, Stone *et al* 2002, Lagerburg *et al* 2006) can cause anatomical modifications (and needle position deviations) during the intervention. Those events can lead to uncertainties and errors in the delivered dose to the PTV and OARs (Kirisits *et al* 2014). To reduce those uncertainties, two methods are possible: (1) restraining at maximum the needle positioning errors and (2) dynamically updating the dose plan with feedback on the actual catheter locations as shown by Borot de Battisti *et al* (2016a). For that, the real-time determination of the needle position (consisting of tracking the needle during insertion and reconstructing the needle after insertion) is warranted.

For an increasing number of brachytherapy applications, MRI is the imaging modality of choice due to excellent tumor and OARs visualization (Pötter *et al* 2009, Groenendaal *et al* 2010, Dimopoulos *et al* 2012, Damato *et al* 2015). De Oliviera *et al* (2008) proposed a needle tracking method using MRI in the case of endorectal biopsy device: It consists of applying a pulse sequence in order to follow a passive marker attached to the MR biopsy device holder. With this method, the position of the needle axis is automatically identified using a phase-only cross-correlation algorithm. The total duration of the tracking sequence is about 10 min. More recently, an active MR-TRacking (MRTR) system was developed to provide accurate and rapid localization of interstitial brachytherapy catheters (Wang *et al* 2015). This system consists of integrating multiple microcoils into the metallic stylets that are used to advance the catheters into tissue. The catheter trajectory is reconstructed by pulling out the stylet from the catheter while the microcoils are tracked using a dedicated MR sequence. The mean 3D error of the catheter path was found to be $1.5mm \pm 0.5mm$ for an acquisition time of $\sim 10s$ per catheter. In practice, the update rate of the needle position measurement in MRI may be too low and the latency too high for high-precision needle steering during the interventional procedure.

As an alternative to MR-based needle tracking, the needle shape can also be measured using a MR-compatible stylet with embedded fiber Bragg gratings (FBG) sensors. Park *et al* (2010) and Henken *et al* (2014) were able to reconstruct the needle shape with high accuracy, but both only assessed in-plane needle deflection in free space. Roesthuis *et al* (2014) validated the accuracy of needle tip measurements using FBG sensors for out-of-plane (3D) deflections in both free space and a soft tissue simulant with a maximum out of plane error of $1.66mm$. Besides, Park et al. and Henken et al. both estimated needle curvature by measuring the curvature at two locations along the needle shaft (their stylets were composed of three fibers with two sets of FBG sensors each). Roesthuis et al. used three fibers with four sets of FBG sensors each, which enabled to measure needle curvature at four different locations along the needle shaft. In this manuscript, an upgraded prototype is investigated: it includes an MR-compatible stylet involving three fibers with nine embedded sets of FBG sensors each. This FBG-based

tracking system has potentially an improved accuracy and precision, higher update rate and lower latency compared to MR-based needle tracking. Furthermore, the FBG-based sensing stylet is composed of MR-compatible materials which do not interfere with MR-imaging. However, the major issue of FBG-based sensing is that it only measures the deflection of the needle (*i.e.* the relative shape in the needle coordinate system). In order to assess the needle shape in the physical spatial coordinate system, the position and orientation of the stylet at, at least, one point of the stylet must be known.

This study aims to assess the potential of FBG-based sensing for real-time needle (including catheters or tubes) tracking during MR-guided intervention. The main contribution of this work is:

- To evaluate the MR-compatibility and accuracy of the needle deflection measurement using FBG-based sensing.
- To propose an experimental protocol designed to assess needle tracking using FBG-based sensing. This protocol involves (1) the fixation in space of the stylet base and (2) a MR-based calibration which aims to determine the position and orientation of the stylet at the fixation point. This calibration is performed once and for all, prior to the measurement of the needle position. The authors underline that in practice, the proposed protocol is optional if the position and orientation of the stylet at one point is already known.
- To assess the FBG-based needle tracking procedure under MR-imaging in a phantom experiment.

Special attention will be paid to the accuracy, precision, update rate and latency of the proposed needle tracking method.

4.2 Methods

First, we describe the MR-compatible FBG-based sensing device (*cf.* section 4.2.1). An inherent deficit of the FBG-based sensing is reported in this section: In order to assess the needle position in the physical spatial coordinate system, the position and orientation of the stylet at one or more stylet points are mandatory. To achieve this, we propose an experimental protocol which involves the fixation of the stylet base and a MR-based calibration performed prior to the measurement of the needle position (*cf.* section 4.2.2). The experiments to evaluate the MR compatibility of the FBG-based sensing are described in section 4.2.3.1: The accuracy of the needle deflection measurement is evaluated under on-line MRI. An experiment, which aims to assess the proposed FBG-based needle tracking procedure, is described in section 4.2.3.2: this experiment involves the tracking of needles inserted in a moving phantom.

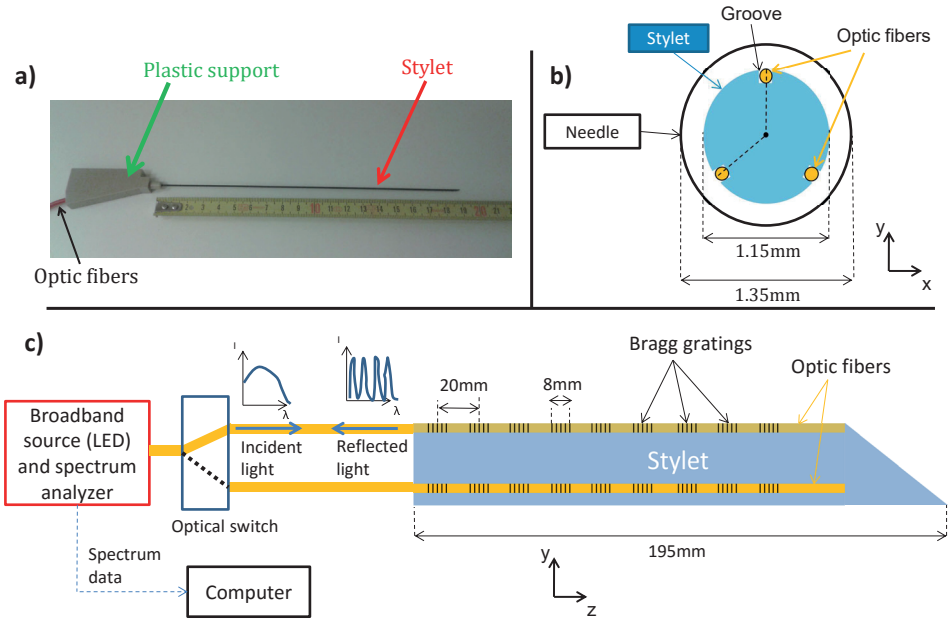

Figure 4.1: (a) presents a picture of the FBG-based sensing stylet. (b) is a schematic of a transverse slice of the FBG-based sensing stylet inserted in the needle. (c) presents the longitudinal schematic of the stylet.

4.2.1 MR-compatible FBG-based sensing device

In the scope of this study, a FBG-based sensing prototype was used to determine the deflection of a brachytherapy needle in real-time. This FBG-based sensing prototype was composed of a MR-compatible stylet that can be inserted inside the lumen of the needle. The length of the stylet was $195mm \pm 1mm$ and the diameter $1.15mm \pm 0.05mm$ (*cf.* Fig. 4.1). Three grooves were situated parallel to the central axis of the stylet, at 120° intervals. Three fibers (noted F_1, F_2 and F_3) were embedded inside the grooves such that F_1, F_2 and F_3 were at the same distance from the central axis of the stylet. Each fiber F_i ($i \in [1,3]$) had 9 FBGs (noted $FBG_1^{(i)}$,$\cdots$,$FBG_9^{(i)}$). Those FBGs were separated by intervals of $20mm$ along the stylet's length such that, $\forall k \in [1,\cdots,9]$, $FBG_k^{(1)}$, $FBG_k^{(2)}$ and $FBG_k^{(3)}$ had the same longitudinal position along the stylet. By measuring the wavelength of the light reflected by the FBGs, the 3D curvature and temperature along the stylet can be determined. Knowing the 3D curvature, it is possible to reconstruct the stylet deflection (and consequently the needle deflection when the stylet is inserted inside the needle) at regularly sampled position (every $1mm$). The procedure to reconstruct the 3D needle deflection by measuring the reflected FBG wavelengths was described by Roesthuis *et al* (2014) and Park *et al* (2010).

To determine the amplitude of the reflected wavelength, a measurement device for FBG sensors was used (*FBG-scan 804D, FBGS, Geel, Belgium*). This device

is composed of broadband LED source to light the optical fibers, a spectrum analyzer (monochromator) to measure the reflected wavelength and a fast optical switch which alternatively routes the 3 optical fibers to the LED source and spectrum analyzer. A computer controls the device and automatically determines the stylet's deflection using a LabVIEW program. This program could also determine the update rate and latency of the needle deflection measurement, which were dependent of the switching speed, the light integration time of the monochromator and the needle deflection computation time.

With this system, we can monitor the deflection of the needle. To derive the position of the whole needle, the position and orientation of the stylet at one or more stylet points need to be determined. This can be done using a MR-based calibration, as follows.

4.2.2 MR-based calibration of the FBG-based measurement

In the scope of this study, an experimental protocol is proposed in order to assess the FBG-based needle tracking procedure under MR-imaging. In this set-up, the base of the stylet is fixed in space (for example with a clamp) such that this point cannot move or rotate. A MR-based calibration is then performed prior to the measurements of the needle position in order to determine the position and orientation of the stylet at the fixation point (called the "reference point" in the scope of this study). Once the calibration is done, the tracking of the needle can be performed without having to subsequently re-apply the calibration. This section describes this MR-based calibration.

If we assume that no image distortion occurred during the MR-imaging, the axis X_{MR}, Y_{MR} and Z_{MR} of the MR image are coincident with the axis X, Y and Z of the physical spatial coordinate system. A way to determine the position and orientation of the stylet at the reference point is to register this point to the X_{MR}, Y_{MR} and Z_{MR}-coordinate system. To achieve this, we propose the following procedure:

1. Several (at least 2) different needle shapes are measured with FBG-based sensing during simultaneous MR imaging. For that, we can insert the stylet into two needles (with different shapes) introduced beforehand into a phantom.

2. The MR-based needle shapes stem from a segmentation step.

3. A rigid registration of the MR and the FBG-based measurements of the needle shapes is then performed. The rigid registration of the MR and FBG-based measurement consists of determining 6 parameters: 3 parameters of translations along X_{MR}, Y_{MR} and Z_{MR} (noted t_x, t_y and t_z) and 3 angles of rotation about X_{MR}, Y_{MR} and Z_{MR} (noted θ_x, θ_y and θ_z). To find those parameters, paired points between the MR and the FBG-based measurements at regular sample positions along the needle are determined.

A gradient driven optimization is then performed to find the values of t_x, t_y, t_z, θ_x, θ_y and θ_z. This gradient driven optimization consists of minimizing the distances between those paired points after transformation (translations and rotations). The method to perform this rigid registration is detailed in the Appendix.

4. Once MR and FBG-based measurements are registered, the determination of the stylet position and orientation at the reference point in the X_{MR}, Y_{MR} and Z_{MR}-coordinate system is straight forward.

The proposed method involves an immobilization of the stylet base and therefore may be limiting in a clinical workflow. This issue will be discussed in section 4.4.

4.2.3 Experimental evaluation of FBG-based sensing for real-time needle tracking during MR-guided intervention

This section presents three experiments which aim:

- To assess the accuracy and MR-compatibility of the FBG-based sensing system (*cf.* section 4.2.3.1).
- To evaluate the accuracy, precision, update rate and latency of the complete tracking device under MR imaging using the MR-based calibration presented in section 4.2.2 (*cf.* section 4.2.3.2).

In the following experiments, the 3D MR images were acquired with a 1.5T MR-scanner using a 3D Spectral Presaturation with Inversion Recovery (SPIR) sequence ($TR = 2.9ms$, $TE = 1.44ms$, $voxel\ size = 1.2 \times 1.45 \times 1mm^3$, number of signal average = 2). This sequence was chosen because it is commonly used to reconstruct needle in practice of HDR brachtherapy at the UMCU. The employed field of view was approximately $60 \times 250 \times 250mm^3$ in order to image the whole length of the needle. The scan time to cover the whole volume was 5 minutes and 37 seconds.

4.2.3.1 Accuracy and MR compatibility of FBG-based sensing

To evaluate the accuracy and MR-compatibility of the FBG-based tracking system, we performed the two following experiments:

First, to evaluate the accuracy during MR-imaging, a needle (titanium needle $1.9mm \times 200mm$ from *Elekta, Veenendaal, The Netherlands*) was placed inside the MR scanner bore and its shape was imposed by a specially designed plastic mold with different known 2D paths (*cf.* Fig. 4.2). For path 1, 2 and 3, the deflection of the needle was measured by FBG-based sensing during MR-imaging along 4 orientations (*i.e* 0°, 90°, 180°, 270°), by rotating the needle along its longitudinal axis (*cf.* Fig. 4.3a). The error between the FBG-based measurement and the gold standard shape was then calculated.

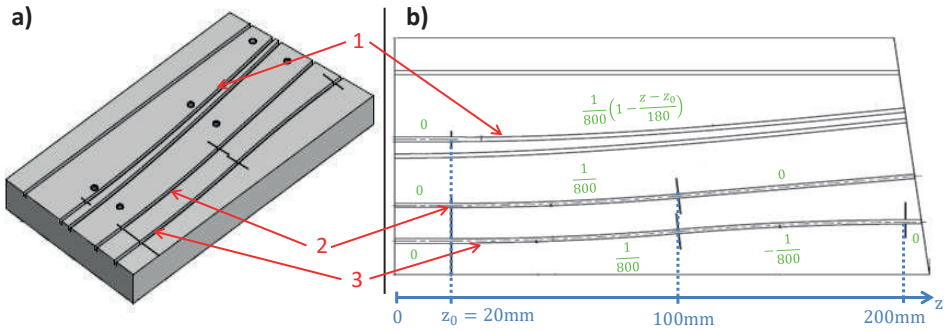

Figure 4.2: (a) presents the schematic in 3 dimensions of the mold used. The 3 paths used for the experiment are noted 1, 2 and 3. (b) is a schematic of the upper view of the mold. The curvatures (in mm^{-1}) of the paths 1, 2 and 3 are depicted in green.

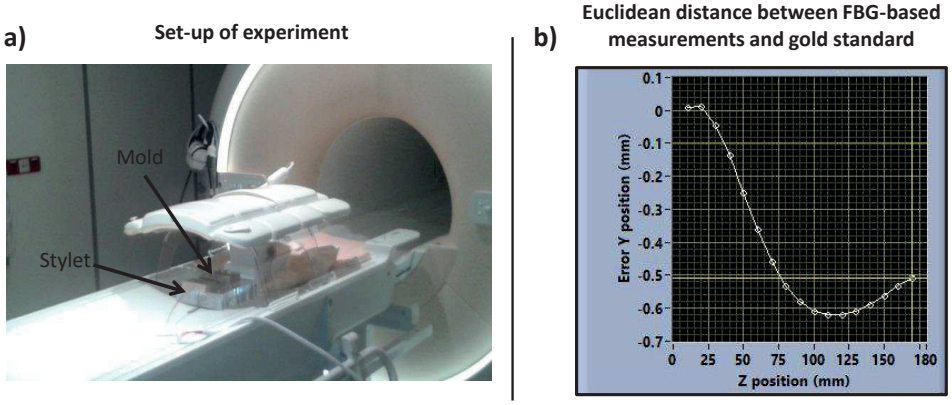

Figure 4.3: (a) is a picture of the experimental set-up for the gold standard test using the mold inside the MR scanner bore (the set-up was shifted out of scanner for photograph). (b) presents the typical example of the Euclidean distance between a known shape and the FBG-based measurement.

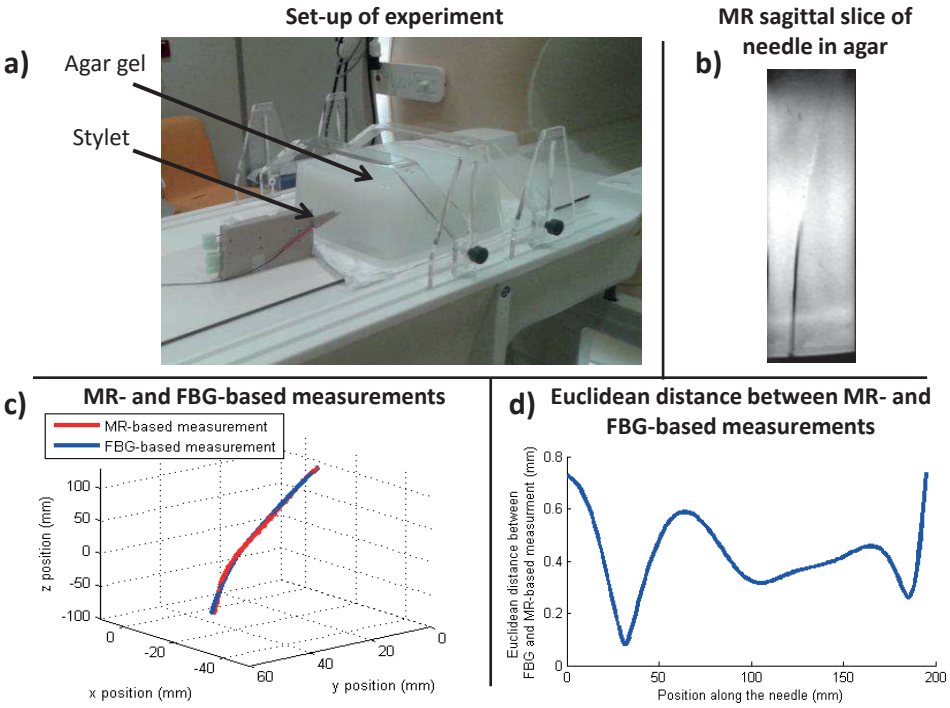

Figure 4.4: (a) presents a picture of the experimental set-up consisting of evaluating the impact of FBG-based sensing measurement on MR-imaging (the set-up was shifted out of scanner for photograph). (b) shows the MR image of one needle, (c) represents the MR and the FBG-based measurement after rigid registration and (d) the Euclidean distance between the MR and FBG-based measurement along the needle.

Second, to evaluate the impact of FBG-based sensing measurement on MR-imaging, four plastic ProGuide 6F Sharp needles (*Elekta, Veenendaal, The Netherlands*) with a length of 195*mm* were introduced in an agar phantom. The corresponding needle shapes were measured with FBG-based sensing during simultaneous MR imaging (*cf.* Fig. 4.4a and b). The MR-based needle shapes stem from a manual segmentation step. A rigid registration of the obtained MR and the FBG-based needle measurement was then performed using the algorithm described in the Appendix. After registration, the error between the FBG and MR-based needle position measurement was assessed: For this purpose the Euclidean distances between the paired points (see subsection 4.A.1 of the Appendix) were calculated.

4.2.3.2 Assessment of the proposed FBG-based needle tracking system

The following experiment was performed to assess the complete needle tracking procedure using the calibration protocol described in section 4.2.2:

Step 1: A flexible needle of $93mm$ (ProGuide 6F Sharp by *Elekta, Veenendaal, The Netherlands*) was placed into a prostate phantom (CIRS, Model 053-I, Ultrasound Prostate Training Phantom).

Step 2: The plastic holder of the FBG-based sensing device (*cf.* Fig. 4.1a) was fastened to a support fixed on the MR table (*cf.* Fig. 4.5a). That way, the stylet base was fixed in space with no possibility of translation or rotation.

Step 3: The needle shape was measured with FBG-based sensing during simultaneous MR imaging in five different configurations: the phantom was moved for each configuration by approximately one centimeter, along the left-right axis. That way the needle position was different in each configuration.

Step 4: Two of those configurations were used to perform the MR-based calibration and determine the position and orientation of the stylet base (see section 4.2.2).

Step 5: The 3 other configurations were used to assess the complete FBG-based tracking system: the FBG and MR-based needle position measurements were compared. For this purpose, paired MR and FBG-based points were determined at regular interval ($1mm$) along the needle using the algorithm described in subsection 4.A.1 of the Appendix and their corresponding Euclidean distances were calculated.

To assess the repeatability of the results, Step 4 and 5 were repeated for all possible pairs of configurations.

4.3 Results

4.3.1 Accuracy and MR compatibility evaluation of the FBG-based sensing

This section presents the results of the experiments which aim to assess the accuracy and MR-compatibility of the FBG-based tracking system (the experimental method is described in section 4.2.3.1). For all tested needle shapes, the average difference between the FBG-based measurement and the gold standard values (known shapes given by the mold) was $0.27mm$. A characteristic example (path 1 of the mold) is presented in Fig. 4.3b: the average(minimum, maximum) absolute difference between the FBG-based measurement and the known shape was $0.42mm(0.01mm, 0.62mm)$. For the second experiment with 4 needles in agar phantom, the mean Euclidean distance between MR and FBG-based paired points along the needle was $0.42mm$ on average over the 4 tested needles. A typical example is presented on Fig. 4.4c and d: the average (minimum,maximum) Euclidean distance between MR and FBG-based paired points along the needle was $0.42mm(0.08mm, 0.74mm)$.

4.3.2 Assessment of the proposed FBG-based needle tracking system

This section presents the results of the experiment which consists of validating the complete needle tracking system. The experimental method is described in section 4.2.3.2. Over all tested scenarios, the average (standard deviation) Euclidean distance between MR and FBG-based paired points along the needle was $0.79mm(0.37mm)$. In particular, for the paired points at the tip of the needle, the average(standard deviation) Euclidean distance was $1.10mm(0.45mm)$. The update rate and the latency of the needle position measurement were around $100ms$ and $300ms$, respectively. The latency and update rate include the integration time of the light received by the monochromator ($90ms$) and the computation time of the needle deflection (order of magnitude of a few milliseconds). A typical example is presented on Fig. 4.5c and d: the average(minimum, maximum) Euclidean distance between MR and FBG-based needle position measurements along the needle configurations 2, 3 and 5 (which corresponds to the configurations used to assess the needle tracking system) were $0.76mm(0.72mm, 0.93mm)$, $0.94mm(0.87mm, 1.11mm)$ and $0.79mm(0.63mm, 0.93mm)$ respectively. The average(minimum, maximum) Euclidean distance of the needle tip measurements was $0.84mm(0.63mm, 1.11mm)$. The largest deviations between the FBG and MR-based measurements were situated close to the outer borders of the phantom.

4.4 Discussion

This manuscript presents a FBG-based sensing device which is able to track and reconstruct a needle (including catheter or tube) during a medical procedure. This device can track a needle deflection with a high accuracy ($0.27mm$ on average) in an MR environment. In addition, this report shows that the average Euclidean distance between MR and FBG-based measurements of the needle position after registration was comparable to the uncertainty of MR-based measurements (corresponding to the uncertainty of the manual segmentation) estimated at half the voxel size in the MR image. This indicates that the FBG-based sensing device is not significantly influenced by the MR environment. Finally, the FBG-based needle tracking device can measure the needle position with an accuracy of $0.79mm$ and a precision (standard deviation) of $0.37mm$ on average in comparison to the MR-based measurement. In particular, the accuracy and precision of the needle tip is $1.10mm$ and $0.45mm$ respectively. Moreover, the update rate of the needle position measurement is $100ms$ and its latency $300ms$.

The inaccuracy related to MR-based measurement can have 2 origins: Inaccuracy in the manual needle segmentation and distortion of the MR-images. Regarding the inaccuracy in the manual needle segmentation, the error was estimated to half the voxel size of the MR images ($voxel\ size = 1.2 \times 1.45 \times 1mm^3$). Regarding the distortion of the MR-image, a quality assessment of the MR was performed prior to the measurements using an ACR phantom with a length of 148 mm and a diameter of 190 mm. Based on this quality assessment, the maximum error found at the border of the ACR phantom was less than 1mm. Since all MR-

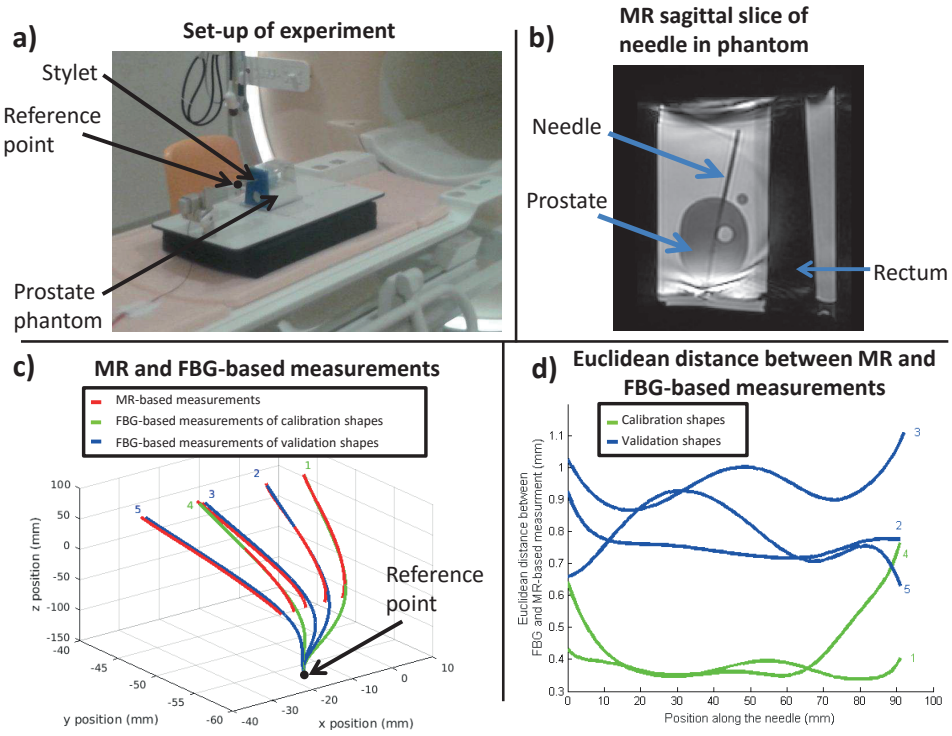

Figure 4.5: (a) presents the set up of the experiment consisting of assessing the FBG-based needle tracking system (the set-up was shifted out of scanner for photograph). (b) is a MR sagittal slice of the phantom with the inserted needle. (c) represents the MR and the FBG-based measurement after rigid registration. The two configurations used for the calibration of the reference point are in green, the configurations to validate the protocol are in blue. (d) represents the Euclidean distance between the MR and FBG-based tracking measurement along the needle.

images of the experiments presented in this manuscript were within 100mm from the MR isocenter, negligible errors are expected related to MR-image distortion. The accuracy of the MR-based measurement was therefore estimated to half the voxel size of the MR images.

Since the FBG-based sensing stylet is composed of MR-compatible materials, this device is eligible to be used in a MR environment. Another method eligible in a MR environment is described by Wang *et al* (2015). In this study, a real time active MR tracking method has been proposed. Multiple microcoils are integrated into metallic stylets. These stylets are used to insert the needles into the tissue. The catheter trajectory is reconstructed by pulling out the stylet from the catheter while the microcoils are tracked using a dedicated MR sequence. In comparison to this active MR tracking method, the accuracy of FBG-based sensing is higher

($1.5mm$ on average with the active MR tracking method vs. $0.8mm$ on average with FBG-based tracking). Also the update rate of the FBG-based needle tracking is higher and latency lower (around 10 seconds acquisition time per catheter with the MR tracking method vs $100ms$ update rate and $300ms$ latency with FBG-based sensing). Besides, De Oliviera *et al* (2008) proposed a needle tracking method using MR in the case of endorectal biopsy device. This tracking method has also a lower update rate and higher latency (the total duration of the tracking sequence is about 10 min).

Finally, although MRI presents a lot of advantage such as high contrasts of soft tissues which is useful for organs/tumor delineation, FBG-based needle tracking can also *a priori* be done under a different imaging modality such as ultrasound, computed tomography, or X-ray. In that scenario, other needle tracking methods (which are not MR-compatible) have been recently developed. Kaya *et al* (2015) proposed a method to determine automatically the tip of a needle using 2D ultrasound imaging: The needle tip is estimated with the Gabor filter-based image processing algorithm, and the estimation noise is reduced with the Kalman filter. In that study, the tip location was measured and compared with optical tracking system. The Euclidean distance of the tip position was found to be $1.17mm$. Additionally, a 3D electromagnetic needle tracking system was recently developed (Boutaleb *et al* 2015, Poulin *et al* 2015, Zhou *et al* 2013, Damato *et al* 2014): a stylet, composed of miniature sensor coils, is immersed in alternating magnetic fields. The resulting electric signal of the sensor coils is then converted to detect the position of the stylet (and therefore the needle when the stylet is inserted in the needle's lumen). The tracking accuracy experiments showed that positional errors were higher (typically $1mm$) compared with FBG-based needle tracking. In addition, the accuracy was dependent on disturbing equipment around.

The benefit of MRI was two-fold in the scope of our study: 1) it allowed determining the position and the orientation of the base ; 2) it provided a gold standard of the needle shape. This allowed reaching the following endpoints of our paper: 1) to demonstrate the potential of FBG-based needle tracking for the determination of the needle position with high frame rate and low latency ; 2) to demonstrate the potential of the latter under on-line MRI. Regarding the determination the position and the orientation of the stylet base, we proposed a simple protocol involving the fixation of the stylet base and the determination of its position and orientation using a MR-based calibration. In the proposed MR calibration, several (at least 2) needle shapes (see (1) in section 4.2.2) are used to determine the stylet position and orientation at the reference point. This way, the determination of the stylet's position and orientation at the reference point is more accurate: If only one needle shape is used for the registration, the determination of the orientation about the longitudinal axis of the stylet may not be accurate (especially if the needle shape is straight).

A limitation of the proposed tracking protocol arises from the fact that our system is now implemented with the stylet in a fixed support. Although this condition was fulfilled in our experiments, this may not be the case under clinical practice.

In a clinical workflow, to know the position and orientation of the stylet base, it should be mounted in a flexible and tracked support that is fixed to the table. This special support could be a robot that supports the insertion of the needle such as those currently developed in several institutes (Podder *et al* 2014). In particular, at our institution (the UMCU), a MR-compatible single needle robotic device which is fixed to the MR couch is currently under development (Van den Bosch *et al* 2010). Knowing the needle mounting position of the robot in the MR coordinate space means that we can determine the complete shape of the needle in the MR coordinate system. In our view, the current promising results provide justification to continue investing in further improvements of the clinical implementation of the FBG tracking technology within an MR-guided workflow.

Furthermore, the clinical benefits of such a system would be twofold. The first clinical benefit is for real-time tracking of needle during insertion. The fast and accurate feedback of the needle position will help the steering of the needle and warn the user in case of deviations from the planned needle track: better dose coverage and less toxicity would then be expected due to less needle positioning errors. The second clinical benefit is for fast and automatic reconstruction of the needle after insertion. The authors expect that with FBG tracking, less time will be spent compared to manual segmentation of a needle with possibly, a better accuracy. This would allow a shorter overall procedure time and enable update of the dose plan with feedback on the needle positioning error. Future works will involve pre-clinical and clinical evaluations of the setup.

4.5 Conclusion

The proposed FBG-based needle tracking method is able to determine the position of the whole needle with an accuracy of $0.79mm$, a precision (standard deviation) of $0.37mm$, an update rate of $100ms$ and a latency of $300ms$. The proposed approach is a good candidate for the measurement and the compensation of needle positioning errors during the procedure. This would allow an improved needle guidance and reconstruction. Moreover, the dose plan may be updated accordingly using a suited feedback strategy based on the residual needle deviations.

Appendix. Optimization strategy to perform the rigid registration of the MR and FBG-based needle position measurement

This section details the method employed to find the transformation between the FBG and the segmented MR-based measurement of a needle. 6 transformation parameters are determined: 3 parameters of translations, noted t_x, t_y and t_z, along X_{MR}, Y_{MR} and Z_{MR} (the axis of the MR image) and 3 angles of rotation, noted θ_x, θ_y and θ_z, about X_{MR}, Y_{MR} and Z_{MR}. A way to determine the value of t_x, t_y, t_z, θ_x, θ_y and θ_z is: first, to determine paired MR and FBG-based measurement points at regular intervals along the needle and then, to minimize

the distance between the paired MR and FBG-based measurements points after transformation.

4.A.1 Determination of the paired MR and FBG-based measurement points at regular intervals along the needle

It is noticeable that the FBG-based measurement gives the needle's shape at regularly sampled position (every $1mm$) along the stylet. Consequently, to determine the corresponding MR points, the MR based needle shape needs to be analytically modeled: A 3D parametric polynomial fitting of the MR-based points is chosen with the following general form:

$$\begin{cases} x(t) = a_n t^n + a_{n-1} t^{n-1} + \cdots + a_0 \\ y(t) = b_n t^n + b_{n-1} t^{n-1} + \cdots + b_0 \\ z(t) = t \end{cases} \tag{4.1}$$

The polynomial order n is optimized exhaustively by following two conditions: (1) the order must be as small as possible to avoid over-fitting, and (2) the maximum fitting error must be lower than the typical uncertainties of the manually segmented points (estimated at half the voxel size in the MR image).

With this model, the corresponding points of the MR-based measurement can easily be determined by sampling the model at same positions along the stylet compared to the FBG-based measurement points.

4.A.2 Determination of the transformations parameters

The next step is to determine the value of t_x, t_y, t_z, θ_x, θ_y and θ_z using a minimization of the distance between the MR and FBG-based paired points after transformation (rotations and translations). For this purpose, we employed a gradient driven optimization method.

Let n be the total number of paired points, and for all $i \in [1; n]$, $(x_i^{MR}, y_i^{MR}, z_i^{MR})$ and $(x_i^{FBG}, y_i^{FBG}, z_i^{FBG})$ are their corresponding coordinates of the MR and FBG-based measurement points. To minimize the distance between the paired points, the following cost function $C(t_x, t_y, t_z, \theta_x, \theta_y, \theta_z)$ (corresponding to the squared average distance between the paired points after transformation (rotations and translations)) is minimized:

$$\begin{aligned} &C(t_x, t_y, t_z, \theta_x, \theta_y, \theta_z) = \\ &\quad \| P^{MR} - A_{FBG \to MR}(t_x, t_y, t_z, \theta_x, \theta_y, \theta_z) P^{FBG} \|_2^2 \end{aligned} \tag{4.2}$$

where P^{MR} and P^{FBG} are the MR and FBG-based measurement points matrices:

$$P^{MR} = \begin{pmatrix} x_1^{MR} & \cdots & x_n^{MR} \\ y_1^{MR} & \cdots & y_n^{MR} \\ z_1^{MR} & \cdots & z_n^{MR} \\ 1 & \cdots & 1 \end{pmatrix}, \; P^{FBG} = \begin{pmatrix} x_1^{FBG} & \cdots & x_n^{FBG} \\ y_1^{FBG} & \cdots & y_n^{FBG} \\ z_1^{FBG} & \cdots & z_n^{FBG} \\ 1 & \cdots & 1 \end{pmatrix} \tag{4.3}$$

and $A_{FBG\to MR}(t_x, t_y, t_z, \theta_x, \theta_y, \theta_z)$ is the transformation matrix:

$$\begin{aligned} A_{FBG\to MR}(t_x, t_y, t_z, \theta_x, \theta_y, \theta_z) = \\ T_x(t_x)T_y(t_y)T_z(t_z)R_x(\theta_x)R_y(\theta_y)R_z(\theta_z) \end{aligned} \tag{4.4}$$

where $T_x(t_x)$, $T_y(t_y)$ and $T_z(t_z)$ are the matrices of translation along the X_{MR}, Y_{MR} and Z_{MR} axis and $R_x(\theta_x)$, $R_y(\theta_y)$ and $R_z(\theta_z)$ the matrices of rotation about the X_{MR}, Y_{MR} and Z_{MR} axis.

Since $A_{FBG\to MR}(t_x, t_y, t_z, \theta_x, \theta_y, \theta_z)$ is not linear along θ_x, θ_y and θ_z, the minimization of $C(t_x, t_y, t_z, \theta_x, \theta_y, \theta_z)$ is therefore performed using a gradient driven method.

CHAPTER 5

A novel adaptive needle insertion sequencing for robotic, single needle MR-guided high-dose-rate prostate brachytherapy

The following chapter is based on:
Borot de Battisti M, Denis de Senneville B, Hautvast G, Binnekamp D, Lagendijk J J W, Maenhout M and Moerland M A 2017 A novel adaptive needle insertion sequencing for robotic, single needle MR-guided high-dose-rate prostate brachytherapy *Phys. Med. Biol.* **62** 4031-45

Abstract

MR-guided HDR brachytherapy has gained increasing interest as a treatment for patients with localized prostate cancer because of the superior value of MRI for tumor and surrounding tissues localization. To enable needle insertion into the prostate with the patient in the MR bore, a single needle MR-compatible robotic system involving needle-by-needle dose delivery has been developed at our institution. Throughout the intervention, dose delivery may be impaired by: (1) sub-optimal needle positioning caused by e.g. needle bending, (2) intra-operative internal organ motion such as prostate rotations or swelling, or intra-procedural rectum or bladder filling. This may result in failure to reach clinical constraints. To assess the first aforementioned challenge, a recent study from our research group demonstrated that the deposited dose may be greatly improved by real-time adaptive planning with feedback on the actual needle positioning. However, the needle insertion sequence is left to the doctor and therefore, this may result in sub-optimal dose delivery. In this manuscript, a new method is proposed to determine and update automatically the needle insertion sequence. This strategy is based on the determination of the most sensitive needle track. The sensitivity of a needle track is defined as its impact on the dose distribution in case of sub-optimal positioning. A stochastic criterion is thus presented to determine each needle track sensitivity based on needle insertion simulations. To assess the proposed sequencing strategy, HDR prostate brachytherapy was simulated on 11 patients with varying number of needle insertions. Sub-optimal needle positioning was simulated at each insertion (modeled by typical random angulation errors). In 91% of the scenarios, the dose distribution improved when the needle was inserted into the most compared to the least sensitive needle track. The computation time for sequencing was less than 6s per needle track. The proposed needle insertion sequencing can therefore assist in delivering an optimal dose in HDR prostate brachytherapy.

5.1 Introduction

HDR prostate brachytherapy has gained increasing interest as an advanced treatment for patients with localized prostate cancer (Hauswald *et al* 2016, Morton and Hoskin 2013). It consists of inserting catheters into or close to the tumor and irradiating the localized cancer by stepping a radioactive source (e.g. Ir-192) through the catheters at various dwell positions for certain times according to a calculated dose plan (Venselaar *et al* 2012). In the current practice of HDR brachytherapy for localized prostate cancer, catheters are inserted manually under TRUS guidance in a parallel configuration with the support of a template brachytherapy grid (Hoskin *et al* 2013). After completion of the implant procedure, needle reconstruction, dose planning and needle position verification are assessed using TRUS, CT or MRI. This procedure is not optimal for several reasons: Firstly, US-guided

manual insertion of needles may lead to sub-optimal needle configurations due to (1) anatomical modifications such as prostate deformations and swelling, (2) the shadowing effect behind the implant needles which decreases the image quality. Secondly, the procedure can be relatively time consuming ($\sim$ few hours) if two imaging modalities are used (TRUS for insertion of the needle and CT or MRI for the needle reconstruction).

Imaging, pathology and dose delivery studies have shown the superior value of multi-parametric MRI for localization of prostate tumor (Atalar and Ménard 2005, Groenendaal *et al* 2010). Consequently, a complete MR-guided focal HDR prostate brachytherapy procedure is currently being investigated: To support needle insertion into the prostate with the patient in the MR bore, MR-compatible robotic methods have been developed recently in several institutes (Muntener *et al* 2006, Fischer *et al* 2007 and 2008 and DiMaio *et al* 2007). In particular, a single needle MR-compatible robotic device is being developed at the UMCU (Van den Bosch *et al* 2010). This robotic device allows the automatic transperineal insertion of the needle into the prostate under MR-guidance. With this setup, the needle is inserted without a template, under different angles in a divergent pattern from a single rotation point situated at the perineum. Moreover, the dose is delivered needle-by-needle. A fast optimization planning method was recently proposed for this setup (Borot de Battisti *et al*, 2015).

However, during the intervention, suboptimal dose delivery can occur due to two unpredictable events as follows:

1. **Sub-optimal needle positioning** can happen due to uncertainties of the robotic needle placement or bending of the needle: Straßmann et al (2011) showed, on a prostate model, that the average needle positioning accuracy was $2.7 \pm 0.7mm$ and $1.8 \pm 0.6mm$ in the two following scenarios: (1) when the needle is manually inserted by the doctor with support of a template and (2) when using a robot-assisted method, respectively.
2. **Intra-operative internal organ motion** such as swelling, displacement (Stone *et al* 2002) or rotation (Lagerburg *et al* 2005) of the prostate (related to the trauma caused by the needle insertion) or intra-procedural changes in rectum or bladder filling may also induce sub-optimal target coverage or overdose of organ at risk.

In practice, sub-optimal dose delivery cannot be measured directly: The dose deposition relies on model-based dose calculation methods (Beaulieu *et al* 2012) which requires, as input, tumor, OARs, needle and source localization. The ultimate goal is therefore to develop a fully automatic control system, where the dose plan and the needle insertion sequence are re-optimized during the intervention according to the two aforementioned perturbations. This fully automatic control system would require (1) to localize accurately the tumor and OARs which can be provided by the MRI (e.g. in current practice of HDR prostate brachytherapy at the UMCU, after insertion of catheters under TRUS guidance, the anatomy of

the patient is imaged and delineated using MRI for dose planning), (2) to localize accurately the needle with MRI or other MR compatible localization methods such as fiber Bragg gratings-based technology (Borot de Battisti 2016b), (3) to calculate and update the dose plan and (4) the needle insertion sequence during the procedure

To make a step towards this ultimate goal, a pipeline (cf. Figure 5.1a) was proposed by our group in a previous study (Borot de Battisti *et al* 2016a): This pipeline consists of calculating an initial dose plan and re-optimizing the dose plan during the intervention with feedback on sub-optimal needle positioning. This study showed that updating the dose plan, during the interventional procedure, may improve the delivered dose and allow to reach the clinical constraints. However, the needle insertion sequence is left to the doctor and may thus be potentially sub-optimal. A tool to assist the doctor in determining the optimal needle insertion sequence would therefore be of great interest. In order to develop a fully automatic control system with feedback on sub-optimal needle positioning and increase the chance of reaching the clinical constraints, the fast, automatic and adaptive determination of the optimal needle insertion sequence is therefore mandatory. In the scenario of TRUS-guided needle insertion with parallel needle configuration, the GEC/ESTRO working group (Hoskin *et al* 2013) recommends to start to implant with the anterior catheters. That way, issues related to the ultrasound shadowing effect behind the implant needles are reduced. Moreover, interference with the pubic arch can be checked at an early stage of the intervention so the setup can be adjusted to overcome this. However, those issues are not applicable for needle-by-needle delivery or MR-guided needle insertion.

In this manuscript, a new needle insertion sequencing strategy for MR-guided focal HDR brachytherapy involving needle-by-needle dose delivery is proposed (Figure 5.1b). The needle is inserted along the track which has the largest impact on the dose coverage if a sub-optimal needle positioning occurs. That way, potential sub-optimal needle positioning is compensated by the re-optimization of the subsequent needle insertions. The impact on the dose coverage (or also called the "sensitivity" later on in this manuscript) of each possible needle track is predicted by a stochastic method based on needle insertion simulations. The proposed needle sequencing strategy was assessed by simulating MR-guided HDR prostate brachytherapy on 11 patients with different sequences of needle insertions.

The main contribution of this study is therefore threefold:

1. A new adaptive needle insertion sequencing is introduced, based on the determination of the most sensitive needle track.
2. A new stochastic criterion to determine the sensitivity of each needle track is proposed, based on needle insertion simulations.
3. The performance of the proposed needle insertion sequencing is assessed by simulating MR-guided HDR prostate brachytherapy using MR-data of 11 patients diagnosed with prostate cancer.

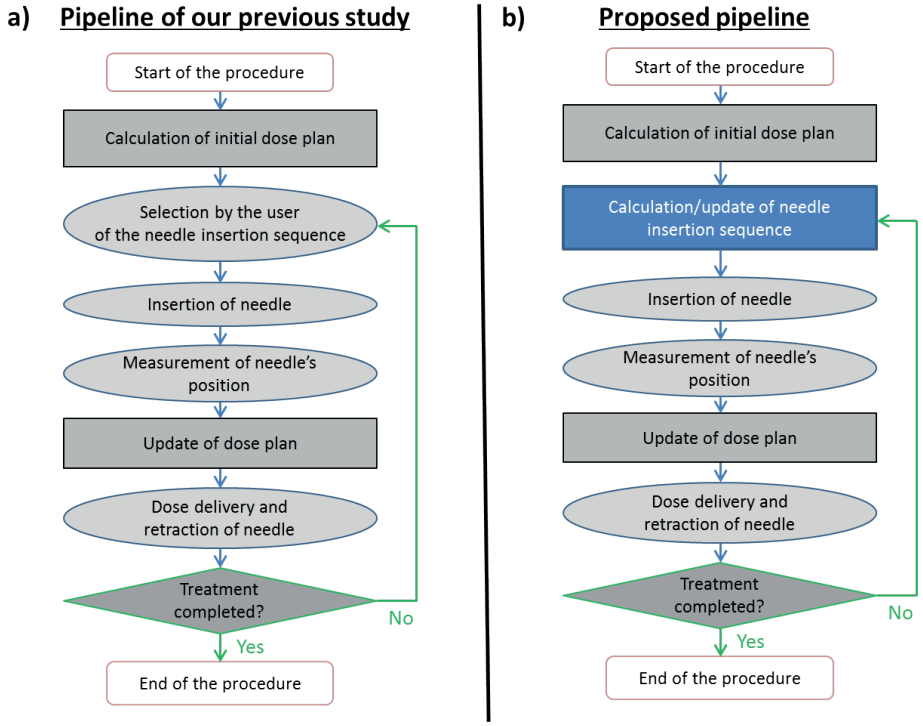

Figure 5.1: a) The schematic of the adaptive planning strategy proposed by our group in a previous study (Borot de Battisti *et al* 2016a): The determination of the needle insertion sequence is left to the doctor and may thus be potentially sub-optimal. b) The schematic of the new adaptive planning strategy: the needle insertion sequencing is determined automatically and adaptively based on the determination of the most sensitive needle track.

5.2 Methods

In this manuscript, a new adaptive and automatic needle insertion sequencing strategy is introduced. The method consists of inserting the needle into the most sensitive needle track: That way, sub-optimal needle positioning may still be compensated by the re-optimization of the subsequent needle insertions. For this purpose, a criterion designed to determine automatically the sensitivity of the needle tracks is presented in section 5.2.3. The adaptive needle sequencing is then assessed by simulating complete brachytherapy procedures on 11 patients with varying number of needle insertions (cf. section 5.2.4).

5.2.1 Clinical constraints

Focal prostate HDR brachytherapy aims to deliver an optimal dose distribution with a high irradiation dose to the tumor and the lowest possible dose to sur-

rounding OARs. At the UMCU, a dose plan is considered clinically acceptable when:

$$\begin{cases} D_{95\%\ PTV} > D^{min}_{95\%\ PTV} \\ D_{10\%\ Ur} < D^{max}_{10\%\ Ur} \\ D_{1cc\ Rec} < D^{max}_{1cc\ Rec} \\ D_{1cc\ Bl} < D^{max}_{1cc\ Bl} \end{cases} \tag{5.1}$$

where $D_{95\%\ PTV}$, $D_{10\%\ Ur}$, $D_{1cc\ Rec}$ and $D_{1cc\ Bl}$ are the doses received by 95% of the PTV, by 10% of the urethra and by $1cc$ of rectum and bladder, respectively. $D^{min}_{95\%\ PTV}$, $D^{max}_{10\%\ Ur}$, $D^{max}_{1cc\ Rec}$ and $D^{max}_{1cc\ Bl}$ correspond to the minimal accepted value of $D_{95\%\ PTV}$ and the maximal accepted value of $D_{10\%\ Ur}$, $D_{1cc\ Rec}$ and $D_{1cc\ Bl}$ in order to obtain a clinically acceptable and optimal dose plan. Their values are equal to 19Gy, 21Gy, 12Gy and 12Gy, respectively. Those constraints are in line with the study of Hoskin *et al* (2014) and Prada *et al* (2012) who showed that HDR brachytherapy as monotherapy is feasible with acceptable levels of acute complications by delivering a single fraction dose of $19Gy$ to the target.

5.2.2 Assessment of the quality of the dose plan

To determine automatically the sensitivity of each needle track, the quality of a dose plan must be assessed. An evaluation parameter is therefore mandatory to compare the quality of different dose plans. In the scope of this study, we used the evaluation parameter E introduced by Borot de Battisti *et al* (2015) called the "energy parameter" and is such that the greater E is, the better quality the dose plan becomes. E is expressed as the minimum of the four parameters, A, B, C and D where:

$$\begin{cases} A = D_{95\%\ PTV} - D^{min}_{95\%\ PTV} \\ B = D^{max}_{10\%\ Ur} - D_{10\%\ Ur} \\ C = D^{max}_{1cc\ Rec} - D_{1cc\ Rec} \\ D = D^{max}_{1cc\ Bl} - D_{1cc\ Bl} \end{cases} \tag{5.2}$$

The parameters A, B, C and D represent the differences between the dose coverage parameters and the clinical constraints of the PTV, the urethra, the rectum and the bladder, respectively. E represents therefore the smallest difference in Gray between each dose parameter and the clinical constraints. Theoretically, E can take any value between $-\infty$ and ∞. Moreover, if $E > 0$, all dose parameters achieved the clinical constraints. Conversely, if $E \leq 0$, at least one dose parameter did not achieve the clinical constraints.

It is important to note that the use of this particular evaluation parameter is not mandatory to perform the needle insertion sequencing proposed in this manuscript: the needle insertion sequencing strategy is also compatible with the use of any other evaluation parameter expression which assesses the dose plan quality.

5.2.3 New criterion to determine the sensitivity of each needle track

In this section, a criterion is proposed to predict automatically the sensitivity of each possible needle insertion track. The needle track sensitivity is determined using a stochastic method based on needle insertion simulations. For a given needle track i ($i \in [1, N_{tracks}]$, N_{tracks} is the number of possible needle insertion tracks), the algorithm assessing the needle track sensitivity is described as follows:

Step 1: Starting from the current dose plan, N_{angle} needle insertions are simulated by randomly modifying the needle track angulation (the dwell times and positions along the needle remain unchanged). N_{angle} is an integer large enough to be statistically acceptable. The random angulation is modeled by a Gaussian distribution with a standard deviation of $0.015rad$: this corresponds to a typical insertion error of $3mm$ at a distance of $200mm$ from the center of rotation. After investigation, a typical value of $N_{angle} = 100$ was found to be a good compromise between speed and statistical significance.

Step 2: The N_{angle} newly created dose plans are then evaluated by calculating the energy parameter E (defined in section 5.2.2) for each dose plan.

Step 3: The 5th percentiles of the determined E-values (noted $E_{5\%}(i)$) are calculated. $E_{5\%}(i)$ corresponds to the worst impact on the dose that a sub-optimal needle positioning in needle track i may induce. $E_{5\%}(i)$ is therefore related to the sensitivity of needle track i: the higher $E_{5\%}(i)$ is, the less sensitive the needle track becomes. The 5th percentiles are preferred rather than the minimum in order to avoid outliers.

With this method, we can predict the most and least sensitive needle track $i_{least\ sens}$ and $i_{most\ sens}$ which are expressed as follows:

$$i_{least\ sens} = \underset{i \in [1; N_{tracks}]}{\operatorname{argmax}} \left[E_{5\%}(i)\right] \tag{5.3}$$

$$i_{most\ sens} = \underset{i \in [1; N_{tracks}]}{\operatorname{argmin}} \left[E_{5\%}(i)\right] \tag{5.4}$$

The optimal needle sequence corresponds thus to inserting the needle into the needle track $i_{most\ sens}$ of the current dose plan. Conversely, the least optimal sequence corresponds to inserting the needle into the needle track $i_{least\ sens}$ of the current dose plan.

5.2.4 Experimental evaluation: Simulation of HDR prostate brachytherapy to assess the proposed adaptive needle sequencing

In this section, the experiment to assess the proposed adaptive needle insertion sequencing is described. Focal HDR prostate brachytherapy procedures were simulated on 11 patients with different number of needle insertions (4, 6, 8, 10 and 12).

The simulated brachytherapy procedures followed the strategy described in Figure 5.1b. Sub-optimal needle positioning was simulated for each needle insertion (see section 5.2.4.3). Two situations were compared:

1. When the least sensitive needle track was selected for insertion: That corresponds to the " least optimal" needle insertion sequence.
2. When the most sensitive needle track was selected for insertion: That corresponds to the "optimal" needle insertion sequence.

All brachytherapy simulations were repeated 100 times to assess the robustness of the two tested needle sequences. For each scenario, the final dose parameters $D_{95\%\ PTV}$, $D_{10\%\ Ur}$, $D_{1cc\ Rec}$ and $D_{1cc\ Bl}$ and the final energy parameter E (assessing the quality of the dose distribution) were calculated.

The details of the simulations are presented as follows.

5.2.4.1 Dose planning algorithm

The calculation of the initial dose plan and the re-optimization of the dose plan were performed using the algorithm described by Borot de Battisti *et al* (2015) and Borot de Battisti *et al* (2016a), respectively: the algorithm involves an exhaustive search of the center of rotation of the setup, a heuristic optimization of the needle track angulations and the determination of the dwell times by solving linear equations.

5.2.4.2 Anatomy

Between May 2013 and April 2016, 30 patients were treated by focal MR-guided focal HDR prostate brachytherapy as monotherapy at the UMCU according to the current practice: catheters were first inserted manually under TRUS-guidance with the support of a template grid, and needle reconstruction and dose planning were then assessed using MRI. These patients had localized prostate cancer with a prostate-specific antigen (PSA) level lower than $10\,\mathrm{ng\,ml^{-1}}$ and a Gleason score of 7 or less. The intra-operative MR-data – taken directly after the needles were in place – of the first 15 consecutive patients were included in the simulation study. The anatomy of the patients was obtained using the delineations of the prostate tumors and the OAR considered (urethra, bladder and rectum) on $1mm^3$ resolution MR images by an experienced oncologist. 4 patients were left out of the study because the initial simulated dose plan did not reach the clinical constraints. Consequently, the brachytherapy procedures were simulated using MR-data of 11 patients. The PTV ranged from $9.5cm^3$ to $31.3cm^3$ with a median of $22.8cm^3$. The acquisition of patient MR images used in this study was approved by the Institutional Review Board (IRB). It is noticeable that Patient 9, 10 and 11 were considered as more "difficult cases" for dose planning compared to the other patients because the PTV was very close (if not touching) an OAR (*cf.* Figure 5.2): Patient 9 and 10 had the PTV wound around the urethra and for Patient 11,

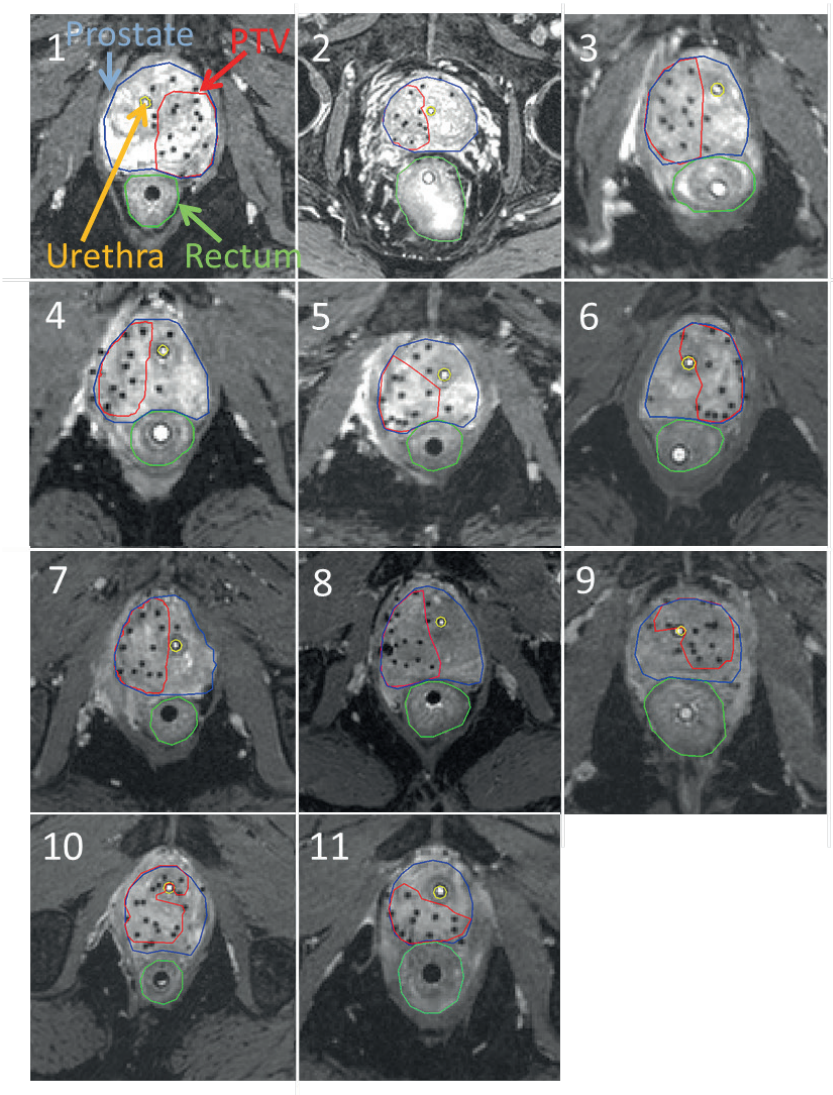

Figure 5.2: Transversal MR images with the delineations of the volumes of interest (PTV, urethra, prostate and rectum) of 11 patients of the study. The number reported in the upper-left of each image corresponds to the number associated to the patient throughout the manuscript. For instance, Patient 2 corresponds to an "easy case" and Patient 9 a "difficult case" for dose planning.

the PTV was very close to the rectum. Consequently, the arrangement of needle tracks was limited for those patients in order to avoid the needle going through an OAR.

To clarify the benefits of the proposed needle sequencing strategy on the overall results, the anatomy of the patient (delineated before the initial dose plan) was supposed to remain constant throughout the procedure in order to exclude possible artifacts and uncertainties of image registration or dose accumulations.

5.2.4.3 Sub-optimal needle positioning

Sub-optimal needle positioning was modeled as follows: each needle insertion had a random angulation error described by a Gaussian distribution with a standard deviation of $0.015rad$ (*i.e.* $3mm$ at the tip of the needle). The value of the standard deviation was chosen in line with the study of Strassman et al (2011) who assessed the accuracy of needle positioning on a prostate model: in the worst case of the two tested scenarios (manual and robotic needle insertion), the average needle positioning accuracy was $2.7 \pm 0.7mm$. Additionally, we assumed that, during the brachytherapy intervention, the needle position could be measured without error.

5.2.4.4 Model of dose calculation

To simulate the distributed dose to the patient, the point source approximation model was chosen to calculate the dose rate of the source because of its minimum time of computation, with a small adaptation as follows to avoid over-optimization of the dose close to the source:

$$d_i(\boldsymbol{r}) = S_K \Lambda g_P[R_i(\boldsymbol{r})] \Phi_{an}[R_i(\boldsymbol{r})] \frac{{R_0}^2}{R_i(\boldsymbol{r})^2 + \exp[-R_i(\boldsymbol{r})^2]} \tag{5.5}$$

where $d_i(\boldsymbol{r})$ is the dose rate of the i^{th} source position at $\boldsymbol{r}$, S_K is the air-kerma strength, Λ the dose-rate constant in water, $\Phi_{an}(R)$ the one-dimensional anisotropy factor, R_0 the reference distance which is specified to be $10mm$, $g_P(R)$ the radial dose function in the case of the point source approximation model and $R_i(\boldsymbol{r})$ the distance (in millimeters) between the i^{th} source position at coordinate $\boldsymbol{r}_i$ and $\boldsymbol{r}$ ($R_i(\boldsymbol{r}) = ||\boldsymbol{r}_i - \boldsymbol{r}||_2$). With this adaptation of the point source model, the dose has an upper limit value close to the source, therefore it reduces the numeric instabilities for $R_i(\boldsymbol{r})$ approaching 0. TG43 constants, anisotropy factor and radial dose function for the microSelectron-HDR (Elekta/Nucletron, Veenendaal, The Netherlands) 192-Iridium source were taken from a study of Daskalov *et al* (1998) ($\Lambda = 1.108cGy.h^{-1}.U^{-1}$) and an arbitrary source strength $S_K = 40.80mGy.h^{-}1.m^2$ was chosen. The multiplication of the radial dose function $g_P(R)$ and the anisotropy factor $\Phi_{an}(R)$ was approximated by a 2^{nd} order polynomial fit ($g_P(R) \cdot \Phi_{an}(R) = a_0 + a_1 R + a_2 R^2$). The coefficients for the fit were $a_0 = 1.11$, $a_1 = -3.30 \cdot 10^{-3}$ and $a_2 = 3.12 \cdot 10^{-6}$, where R is in millimeters.

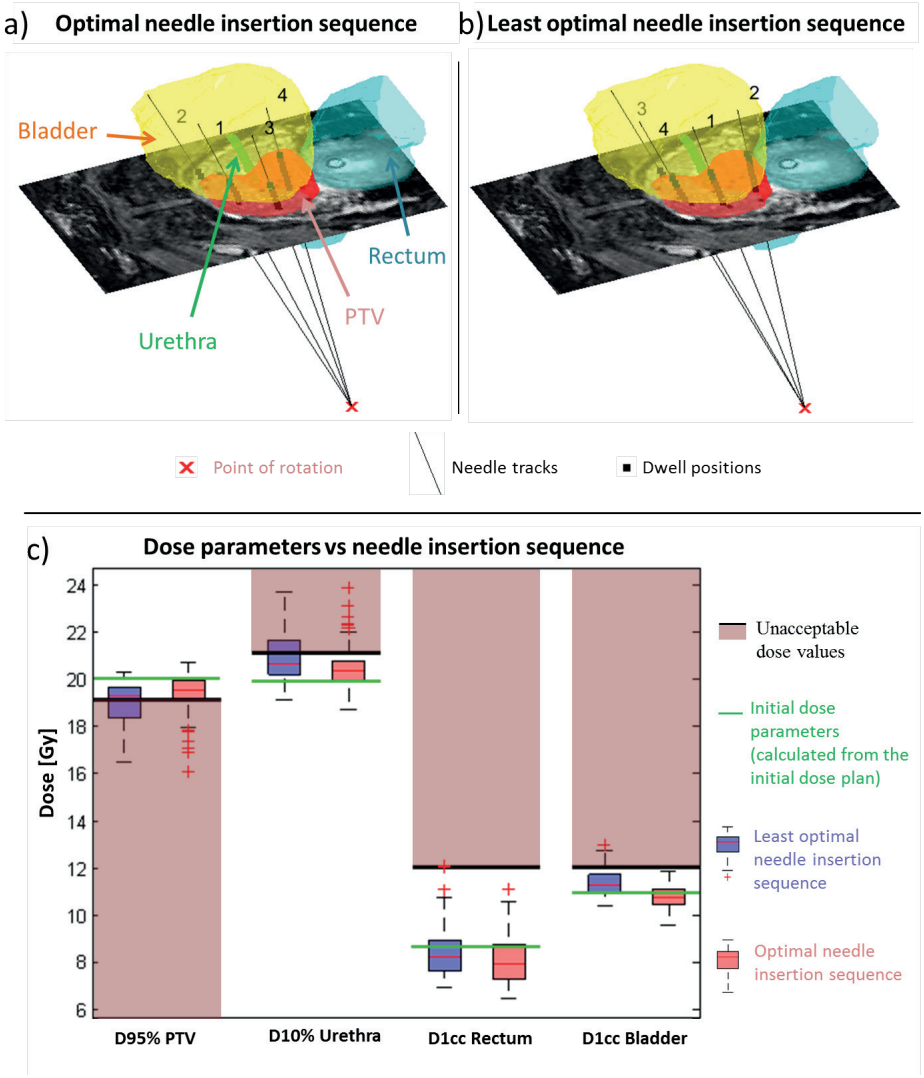

Figure 5.3: Results obtained for a typical patient (Patient 2 with 4 needle insertions in the simulation study). a) and b) Final needle trajectories and dwell positions together with the anatomy resulting from 1 simulation in the situation of optimal and least optimal needle insertion sequence respectively. The order of needle insertion is depicted at the tip of the needle. c) Final dose parameters resulting from the 100 simulations in the situation of optimal and least optimal needle insertion sequence. The green and black lines represent the preplan dose parameters and the clinical constraints, respectively.

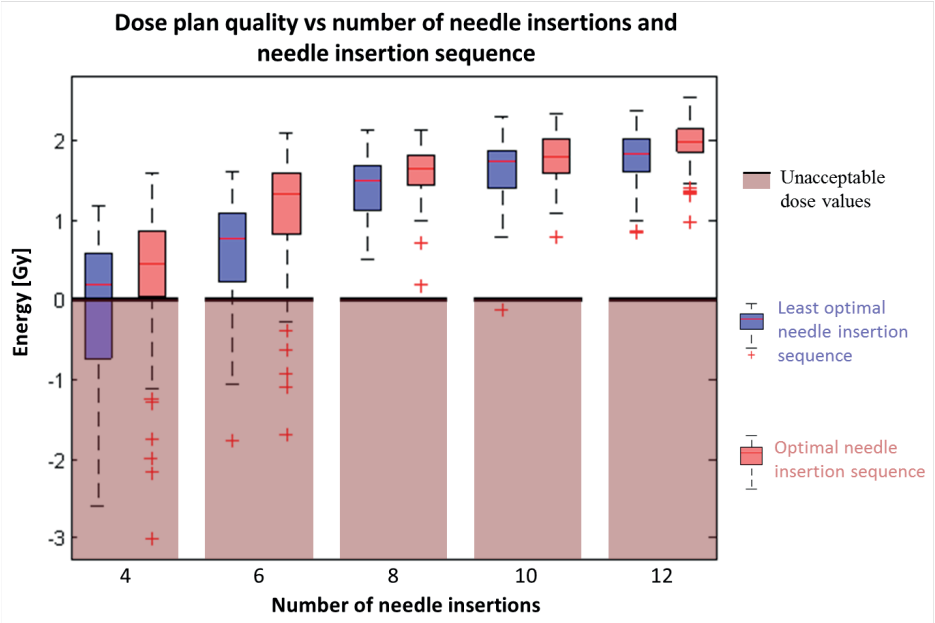

Figure 5.4: Dose plan quality as a function of the number of needle insertions and the needle insertion sequence for Patient 2.

5.3 Results

The results of the brachytherapy simulations corresponding to Patient 2 with 4 needle insertions are depicted in Figure 5.3. Figure 5.3a and b represent the final needle trajectory locations and the order of needle insertions resulting from 1 simulation in the situation of optimal and least optimal needle insertion sequence respectively. Figure 5.3c presents the final dose parameters resulting from the 100 simulations: The final dose parameters [$D_{95\%\ PTV}$, $D_{10\%\ Ur}$, $D_{1cc\ Rec}$, $D_{1cc\ Bl}$] in the situation without sub-optimal needle positioning (calculated from the initial dose plan) were [20.0Gy, 19.8Gy, 8.6Gy, 10.9Gy]. With sub-optimal needle positioning, the median(minimum,maximum) of the final dose parameters was [19.2(16.4, 20.2)Gy, 20.5(19.0, 23.6)Gy, 8.2(6.9, 12.0)Gy, 11.2(10.4, 12.9)Gy] for the least optimal needle sequencing scenario. Using the proposed optimal needle sequencing, these values were equal to [19.4(16.0, 20.6)Gy, 20.3(18.6, 23.7)Gy, 7.9(6.5, 11.0)Gy, 10.7(9.5, 11.8)Gy].

The final energy parameters corresponding to Patient 2 with 4, 6, 8, 10 and 12 needle insertions are presented in Figure 5.4 in the situation of optimal and least optimal needle insertion sequence. For [4, 6, 8, 10, 12] needle insertions, the median(minimum, maximum) of the energy parameter was [0.2(−2.6, 1.2), 0.8(−1.8, 1.6), 1.5(0.5, 2.1), 1.7(−0.1, 2.3), 1.8(0.8, 2.4)] in the situation of least optimal sequencing and [0.4(−3.0, 1.6)Gy, 1.3(−1.7, 2.0)Gy, 1.6(0.2, 2.1)Gy, 1.8(0.8,

$2.3)Gy$, $2.0(1.0, 2.5)Gy]$ in the situation of optimal sequencing.

Table 5.1 presents the percentage of final dose distributions which fulfilled all clinical constraints (*i.e.* $E \geq 0$) for the two tested needle sequencing protocols. According to the table, the percentage of clinical acceptable final dose distributions was equal or higher for 50 scenarios tested with the optimal needle sequence compared to the least optimal needle sequence and lower for 5 scenarios (Patient 5 with 4 needle insertions, Patient 8 with 8 needle insertions, Patient 9 with 6 needle insertions, and Patient 11 with 8 and 10 needle insertions). This corresponds to a dose improvement in 91% of the scenarios tested. It is noticeable that the percentage of clinically acceptable dose plans was low for Patient 9, 10 and 11 (considered as the "difficult cases") compared to other patients in both situations of least optimal and optimal needle sequencing.

5.4 Discussion

In this study, a new automatic and adaptive needle sequencing strategy was proposed for MR-guided HDR prostate brachytherapy. This sequencing is based on the determination of the most sensitive needle track. For that, a new criterion was introduced to predict and quantify the sensitivity of each possible needle insertion track.

The simulation study showed that inserting the needle into the most sensitive needle track will statistically lead to an improved dose coverage compared to inserting into the least sensitive track. Most specifically, the final dose parameters presented in Figure 5.3 illustrate this trend: when the needle insertion sequence was optimal (*i.e.* the needle is inserted into the most sensitive needle track), the dose tended to increase at the PTV and to decrease at the OARs in comparison to the situation of least optimal needle insertion sequence (*i.e.* the needle is inserted into the least sensitive needle track). Inserting the needle into the most sensitive needle track allows sub-optimal needle positioning to be compensated by the re-optimization of the subsequent needle insertions. Moreover, for some patients, the difference in the dose coverage was more pronounced for small number of needle insertions (*cf.* Figure 5.4). This could be explained by the fact that the dose delivered by each needle decreases with the number of needle insertions: For a small number of needle insertions, the dose delivered by each needle is high and there are few needles to compensate for sub-optimal positioning. Therefore, the robustness of the dose plan to sub-optimal needle positioning decreases when a small number of insertions is used. Consequently, the difference of impact on the distributed dose due to sub-optimal needle positioning between least optimal and optimal needle sequence situation is more important with a small number of needle insertions. This effect is attenuated for a large number of needle insertions. In this study, there was no clear correlation between the percentage of clinically acceptable dose plans and the prostate volume. Although a large prostate (or PTV) may be more difficult to cover compared to a small one, the accessibility of the target by the needle (which may be impaired by the urethra or the pubic bone), or the localization of the PTV with respect to the OARs may also play

Table 5.1: Percentage of clinically acceptable dose plans obtained for 11 patients with $N_{needle} = 4$, 6, 8, 10 and 12 in the situation of (1) least optimal and (2) optimal needle sequencing (depicted as "(1) - (2)" in the table). Prostate and PTV volumes are presented in bottom lines.

Number of needle insertions	Clinically acceptable plan (%)										
	Pat. 1	Pat. 2	Pat. 3	Pat. 4	Pat. 5	Pat. 6	Pat. 7	Pat. 8	Pat. 9	Pat. 10	Pat. 11
4	96 - 98	60 - 79	82 - 89	83 - 90	22 - 11	0 - 6	95 - 100	82 - 87	0 - 0	0 - 2	0 - 0
6	100 - 100	79 - 93	96 - 100	90 - 99	74 - 77	45 - 44	100 - 100	86 - 91	8 - 2	2 - 5	0 - 0
8	100 - 100	100 - 100	97 - 100	98 - 99	80 - 84	47 - 49	100 - 100	98 - 96	3 - 11	20 - 25	1 - 0
10	100 - 100	99 - 100	100 - 100	99 - 100	97 - 100	88 - 94	100 - 100	98 - 98	13 - 23	29 - 42	4 - 2
12	100 - 100	100 - 100	100 - 100	98 - 100	98 - 100	86 - 98	100 - 100	99 - 99	15 - 16	77 - 83	9 - 24
Prostate (mL)	102.5	84.7	54.2	65.8	68.5	50.2	85	76.5	43.4	65.9	50.8
PTV (mL)	26.0	22.8	25.2	24.3	22.8	20.7	30.7	31.3	13.1	9.5	12.6

a crucial role to obtain a clinical acceptable dose plan. Another important point concerns Patient 9, 10 and 11: for those patients, the percentage of clinically acceptable dose plans was lower compared to the other patients (*cf.* Table 5.1). For those patients, the PTV was very close to an OAR. Because of this, (1) the arrangement of needle tracks was limited and (2) the dose coverage of the PTV was restricted by the neighboring OAR. Therefore, those patients had less chance to receive a clinically acceptable dose. Finally, the brachytherapy simulations were implemented in MatLab 2015: the computation time increased linearly with the number of needle tracks involved in the sequencing process, and was less than 6 seconds per needle track.

In the presented study, an open number of needle insertions was chosen. In practice, a compromise has to be found: It is clear that the more needle insertions there are, the better the dose distribution will be. However, the influence of adding one or more needle insertions may lead to additional toxicity: Vargas *et al* (2005) and Boyea *et al* (2007) showed the urinary toxicity following HDR brachytherapy is significantly increased by using more than 14 needle insertions. For those reasons, we believe that an automatic determination of the number of needle insertions requires additional work and we decided to perform the simulations for different number of needle insertions. A range of 4 to 12 needle insertions was chosen because, in this range, clinically acceptable dose plans in most patient cases were obtained. It is also noticeable that Patient 11 is a difficult case because the percentage clinically acceptable dose plans obtained was less compared to the other patients. The implication for this patient may be to increase the number of needle insertions until the clinical constraints are reached.

The limitations of this study are mostly related to the limitations in the proposed brachytherapy simulation. Firstly, the point source approximation employed in this study (*cf.* Eq. 5.5) was chosen for implementation simplicity as well as computational speed considerations. However, the proposed needle sequence determination allows more precise source models such as line source approximation. Moreover, the anatomy was supposed to remain constant throughout the procedure in order to exclude possible artifacts and uncertainties of image registration or dose accumulations. In practice, the intra-operative internal organ motion due to, for example, swelling, displacement (Stone *et al* 2002) or rotation (Lagerburg *et al* 2005) of the prostate (related to the trauma caused by the needle insertion) or intra-procedural changes in rectum or bladder filling can cause uncertainties in the delivered dose during the intervention. Those issues can be solved by performing an adaptation of the dose plan and needle insertion sequence with feedback on the anatomy changes (in addition to feedback on sub-optimal needle positioning). The dose plan and needle sequencing adaptation with feedback on anatomy movements is possible while performing brachytherapy treatment under MRI-guidance (but also US-, CT-guidance) for which the anatomy can be captured during the interventional procedure. Finally, the MR data used for the simulation study were taken after insertion of the catheters. Since, one of the factors that affect needle insertion is prostate swelling, an interesting investigation can be to compare the magnitude of dose difference if the simulations are performed on images before vs

after implant. This will be investigated in future works.

The error associated with the measurement of the needle position should also lead to uncertainties on the delivered dose. This issue may be tackled by determining with a high accuracy and update rate the needle position in order to: (1) track the needle during insertion and consequently help the steering and the placement of the needle in the correct position, (2) reconstruct the needle after insertion to re-optimize the dose plan with feedback on sub-optimal needle positioning. To insure the fast and accurate measurement of the needle position, we believe FBG-based needle tracking described by Borot de Battisti *et al* (2016b) may be a great candidate. FBG-based needle tracking involves a stylet that can be inserted into brachytherapy needles to measure quickly and accurately the needle shape. The error propagation due to FBG-based tracking, adaptive dose planning and needle sequencing combination will be studied in future work.

The proposed needle sequencing is compatible with the experimental setup developed at the UMCU for MR-guided HDR prostate brachytherapy:

- in terms of hardware: the robotic device is designed to support needle insertion under MR-guidance
- in terms of software: the computation time of the needle insertion sequencing strategy is eligible for intra-operative use

Furthermore, the proposed needle sequencing may also be used (to some extent) for other applications with different setup as follows:

- using parallel and divergent needle patterns
- with or without brachytherapy template
- involving needle-by-needle delivery or delivery after all needles are in place
- with different imaging modalities such as CT, TRUS or MRI

since the stochastic approach only relies on the knowledge of the PTV and OARs localization.

5.5 Conclusion

In the presented study a new automatic and adaptive needle insertion sequencing was proposed for focal MR-guided HDR prostate brachytherapy involving needle-by-needle dose delivery. The approach consists of inserting the needle into the most sensitive needle track. To predict the sensitivity of each possible needle track, a stochastic criterion was proposed based on needle insertion simulations. To assess this needle sequencing strategy, HDR prostate brachytherapy was simulated on 11

patients with varying number of needle insertions (from 4 to 12). An improvement in the distributed dose was observed in 91% of the tested scenarios for which the needle was inserted into the most sensitive compared to the least sensitive needle track. Finally, the computation time for sequencing was less than 6 seconds per needle track (implementation on MatLab 2015). This novel adaptive sequencing tool can therefore assist the doctor during the intervention. Furthermore, it is a step towards the development of a fully automatic control system with feedback on unpredictable events occurring during brachytherapy, such as sub-optimal needle positioning and/or intra-operative internal organ motion.

CHAPTER 6

A new methodology for planning adaptation on anatomy deformation during MR-guided HDR prostate brachytherapy

The following chapter is based on:
Borot de Battisti M, Denis de Senneville B, Lagendijk, J J W, Hautvast G and Moerland M A 2017 A new methodology for planning adaptation on anatomy deformation during MR-guided HDR prostate brachytherapy *manuscript submitted to Phys. Med. Biol.*

Abstract

An hybrid platform which combines MRI and HDR prostate brachytherapy devices may change drastically the interventional paradigm in brachytherapy since it will enable real-time anatomy visualization during treatment. To this end, a single needle MR-compatible robotic device which supports needle insertion under MR guidance, is currently under development at the UMCU: this robot inserts transperineally the needle into the prostate in a divergent pattern due to the narrow MR-bore. That way, the dose is delivered needle-per-needle. To take advantage of the MRI compound of the system, we propose in this study a new strategy consisting in the intrafraction update of the dose plan and needle insertion sequence during treatment, with MR-based feedback on the anatomy deformations.

The performance of the system is evaluated through simulations, on 15 patients, with varying number of needle insertions (from 2 to 14), with and without intrafraction replanning. To mimic organ displacements during the intervention, two motion models were tested: needle insertion and retraction induced (1) a translation and (2) a rotation of the prostate, resulting in an incremental shift of the target and OARs during treatment. In both scenarios, with our proposed replanning strategy, a higher PTV dose was delivered safely to the patient compared the situation without replanning: with replanning, a clinically acceptable dose was delivered on average with 6 needle insertions or more. Furthermore, the average difference between initial dose parameters (calculated at the beginning of the treatment) and final dose parameters was within 6.0%. However, without replanning, $D_{95\%\ PTV}$ decreased 17.5% and $D_{10\%\ Ur}$ increased 16.4% with the translation and rotation motion model, respectively.

The development of our MRI-brachytherapy hybrid system is therefore promising for taking into account anatomy deformation during HDR prostate brachytherapy and to deliver a clinically acceptable dose plan.

6.1 Introduction

During the course of HDR prostate brachytherapy, two main events may occur, leading in turn to sub-optimal dose delivery. The first event is needle positioning errors which can be due to e.g. inaccuracy of needle insertion, and/or needle bending: Straßmann *et al* (2011) showed, on a prostate model, that the average needle positioning accuracy was $2.7 \pm 0.7mm$ when the needle is manually inserted by the doctor with support of a template, and $1.8 \pm 0.6mm$ when using a robot-assisted method. The second event is intra-operative internal organ motion such as swelling, displacement (Stone *et al* 2002, Lagerburg *et al* 2006) and rotation of prostate (Lagerburg *et al* 2005) induced by the needle insertion or retraction, or intra-procedural changes in rectum or bladder filling.

The UMCU is currently developing a novel hybrid system which combines MRI and a brachytherapy set-up for real-time anatomy and needle visualization during HDR prostate brachytherapy. This hybrid system may change drastically the interventional paradigm in brachytherapy since it allows needle guidance and monitoring of the changing patient anatomy during treatment (the target and OARs anatomy deformations that occur will be available through image registration algorithms). To enable HDR prostate brachytherapy treatment under MR-guidance, the UMCU is building a new single needle MR-compatible robot which supports the needle insertion in the narrow MR-bore (Van den Bosch *et al* 2010): Placed between the legs of the patient, the robot taps the needle transperineally under MR-guidance into the prostate. Moreover, due to limited space in the MR-bore, the needle is inserted in a divergent configuration (i.e. under different angles with a point of rotation situated at the perineum). That way, the dose is delivered needle-per-needle. Since then, the development of such hybrid systems gains a growing interest, and several designs along the same line are currently under investigation in other institutions (Podder *et al* 2014, Popescu *et al* 2015): Muntener *et al* (2006) developed a robot designed to place seeds under MRI-guidance for LDR brachytherapy intervention ; DiMaio *et al* (2007) and Fischer *et al* (2007, 2008) have designed MR-compatible robotic assistants for transperineal prostate needle placement.

In our previous work (Borot de Battisti *et al* 2015, 2016a and 2017), a new method for optimization of the dose plan and needle insertion sequence was developed, specifically suited for MRI-brachytherapy system such as the one developed at the UMCU. The method features intrafraction replanning based on the needle positioning errors. A MRI is acquired at the beginning of the treatment to localize the target and OARs, and an initial dose plan and sequence is determined. Then, after each insertion, a measurement of the needle position is performed (using MRI or other MR-compatible localization methods such as fiber Bragg gratings-based technology (Borot de Battisti *et al* 2016b)), and the dose plan and sequence are updated according to the deviation of the needle with respect to the planned trajectory.

However, none of the above mentioned strategies takes into account anatomy deformations, which are nevertheless likely to occur during the treatment (the position of the target and OARs is evaluated from a MRI image acquired at the beginning of the treatment). In the presented manuscript, we harness for the first time the MRI-brachytherapy hybrid compound of the system, with the aim of adapting the treatment during the intervention: a new strategy is proposed for intrafraction update of the dose plan and sequence, based on incoming anatomy deformations from MRI. The proposed strategy is evaluated by verifying if, given a set of anatomy deformations during treatment, the prescribed dose can be delivered to the target while minimizing the dose to the surrounding structures.

The contribution of this study is three-fold:

- To propose a new strategy consisting in the intrafraction update of the dose

plan and sequence during HDR prostate brachytherapy, with MR-based feedback on the anatomy deformation.

- To present a framework which aims to simulate intra-procedural movements occurring during HDR prostate brachytherapy using a single needle robotic device.

- To assess the performance of a MRI-brachytherapy hybrid system. For this purpose, HDR prostate brachytherapy treatments were simulated with varying number of needle insertions (from 2 to 14) using the MR-data of 15 patients. Two types of intra-operative internal organ motion were tested: an artificial (1) translation and (2) rotation of the prostate induced by the insertion and retraction of the needle was created, resulting in an incremental shift of the target during the treatment. We compared our adaptive strategy to the "static" strategy (without update of dose plan and sequence during treatment) by evaluating the final dose parameters.

6.2 Methods

We first recall clinical constraints in use at the UMCU in section 6.2.1. Then, we present in section 6.2.2 the new strategy which consists in updating the dose plan and needle insertion sequence during HDR prostate brachytherapy with MR-based feedback on the anatomy deformation. A framework is presented in section 6.2.3 for simulating anatomy movements during a brachytherapy procedure. Finally, we assess in section 6.2.4, the performance of a MRI-brachytherapy hybrid system by simulating MR-guided HDR prostate brachytherapy with and without intrafraction replanning.

6.2.1 Clinical constraints

The aim of focal prostate HDR brachytherapy is to deliver an optimal dose distribution with a high irradiation dose to the tumor and the lowest possible dose to surrounding OARs. At the UMCU, a dose plan is considered clinically acceptable when:

$$\begin{cases} D_{95\%\ PTV} > 19Gy \\ D_{10\%\ Ur} < 21Gy \\ D_{1cc\ Rec} < 12Gy \\ D_{1cc\ Bl} < 12Gy \end{cases}$$

where $D_{95\%\ PTV}$, $D_{10\%\ Ur}$, $D_{1cc\ Rec}$ and $D_{1cc\ Bl}$ are the doses received by 95% of the PTV, by 10% of the urethra and by $1cc$ of rectum and bladder, respectively. Those constraints are in line with the study of Hoskin *et al* (2014) and Prada *et al* (2012) who showed that HDR brachytherapy as monotherapy is feasible with acceptable levels of acute complications by delivering a single fraction dose of $19Gy$ to the target.

6.2.2 Proposed planning adapation strategy on anatomy deformation

6.2.2.1 Pipeline

During HDR prostate brachytherapy, the anatomy can move due to e.g. insertion or retraction of needles. In this manuscript, a pipeline is proposed consisting in updating, during treatment, the dose plan (i.e. the needle track positions, source positions and dwell times) and the needle insertion sequence with MR-based feedback on the anatomy deformation. This pipeline requires to monitor the anatomy deformation and adapt the distributed dose during the treatment.

The proposed pipeline is described in figure 6.1. It is composed of the following steps:

- **Task 1**. A MR image of the patient anatomy is performed and delineated. The initial dose plan and needle insertion sequence is then determined for given number of needle insertion N_{needle}.

- **Task 2**. The needle is inserted according to the dose plan and the needle insertion sequence.

- **Task 3**. The insertion of the needle may induce anatomy deformation (prostate rotation, translation, deformations,...) and the current dose plan and needle insertion sequence may be not optimal anymore. A 3D MR image of the anatomy is thus performed (Task 3a). The delineations and the actual accumulated dose are warped on the new anatomy grid (Task 3b) by registration between the new MRI to the previous MRI. The dose plan and needle insertion sequence are then updated with feedback on the anatomy changes using, as input, the warped delineations and accumulated dose (Task 3c).

- **Task 4**. The source is inserted into the needle and the dose is delivered according to the updated dose plan. The accumulated dose is stored in memory. Then the needle is retracted.

- **Task 5**. At this point, there are two possibilities: (1) the dose plan is completed: in this case the procedure is over, (2) the needle must be still inserted in a different track to complete the dose plan. In the second above-mentioned scenario, anatomy movements induced by the retraction of the needle may have occurred. Therefore, the dose plan and needle insertion sequence are updated as previously (cf. **Task 3**) with MR-based feedback on the anatomy.

- The process is repeated from **Task 2** until the procedure is completed.

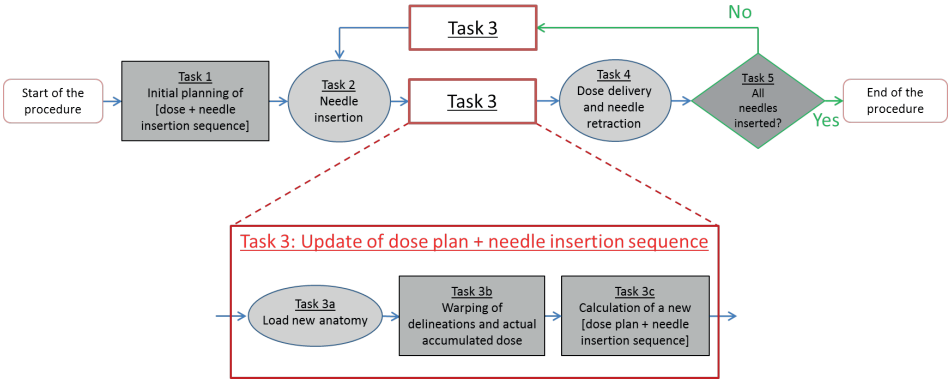

Figure 6.1: Proposed pipeline consisting in the update of the dose plan and needle insertion sequence with feedback on the intra-procedural anatomy movements. In the current manuscript, we focus on the development and on the assessment of a method designed to calculate the optimal dose plan and needle insertion sequence (i.e. Task 3). The optimization tasks are represented by a rectangle, the interventional tasks by an oval and the decision task by a diamond.

6.2.2.2 Calculation of needle insertion sequence and dose plan (Task 3)

Reaching Task 3, the anatomy may have changed due to the insertion or retraction of the needle. The new anatomy is loaded (Task 3a) and the delineations and actual accumulated dose are warped on the new anatomy grid (Task 3b). Subsequently, the dose plan and the needle insertion sequence are both updated, based on a feedback on the anatomy movements, as follows. The dose plan was evaluated using the method described in Borot de Battisti *et al* (2016a), the latter being specifically designed for the single needle MR-compatible robot developed at the UMCU. We recall that this robot inserts the needle in a divergent way due to the narrow MR-bore, and delivers the dose needle-per needle. The main feature of this algorithm is to simulate a dose plan, using such a robot, based on anatomy delineations and measured needle position, within 2 minutes of computation time. In the seminal scientific paper, the anatomy was considered to be static during the procedure (i.e. the position of the target and OARs were evaluated from a MRI image acquired at the beginning of the treatment). In the current study, the dose plan and needle insertion sequence are updated in Task 3c using the warped anatomy delineations and accumulated dose.

6.2.3 Proposed framework for the simulation of anatomy deformations

In order to assess the performance of the system, we propose to simulate brachytherapy intervention. For that purpose, a framework is presented in this section, to

model the anatomy deformation occurring during the intervention.

At the beginning of the intervention, we start with the initial anatomy which consists in the prostate tumors and the OAR considered (urethra, bladder and rectum), delineated from the MR-data of a patient. Then, in the course of the procedure, intra-procedural anatomy movements are simulated. For that, we assume that deformations are induced by needle insertion and retraction. On the base of articles in literature which investigated intrafraction prostate movements during the course of brachytherapy intervention, two types of motion model were implemented:

Translation model: Each time a needle is inserted, we considered that the prostate is instantaneously pushed by the needle: For that we simulated a prostate translation of $0.9mm$ along the caudo-cranial direction induced by each needle insertion. This motion model is line with the study of Lagerburg *et al* (2006) who showed that the mean prostate motion was $0.9mm$ when the needle was tapped into the prostate with a robotic system.

Rotation model: The needle's insertion and retraction induced a rotation of the prostate around its center of gravity: For that, a rotation of the prostate around the normal axis of the plane formed by the needle and the gravity center was applied. The rotation angle α was assumed to be linear with the Euclidean distance between the prostate gravity center and the needle. It was therefore expressed as follows:

$$\alpha = a \cdot d \tag{6.1}$$

where d is the minimum distance between the center of gravity and the needle, and:

$$\begin{cases} a = 0.6°/mm & \text{when the needle is inserted} \\ a = -0.3°/mm & \text{when the needle is retracted} \end{cases} \tag{6.2}$$

This motion is, in order of magnitude, in line with the study of Lagerburg *et al* (2005) who measured the prostate rotation angle due to needle retraction. In particular, Lagerburg *et al* found that, in the worst case scenario (without the use of a locking needle), the prostate rotation in the sagittal plane could be expressed as: $-0.42 + 0.26d$.

Moreover, in order to obtain a synthetic 3D motion field within the complete image field-of view, a regularization of the motion around the prostate is applied: that way, we can match real organ deformations by mimicking movements of neighboring tissues induced by the moving organ. To illustrate the implementation of the anatomy motion, let's suppose the "rotation model" where needle insertion induces a prostate rotation (cf. figure 6.2 corresponding to anatomy of Patient 1 in the planning study). Before insertion of the needle, the anatomy and delineations are known (figure 6.2(a)). The insertion of the needle will induce a rotation of

the prostate around its center of gravity: the imposed prostate motion is defined (figure 6.2(b) and (c)). A regularization of the movement outside the prostate is then applied (figure 6.2(d) and (e)). The interested reader is referred to the Appendix for additional details about the employed algorithm. Knowing the voxelwise deformation field, both delineations and the actual accumulated dose can be propagated on the new anatomy grid.

6.2.4 Experimental protocol

To assess the performance of our MRI-brachytherapy hybrid system, MR-guided HDR prostate brachytherapy was simulated on 15 patients with varying number of needle insertions ($N_{needle} = [2, 4, 6, 8, 10, 12, 14]$). Intra-procedural anatomy changes were simulated using the framework proposed in section 6.2.3. For each scenario, the simulated brachytherapy procedures followed the pipeline described in figure 6.1. Two situations were compared: (I) with and (II) without replanning during the intervention (i.e. with and without Task 3c respectively).

6.2.4.1 Anatomy

Between May 2013 and April 2016, 30 patients were treated by focal MR-guided focal HDR prostate brachytherapy as monotherapy at the UMCU according to the current practice: catheters were first inserted manually under TRUS-guidance with the support of a template grid, and needle reconstruction and dose planning were then assessed using MRI. These patients had localized prostate cancer with a prostate-specific antigen (PSA) level lower than $10\,\mathrm{ng\,ml^{-1}}$ and a Gleason score of 7 or less. The intra-operative MR-data – taken directly after the needles were in place – of the first 15 consecutive patients were included in the simulation study. The anatomy of the patients was obtained using the delineations of the prostate tumors and the OAR considered (urethra, bladder and rectum) on $1mm^3$ resolution MR images by an experienced oncologist. The acquisition of patient MR images used in this study was approved by the Institutional Review Board (IRB). The PTV ranged from $9.5mL$ to $36.4mL$ with a median of $24.3mL$.

6.2.4.2 Model of dose calculation

To simulate the dose deposition, the dose rate around the source was calculated using the point source approximation model because of its reduced computation time, with a small adaptation as follows to avoid over-optimization of the dose close to the source:

$$d_i(\boldsymbol{r}) = S_K \Lambda g_P[R_i(\boldsymbol{r})] \Phi_{an}[R_i(\boldsymbol{r})] \frac{{R_0}^2}{R_i(\boldsymbol{r})^2 + \exp[-R_i(\boldsymbol{r})^2]} \tag{6.3}$$

where $d_i(\boldsymbol{r})$ is the dose rate of the i^{th} source position at $\boldsymbol{r}$, S_K is the air-kerma strength, Λ the dose-rate constant in water, $\Phi_{an}(R)$ the one-dimensional anisotropy factor, R_0 the reference distance which is specified to be $10mm$, $g_P(R)$ the radial

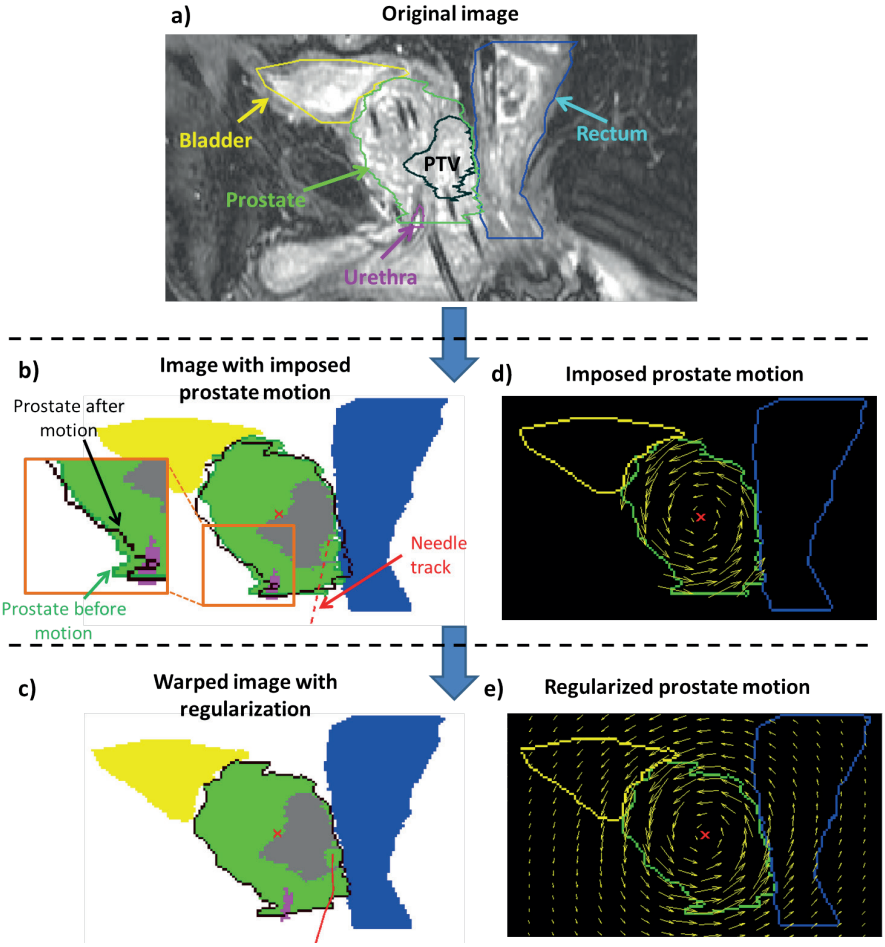

Figure 6.2: Implementation of intra-procedural anatomy movements. For illustration, a needle insertion is simulated in the scenario where the anatomy movements follow the "rotation model". The anatomy corresponds to MR data of Patient 1 in the planning study. Starting from a known anatomy with delineations of PTV, prostate, bladder, urethra and rectum (figure (a)), the prostate motion is defined according to the motion model: Figure (b) represents the different regions before and after the defined motion and figure (c) represents the defined motion with the initial delineations. Then a regularization of movement is performed for the region outside the prostate to obtain a smooth anatomy movement. Figure (d) represents the final anatomy position and figure (e) the final motion and delineations.

dose function in the case of the point source approximation model and $R_i(\boldsymbol{r})$ the distance (in millimeters) between the i^{th} source position at coordinate $\boldsymbol{r}_i$ and $\boldsymbol{r}$ ($R_i(\boldsymbol{r}) = ||\boldsymbol{r}_i - \boldsymbol{r}||_2$). With this adaptation of the point source model, the dose has an upper limit value close to the source, therefore it reduces the numeric instabilities for $R_i(\boldsymbol{r})$ approaching 0. TG43 constants, anisotropy factor and radial dose function for the microSelectron-HDR (Elekta/Nucletron, Veenendaal, The Netherlands) 192-Iridium source were taken from a study of Daskalov *et al* (1998) ($\Lambda = 1.108 cGy.h^{-1}.U^{-1}$) and an arbitrary source strength $S_K = 40.80 mGy.h^{-}1.m^2$ was chosen. The multiplication of the radial dose function $g_P(R)$ and the anisotropy factor $\Phi_{an}(R)$ was approximated by a 2^{nd} order polynomial fit ($g_P(R) \cdot \Phi_{an}(R) = a_0 + a_1 R + a_2 R^2$). The coefficients for the fit were $a_0 = 1.11$, $a_1 = -3.30 \cdot 10^{-3}$ and $a_2 = 3.12 \cdot 10^{-6} mm^{-2}$, where R is in millimeters.

6.2.4.3 Assessment of the proposed planning adaptation strategy

To assess the proposed planning adaptation strategy, we evaluated for each simulated intervention:

- The initial dose parameters (noted $D^i_{95\%\ PTV}$, $D^i_{10\%\ Ur}$, $D^i_{1cc\ Rec}$ and $D^i_{1cc\ Bl}$) calculated from the initial dose plan at the beginning of the intervention.
- The final dose parameters, determined from the accumulated dose at the end of the intervention and noted $D^f_{95\%\ PTV}$, $D^f_{10\%\ Ur}$, $D^f_{1cc\ Rec}$ and $D^f_{1cc\ Bl}$.
- The difference in percentage between initial dose parameters and final parameters, noted $D^{diff}_{95\%\ PTV}$, $D^{diff}_{10\%\ Ur}$, $D^{diff}_{1cc\ Rec}$ and $D^{diff}_{1cc\ Bl}$. Those values evaluate how close was the final accumulated dose compared to the initially planned dose and are expressed as follows:

$$D^{diff}_{volume} = 100 \cdot (D^f_{volume} - D^i_{volume})(D^i_{volume})^{-1}$$
$$\text{with } volume = \{95\%\ PTV, 10\%\ Ur, 1cc\ Rec, 1cc\ Bl\}. \quad (6.4)$$

6.3 Results

The results from brachytherapy simulations where the intra-procedural anatomy movements followed the "translation model" are presented in figure 6.3. The final dose distribution of a typical patient is presented in figure 6.3(a) and (b) for a brachytherapy intervention with 12 needle insertions ($N_{needle} = 12$): the situation without and with re-optimization of the needle insertion sequence and the dose plan are displayed respectively. It is noticeable that the cranial extremity of the PTV is better covered with replanning compared to the situation without replanning. The initial and final dose parameters of all patients as function of the number of needle insertions are presented in figure 6.3 (c), (d), (e) and (f) respectively: for [2,4,6,8,10,12,14] needle insertions, the median of $D^i_{95\%\ PTV}$, $D^i_{10\%\ Ur}$, $D^i_{1cc\ Rec}$, $D^i_{1cc\ Bl}$ over all patients were [17.0, 19.1, 19.1, 19.6, 19.7, 20.1, 20.2],

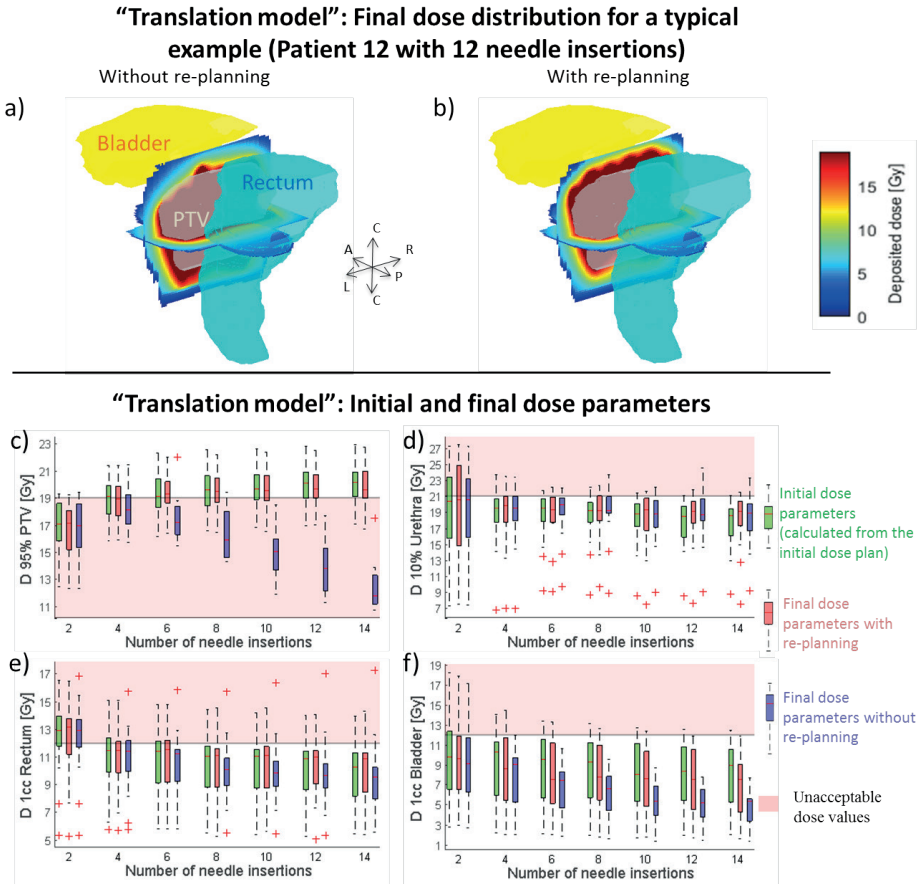

Figure 6.3: Typical results of brachytherapy simulations where intra-procedural anatomy movements are modeled by the "translation model" (needle insertion induced translation of prostate in the cranial direction). Figure (a) and (b) present the final dose distributions of a typical brachytherapy simulation on a patient treated with 12 needle insertions in the situation without and with update of dose plan and needle insertion sequence, respectively. Figure (c), (d), (e) and (f) present the initial and final dose parameters for all patients as function of the number of needle insertions.

[20.4, 19.5, 19.5, 19.2, 18.8, 18.5, 18.5], [12.9, 11.5, 11.4, 11.0, 11.0, 10.9, 10.3] and [9.8, 10.3, 9.5, 9.3, 8.1, 8.4, 9.0] Gy respectively. The median of the final dose parameters when the replanning is performed were, in Gy, [17.1, 18.9, 19.3, 19.5, 19.5, 19.7, 19.6], [20.6, 19.8, 19.3, 19.2, 19.3, 19.1, 19.1], [13.2, 11.5, 11.5, 11.1, 11.1, 11.0, 10.9] and [9.6, 8.6, 7.6, 7.8, 7.7, 7.6, 7.6] respectively. Without replanning, the median of the final dose parameters over all patients were, in Gy, [16.9, 18.1, 17.2, 15.9, 15.0, 13.8, 11.8], [20.5, 19.6, 20.0, 19.2, 18.8, 18.7, 18.9], [12.9, 11.4, 11.3, 10.1, 9.9, 9.7, 9.5] and [9.2, 9.0, 7.5, 6.6, 5.5, 5.3, 5.5].

The results obtained from the brachytherapy simulated with the "rotation model" are displayed in figure 6.4. The final dose distributions of a typical example of a patient treated with 12 needle insertions are depicted in figure 6.3(a) and (b), without and with replanning respectively. When replanning is performed, the coverage of the PTV is better: In particular, without replanning, cold spots can be observed on the cranial side of the PTV, and more dose is delivered to the urethra in comparison to the situation with replanning. The initial and final dose parameters of all patients as a function of the number of needle insertions are depicted in figure 6.3(c), (d), (e) and (f) respectively. For [2,4,6,8,10,12,14] needle insertions, the median of $D^i_{95\%\ PTV}$, $D^i_{10\%\ Ur}$, $D^i_{1cc\ Rec}$, $D^i_{1cc\ Bl}$ over all patients were the same as the previous experiment (the same patients' MR-data were used). The median of $D^f_{95\%\ PTV}$, $D^f_{10\%\ Ur}$, $D^f_{1cc\ Rec}$, $D^f_{1cc\ Bl}$ with replanning were [17.2, 18.7, 19.2, 19.6, 19.8, 20.2, 20.0], [19.8, 19.2, 20.2, 19.3, 19.0, 19.5, 18.9], [13.2, 11.6, 11.3, 11.1, 11.0, 10.8, 10.6] and [9.6, 10.5, 8.5, 9.1, 9.0, 8.5, 8.1] Gy. Without replanning, the median of $D^f_{95\%\ PTV}$, $D^f_{10\%\ Ur}$, $D^f_{1cc\ Rec}$, $D^f_{1cc\ Bl}$ were [17.1, 19.1, 18.6, 18.9, 18.6, 18.0, 16.2], [20.1, 19.8, 21.1, 21.3, 21.8, 23.1, 22.9], [12.9, 11.2, 11.4, 10.7, 10.9, 10.5, 10.6] and [10.0, 11.0, 9.2, 8.3, 7.4, 7.2, 8.1].

The value of $D^{diff}_{95\%\ PTV}$, $D^{diff}_{10\%\ Ur}$, $D^{diff}_{1cc\ Rec}$ and $D^{diff}_{1cc\ Bl}$ averaged over all patients and all different numbers of needle insertions are noted $\overline{D^{diff}_{95\%\ PTV}}$, $\overline{D^{diff}_{10\%\ Ur}}$, $\overline{D^{diff}_{1cc\ Rec}}$ and $\overline{D^{diff}_{1cc\ Bl}}$, and depicted in figure 6.5. With the "translation model", $\overline{D^{diff}_{95\%\ PTV}}$, $\overline{D^{diff}_{10\%\ Ur}}$, $\overline{D^{diff}_{1cc\ Rec}}$ and $\overline{D^{diff}_{1cc\ Bl}}$ are equal to -17.5%, 3.2%, -1.7% and -24.1% without replanning and -0.6%, 1.0%, 1.3% and -6.0% with replanning. With the "rotation model" , the values of $\overline{D^{diff}_{95\%\ PTV}}$, $\overline{D^{diff}_{10\%\ Ur}}$, $\overline{D^{diff}_{1cc\ Rec}}$ and $\overline{D^{diff}_{1cc\ Bl}}$ are -6.3%, 16.4%, -0.8% and -2.3% without replanning and -1.3%, 2.6%, -0.4% and 3.9% with replanning.

Finally, the computation time of the update of dose plan and needle insertion sequence was less than 2 minutes.

6.4 Discussion

In this study, we developed a strategy of intrafraction replanning during HDR prostate brachytherapy intervention, with MR-based feedback on the anatomy deformation. The stategy can be applied in the context of a MRI-brachytherapy hybrid system where the anatomy deformation during treatment is evaluated on-

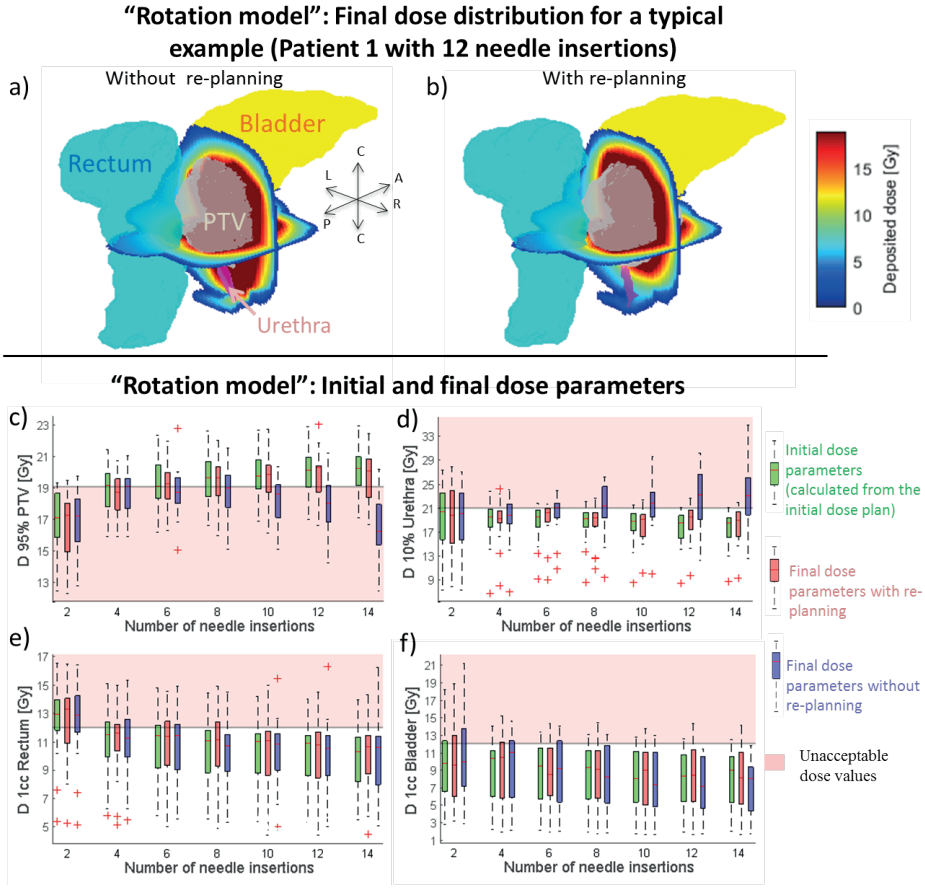

Figure 6.4: Typical results of brachytherapy simulations where intra-procedural anatomy movements are modeled by the "rotation model" (needle insertion and retraction induced rotation of prostate around its center of gravity). Figures (a) and (b) show the final dose distributions for a typical brachytherapy simulation on a patient treated with 12 needle insertions in the situation without and with update of dose plan and needle insertion sequence, respectively. Figures (c), (d), (e) and (f) present the initial and final dose parameters for all patients as function of the number of needle insertions.

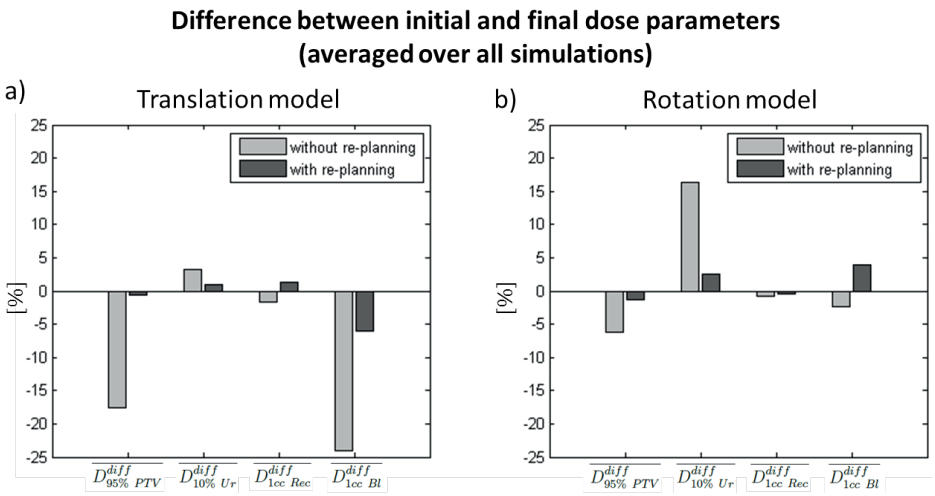

Figure 6.5: Difference in percentage between initial and final dose parameters averaged over all simulations using a) the "translation model" and b) the "rotation model" for the intrafraction anatomy motion. In grey: Interventions without replanning. In black: Interventions with replanning.

line with MRI. The performance of a MRI-brachytherapy hybrid system was assessed as follows: MR-guided HDR prostate brachytherapy was simulated with varying number of needle insertions ($N_{needle} = [2, 4, 6, 8, 10, 12, 14]$), using the MR data of 15 patients. Two different models were tested to mimic the intraprocedural anatomy movements: (1) The needle insertion induced a translation of the prostate in the cranial direction, (2) the needle insertion and retraction induced a prostate rotation around its center of gravity.

For both anatomy motion models, the accumulated dose at the end of the intervention was better when the proposed strategy was employed compared to the situation when no replanning was performed. In the typical example presented in figure 6.3(a) and (b) where the needle insertion induced a prostate translation: when no re-optimization was performed, the cranial side of the PTV presented cold spots while the healthy tissue situated close to the caudal side of the PTV received a high dose. This observation was expected because the prostate shifted in the cranial direction during the intervention. However when replanning was performed, the PTV was better covered because the dose plan and sequence update took into account the anatomy motion. The dose parameters of all tested patients (presented in figure 6.3(c), (d), (e) and (f)) confirmed those observations: $D^{f}_{95\%\ PTV}$ was overall higher when replanning was performed compared to the situation without re-planning (regarding the OARs, the final dose parameters with and without replanning differed moderately). In particular without replanning, the median of $D^{f}_{95\%\ PTV}$ over all patients was inferior to $19Gy$ for each tested number of needle insertions and therefore unacceptable clinically. With replan-

ning, all medians of final dose parameters were acceptable clinically when the intervention was performed with 6 needle insertions or more. It is also noticeable that $D^{f}_{95\%\ PTV}$ without replanning was decreasing with the number of needle insertions compared to the initial dose plan: In particular, for 14 needle insertions, the median of $D^{f}_{95\%\ PTV}$ ($11.8Gy$) decreased 42% compared to the median of $D^{i}_{95\%\ PTV}$ ($20.2Gy$). Those observations were expected because a higher number of needle insertions will cause bigger change in anatomy over the whole course of the intervention: in the situation without replanning, the initially planned dose may not be suited anymore to the current anatomy, leading to sub-optimal dose deposition. Similar trends were observed when the needle insertion and retraction induced a rotation of the prostate (cf. figure 6.4). The typical example presented in figure 6.4(a) and (b) shows that the dose coverage was better using the proposed replanning strategy: Without replanning, the coverage of the PTV cranial side was insufficient and hotspots of the healthy tissue could be observed surrounding the caudal side of the PTV. This was expected because, in the course of the intervention, the prostate rotated and tended to reach the stability position where the PTV is on the cranial side of the prostate (therefore the PTV tends to go "up"). Same observations can be made regarding the dose parameters for all patients (cf. figure 6.4(c), (d), (e) and (f)): with re-optimization, the final dose parameters differed moderately compared to the initial dose plan. Moreover, over all patients, the medians of final dose parameters were acceptable clinically for interventions performed with 8 needle insertions or more. However, without replanning, the $D^{f}_{95\%\ PTV}$ decreased and $D^{f}_{10\%\ Ur}$ increased as function of the number of needle insertion due to larger anatomy motion amplitude induced by the needle insertions and retractions. In particular, for 14 needle insertions, the median of $D^{f}_{95\%\ PTV}$ ($16.2Gy$) decreased 20% and the median of $D^{f}_{10\%\ Ur}$ ($22.9Gy$) increased 24% compared to the median of $D^{i}_{95\%\ PTV}$ ($20.2Gy$) and $D^{i}_{10\%\ Ur}$ ($18.5Gy$) respectively. Moreover, the median of $D^{f}_{95\%\ PTV}$ was clinically unacceptable for each tested number of needle insertion. Finally, it is interesting to remark that the difference between the initial and final dose parameters when replanning was performed, was moderate compared to the situation without replanning (cf. figure 6.5): with replanning, the difference stayed within $\pm 6.0\%$ on average over all interventions. However, without replanning, the dose at the PTV decreased 17.5% with the "translation model" and the dose at the urethra increased 16.4% with the "rotation model" on average compared to the initial dose plan.

Several limitations can be noticed in this study. First, the assessment of the proposed strategy is based on brachytherapy simulations: anatomy movements were modeled such that movements were induced by needle insertion and retraction although in clinical practice, other motion in the pelvic region can occur, e.g. peristaltic motion (bladder or rectum filling). Moreover, the anatomy motion modeled in the simulations (prostate's rotation or translation induced by needle insertion or retraction) may not be conform to what actually happens in clinic: more complex movements may be related to the needle trauma such as prostate swelling or deformations (Stone *et al* 2002). However, the proposed strategy is designed to take into account any type of prostate and OARs movements as long

as the delineations and the accumulated dose are monitored. Second, replanning requires an update of the anatomy grid (cf. Task 3b in the proposed pipeline). MRI can be employed to acquire the anatomy image for registration with the initial (previous) anatomy grid. That way, the delineations and accumulated dose can be warped on the new anatomy grid and used as input for the proposed replanning. The development of a deformable registration tool for MRI acquired during an MR-guided HDR prostate brachytherapy procedure will be investigated in the future. Third, the brachytherapy simulations performed in this manuscript were such that no needle positioning errors were assumed although in clinic, sub-optimal needle positioning can occur due to e.g. inaccuracy of needle insertion or needle bending. However, the pipeline proposed in this manuscript is adapted from the method of Borot de Battisti *et al* (2016a and 2017) where dose plan and needle insertion sequence are updated with feedback on sub-optimal needle positioning. Therefore, we expect the proposed method to be compatible with the update of the dose plan and needle insertion sequence while taking into account the anatomy changes as well as needle positioning errors. Fourth, regarding the dose distribution model, the point source approximation was employed to calculate the accumulated dose, due to implementation simplicity as well as computational speed considerations. However, it is important to notice that the proposed strategy allows more precise source models such as line source approximation.

The proposed replanning strategy was presented for a specific brachytherapy set-up consisting of divergent needle configuration, MRI guidance, and needle per needle dose delivery. However, with some appropriate adjustments, the proposed pipeline may also be compatible with parallel needle configuration and/or CT or US guidance.

6.5 Conclusion

In this manuscript, we presented a new strategy for intrafraction update of dose plan and sequence during HDR prostate brachytherapy, with MR-based feedback on the anatomy deformation. This strategy is designed for MRI-brachytherapy hybrid systems which provide online MR-based anatomy deformation. Our simulations showed that an intrafraction re-planing using an MR-feedback of anatomy deformations is beneficial, and that a clinically acceptable dose may be delivered using at least 6 needle insertions. Moreover, a moderate difference ($< 6.0\%$ in average) between initial and final clinical constraints (i.e. $D_{95\%\ PTV}$, $D_{10\%\ Ur}$, $D_{1cc\ Rec}$ and $D_{1cc\ Bl}$) was obtained using our approach. However, if no replanning is performed during treatment, a decrease up to 17.5% of $D_{95\%\ PTV}$ and an increase up to 16.4% of $D_{10\%\ Ur}$ was observed depending on the intrafraction anatomy motion. Therefore, we demonstrate that a MRI-brachytherapy hybrid system is promising in order to take into account anatomy deformation during HDR prostate brachytherapy and to deliver a clinical acceptable dose.

Appendix. Simulation of MR images with an imposed anatomy motion

This appendix describes the methodology employed to obtain a synthetic 3D motion field within the complete image field-of-view, when displacements are locally imposed solely on specific organs..

Let $\vec{V}_{imp} = (u_{imp}, v_{imp}, w_{imp})$ and $\vec{V} = (u, v, w)$ be the imposed and final motion vector fields, respectively. Let M be the binary mask defined as follows: a value of one is given to the voxels where the movement is imposed and zero for the remaining voxels. We propose a function which imposes $\vec{V}$ to equal $\vec{V}_{imp}$ within M, with an additional spatial regularity constraint supposed to match real organ deformations. The final motion $\vec{V}$ can be obtained by minimizing the following objective function $E(u, v, w)$:

$$E(u,v,w) = \iiint_{\Omega} \Big[M(\|u_{imp} - u\|_2{}^2 + \|v_{imp} - v\|_2{}^2 + \|w_{imp} - w\|_2{}^2) + \alpha(\|\vec{\nabla} u\|_2{}^2 + \|\vec{\nabla} v\|_2{}^2 + \|\vec{\nabla} w\|_2{}^2) \Big] d\vec{r} \quad (6.5)$$

where Ω is the image coordinates domain and α a regularization parameter designed to link both the defined motion fidelity term (first term of the addition) and the regularization term (second term of the addition).

The Euler-Lagrange equations applied on $E(u, v, w)$ provide the following system of equations for each $\vec{r} \in \Omega$:

$$\begin{cases} M(u_{imp} - u) - \alpha \Delta u = 0 \\ M(v_{imp} - v) - \alpha \Delta v = 0 \\ M(w_{imp} - w) - \alpha \Delta w = 0 \end{cases} \quad (6.6)$$

We have therefore a set of $3 \times |\Omega|$ equations with common unknowns u, v and w. The Laplacian operator Δ was approximated by $\Delta u = \bar{u} - u$, where $\bar{u}$ is the average value of u using the neighboring pixels. The solutions u, v and w can thus be found iteratively through the following explicit fixed-point scheme:

$$\begin{cases} u^{n+1} = (\alpha \bar{u}^n - M u_{imp})(\alpha - M)^{-1} \\ v^{n+1} = (\alpha \bar{v}^n - M v_{imp})(\alpha - M)^{-1} \\ w^{n+1} = (\alpha \bar{w}^n - M w_{imp})(\alpha - M)^{-1} \end{cases} \quad (6.7)$$

where $n + 1$ denotes the new iteration.

The residual $\|\vec{V}^{n+1} - \vec{V}^n\|_2$ was evaluated and compared to a maximal allowed tolerance of 10^{-3} to ensure the convergence. Moreover, the regularization parameter α was empirically set to a value of 0.2 in order to avoid non continuous motion estimates.

CHAPTER 7

Summary, general discussion and perspectives

In this thesis, we developed new methodologies which aim to tackle two issues that are likely to occur during MR-guided HDR prostate brachytherapy: needle positioning errors and changes of anatomy. We also developed a MR compatible needle tracking system based on FBG sensors which can measure the position of a needle with performance comparable or superior to current MR-based methods.

7.1 Summary

In **chapter 2**, a fast method to determine the optimal dose plan was presented for focal HDR prostate brachytherapy with divergent needle configuration. A complete optimizer workflow was proposed which includes the determination of (1) the position of the center of rotation, (2) the needle angulations and (3) the dwell times. Unlike most currently used optimizers, no prior selection or adjustment of input parameters such as minimum or maximum dose or weight coefficients for treatment region and organs at risk is required. To test this optimizer, a planning study was performed on 10 patients (treatment volumes ranged from $8.5cm^3$ to $23.3cm^3$) by using 2 to 14 needle insertions. The total computation time of the optimizer workflow was below 20 minutes at the time of the publication of the manuscript in 2015 and clinically acceptable plan was reached on average using only four needle insertions. The computation was afterwards shortened to less than 5 minutes by optimizing the source code without affecting the results (in particular, the memory management was upgraded: the dose was not calculated on the whole field of view of the MR image, but only on the organs of interest with an additional margin which reduced significantly the amount of operations).

However, two major events are likely to modify the pre-planned dose distribution during the interventional process: needle positioning errors and changes of anatomy. The ultimate goal is therefore to develop a fully automatic control system, where the dose plan and the needle insertion sequence are re-optimized during the intervention according to the two aforementioned perturbations.

Chapter 3 made a step towards this ultimate goal. This chapter presented a dose plan adaptation strategy to address the first aforementioned event: a dose plan is made at the beginning of the interventional procedure and updated after each needle insertion in order to compensate for possible needle positioning errors. The proposed feedback strategy was tested by simulating complete HDR procedures with and without feedback on 8 patients with different number of needle insertions (varying from 4 to 12). In 97% of the cases tested, the number of clinically acceptable plans obtained at the end of the procedure was larger with feedback compared to the situation without feedback. Furthermore, the computation time of the adjusted plan between each insertion was below $100s$ which makes it eligible for intra-operative use.

To reduce the uncertainties in the dose distributed related to needle positioning errors, two methods are possible: (1) restraining at maximum the needle positioning errors and (2) dynamically updating the dose plan with feedback on the actual catheter locations as shown in **chapter 3**. For that, the real-time deter-

mination of the needle position (consisting of tracking the needle during insertion and reconstructing the needle after insertion) is warranted. For this purpose, a prototype system for needle tracking based on fiber Bragg gratings (FBG) sensing was investigated in **chapter 4**: the system involves a MR-compatible stylet composed of three optic fibers with nine sets of embedded FBG sensors each. This stylet can be inserted into brachytherapy needles and allows a fast measurement of the needle deflection. In this study, the aim was to assess the potential of FBG-based sensing for real-time needle (including catheter or tube) tracking during MR-guided intervention. First, the MR compatibility of FBG-based sensing and its accuracy was evaluated. Different known needle deflections were measured using FBG-based sensing during simultaneous MR-imaging. Then, a needle tracking procedure using FBG-based sensing was proposed. This procedure involved a MR-based calibration of the FBG-based system performed prior to the interventional procedure. The needle tracking system was assessed in an experiment with a moving phantom during MR imaging. The accuracy of the FBG-based system was investigated by comparing the gold-standard shapes, the shape manually segmented on MRI and the FBG-based measurements. The results showed that the proposed FBG-based needle tracking procedure is able to determine the position of the complete needle, under MR-imaging, with better accuracy and precision, higher update rate and lower latency compared to current MR-based needle localization methods. Moreover, the update rate of the needle position measurement is $100ms$ and its latency $300ms$. This system would be eligible for MR-guided brachytherapy, in particular for an improved needle guidance and reconstruction.

In the dose plan adaptation strategy presented in **chapter 3**, the needle insertion sequence is left to the doctor and may thus be potentially sub-optimal. A tool to assist the doctor in determining the optimal needle insertion sequence would therefore be of great interest. Moreover, it is a step towards the development of a fully automatic control system, where the dose plan and needle insertion sequence are automatically re-optimized during the intervention. **chapter 5** presented a new planning method which aims at determining and updating automatically the needle insertion sequence during the intervention. This strategy is based on the determination of the most sensitive needle track. The sensitivity of a needle track is defined as its impact on the dose distribution in case of sub-optimal positioning. A stochastic criterion was thus presented to determine each needle track sensitivity based on needle insertion simulations. To assess the proposed sequencing strategy, HDR prostate brachytherapy was simulated on 11 patients with varying number of needle insertions. Sub-optimal needle positioning was simulated at each insertion (modeled by typical random angulation errors). In 91% of the scenarios, the dose distribution improved when the needle was inserted into the most compared to the least sensitive needle track. The computation time for sequencing was less than 6s per needle track. The proposed needle insertion sequencing can therefore assist in delivering an optimal dose in HDR prostate brachytherapy.

Finally, **chapter 6** addressed the second perturbation which is likely to occur during a brachytherapy intervention: anatomy changes. We harnessed the MRI compound of the MRI-brachytherapy robotic hybrid system developed at the UMCU:

a new paradigm was investigated, consisting in the intrafraction update of the dose plan and needle insertion sequence during treatment, with MR-based feedback on the anatomy deformations. The performance of the MRI-brachytherapy hybrid system was then evaluated by simulating MR-guided HDR prostate brachytherapy interventions performed on 15 patients, with varying number of needle insertions (from 2 to 14), with and without intrafraction re-planning. To mimic organ displacements during the intervention, two motion simulation models were tested as follows: needle insertions and retraction induced (1) a translation and (2) a rotation of the prostate, resulting in an incremental shift of the target and OARs during treatment. For each intervention simulation, a higher PTV dose was delivered to the patient when re-planning is performed during the intervention, compared to the situation without dose plan update: In particular, with re-planning during the intervention, a clinically acceptable dose was delivered on average with 6 needle insertions or more. Moreover, the difference between initial dose parameters (calculated at the beginning of the treatment) and the final dose parameters was on average within 6.0%. However without re-planning, $D_{95\% \ PTV}$ decreased 17.5% with the translation motion model and $D_{10\% \ Ur}$ increased 16.4% with the rotation motion model, on average. In particular, the difference was increasing with the number of needle insertions. With the proposed strategy, the MRI-brachytherapy hybrid system can take into account anatomy deformations during HDR prostate brachytherapy in order to deliver clinically acceptable dose plans.

7.2 General discussion

7.2.1 Dose planning algorithm for HDR prostate brachytherapy with divergent needle configurations

Chapter 2 presents and evaluates a novel dose planning optimization method for HDR prostate brachytherapy with divergent needle configurations. Unlike most optimizers such as HIPO or IPSA, the proposed method does not require individual adjustments of several input parameters such as minimum dose, maximum dose or weight coefficients for PTV and organs at risk to obtain an acceptable plan (Dinkla *et al* 2014). Moreover, the planning optimization algorithms that are clinically used or described in literature are usually based on iterative methods (Holm *et al* 2013, Gorissen *et al* 2013 and Siauw *et al* 2012) which cause two problems. First, such algorithms strongly depend on the initialization and therefore could produce sub-optimal solutions due to the trapping in local minima regions of the cost function landscape. The second problem is that, due to the high non-convexity of the problem, the optimization may require a long calculation time. To avoid these problems, a different approach was chosen: (1) The center of rotation is determined exhaustively according to the patient anatomy and the capabilities of the robot, (2) the angulation of the needle tracks is determined by evaluating several heuristics chosen carefully using the k-means clustering and (3) the dwell times are efficiently optimized by solving linear equations. Finally, the total computation time of the optimizer workflow was below 20 minutes and a clinically acceptable plan was

reached on average using at least four needle insertions (as a comparison, 13 to 17 needles are usually inserted in the current clinical practice of HDR prostate brachytherapy,). It is important to note that the program has been developed on Matlab and has not been optimized for speed. The proposed pipeline and the employed numerical schemes thus show great perspectives for a further reduction of the computation time using Graphical Processing Units (GPU's) in a parallel architecture.

In this study, an open number of needle insertions was chosen. In practice, a compromise has to be found: It is clear that the more needle insertions there are, the better the dose distribution will be. However, the influence of adding one or more needle insertions may lead to additional toxicity: Vargas *et al* (2005) and Boyea *et al* (2007) showed that the urinary toxicity following HDR brachytherapy is significantly increased when using more than 14 needle insertions. For those reasons, we think that an automatic determination of the number of needle insertions requires additional works and we decided to perform the simulations for different number of needle insertions (from 4 to 12). A range of 4–12 needle insertions was chosen because, for this range, clinically acceptable dose plans for all patients were obtained. Furthermore, although the proposed optimizer was implemented with the point source approximation for simplicity of calculation, the proposed method allows the use of more precise source models such as the line source approximation. Finally, the planning study of the proposed optimizer shows promising results. The clinical constraints set as input were reached on average with 4 needle insertions which is better compared to the current clinical procedure where 13 to 17 needles are usually inserted (see Hsu *et al* 2004, Menard *et al* 2004).

It is important to note that the proposed optimization method is based on soft constraints, i.e. in the cost function, variables are penalized if the clinical constraints are not reached. However, it can be useful in certain clinical situations to impose hard constraints of dose for defined regions, which set conditions for the variables that are required to be satisfied : a hard constraint could be e.g. to impose a minimum dose to the target or a maximum dose to a defined OAR. In this scenario, the corresponding cost function would not be linear anymore: the minimization of the cost function must therefore be determined using a gradient-based optimizer on all parameters at the same time (point of rotation, needles angles and dwell times) based on the cost function that is being minimized.

7.2.2 Adaptive dose planning strategy with feedback on needle positioning errors

In **chapter 3**, a dose plan adaptation strategy for HDR prostate brachytherapy for the robotic brachytherapy set-up developed at the UMCU is described and assessed. This strategy consists in the update of the dose plan during treatment with feedback on the needle position. The strategy proposed in this manuscript supposed that the position of the needle can be measured. For that, MRI or other MR compatible localization methods can be used: an active MRTR system

was recently developed to provide accurate and rapid localization of interstitial brachytherapy catheters (Wang *et al* 2015) and we describe in **chapter 4** a needle tracking system based on FBG sensors that has the advantage to be MR compatible and provide real-time and accurate measurement. Moreover, this system may also be valuable in case signal voids from blood vessels, calcifications or other artefacts make image interpretation difficult.

Furthermore, the study presented in **chapter 3** shows that the proposed re-optimization strategy on the needle positioning results in dose plans with a significantly better quality compared to the scenario without re-optimization. For all simulations performed, the percentages of clinically acceptable final dose plans were on average 47.8% without re-optimization and 86.4% with re-optimization. This points out that the re-optimization procedure is able to compensate for the angulation error during insertion. Furthermore, all the simulations and dose re-plannings of the validation study were done completely automatically (no human interaction was involved in the process). The algorithm was implemented in Matlab 2015. The computation time of the re-optimization of the dose plan took less than $100s$. The re-optimization procedure is therefore eligible for intra-operative use.

A limitation of this study is mainly due to the difference between the model chosen for the intervention simulations and what actually happens in clinics: only the needle angulation errors were taken into account although more complex problems may occur during insertion such as needle bending or modification of the patient anatomy during treatment. However, the proposed pipeline is compatible with a re-optimization of the dose plan parameters after each insertion of the needle while taking into account those issues thanks to the proposed experimental setup: in terms of hardware, the robotic device developed in our institution is designed such that the needle can be inserted under MRI guidance, and, in terms of software, the calculation time of the optimizer is eligible for intra-operative use. Moreover, in order to improve the delivered dose distribution the strategy should include the optimization and update of the needle sequence during treatment. The development of the strategy is described in **chapter 5** and **chapter 6**.

7.2.3 Real-time needle tracking system based on FBG sensors

Chapter 4 presents and evaluates a FBG-based sensing device which is able to track and reconstruct a needle (including catheter or tube) during a medical procedure. This study shows that this device can track a needle deflection with a high accuracy ($0.27mm$ on average) in an MR environment. In addition, the average Euclidean distance between MR and FBG-based measurements of the needle position after registration was comparable to the uncertainty of MR-based measurements (corresponding to the uncertainty of the manual segmentation) estimated at half the voxel size in the MR image. This indicates that the FBG-based sensing device is not significantly influenced by the MR environment. Finally, to determine the needle position, we proposed a simple protocol involving the fixation of the stylet base and the determination of its position and orientation using

a MR-based calibration. With this system, the needle position can be measured with an accuracy of $0.79mm$ and a precision (standard deviation) of $0.37mm$ on average in comparison to the MR-based measurement. In particular, the accuracy and precision of the needle tip is $1.10mm$ and $0.45mm$ respectively. Moreover, the update rate of the needle position measurement is $100ms$ and its latency $300ms$.

A limitation of the proposed tracking protocol arises from the fact that our system is now implemented with the stylet in a fixed support. Although this condition was fulfilled in our experiments, this may not be the case under clinical practice. In a clinical workflow, to know the position and orientation of the stylet base, it should be mounted in a flexible and tracked support that is fixed to the table. This special support could be the MR-compatible single needle robotic device currently developed at the UMCU. Knowing the needle mounting position of the robot in the MR coordinate space means that we can determine the complete shape of the needle in the MR coordinate system. In our view, the current promising results provide justification to continue investing in further improvements of the clinical implementation of the FBG tracking technology within an MR-guided workflow. The clinical benefits of such a system would be twofold:

1. For real-time tracking of needle during insertion. The fast and accurate feedback of the needle position will help the steering of the needle and warn the user in case of deviations from the planned needle track: better dose coverage and less toxicity would then be expected due to less needle positioning errors.

2. For fast and automatic reconstruction of the needle after insertion. The authors expect that with FBG tracking, less time will be spent compared to manual segmentation of a needle with possibly, a better accuracy. This would allow a shorter overall procedure time and enable update of the dose plan with feedback on the needle positioning error.

7.2.4 Adaptive needle insertion sequencing for MR-guided HDR brachytherapy

In **chapter 5**, a new automatic and adaptive needle sequencing strategy for MR-guided HDR prostate brachytherapy is proposed and evaluated by simulating MR-guided HDR brachytherapy interventions. The simulation study showed that inserting the needle into the most sensitive needle track leads to an improved dose coverage compared to inserting into the least sensitive track: When the needle insertion sequence was optimal (*i.e.* the needle is inserted into the most sensitive needle track), the dose tended to increase at the PTV and to decrease at the OARs in comparison to the situation of least optimal needle insertion sequence (*i.e.* the needle is inserted into the least sensitive needle track). Inserting the needle into the most sensitive needle track allows sub-optimal needle positioning to be compensated by the re-optimization of the subsequent needle insertions. Moreover, for some patients, the difference in the dose coverage was more pronounced for small number of needle insertions. This could be explained by the fact that the

dose delivered by each needle decreases with the number of needle insertions: For a small number of needle insertions, the dose delivered by each needle is high and there are few needles to compensate for sub-optimal positioning. Therefore, the robustness of the dose plan to sub-optimal needle positioning decreases when a small number of insertions is used. Consequently, the difference of impact on the distributed dose due to sub-optimal needle positioning between least optimal and optimal needle sequence situation is more important with a small number of needle insertions. This effect is attenuated for a large number of needle insertions.

The limitations of this study are mostly related to the limitations in the proposed brachytherapy simulations. Firstly, the anatomy was supposed to remain static throughout the procedure in order to exclude possible artifacts and uncertainties of image registration or dose accumulations. In practice, the intra-operative internal organ motion due to, for example, swelling, displacement (Stone *et al* 2002) or rotation (Lagerburg *et al* 2005) of the prostate (related to the trauma caused by the needle insertion) or intra-procedural changes in rectum or bladder filling can cause uncertainties in the delivered dose during the intervention. Those issues can be solved by performing an adaptation of the dose plan and needle insertion sequence with feedback on the anatomy changes (in addition to feedback on sub-optimal needle positioning). This is tackled in **chapter 6**: The dose plan and needle sequencing adaptation with feedback on anatomy movements is possible while performing brachytherapy treatment under MRI-guidance (but also US-, CT-guidance) for which the anatomy can be captured during the interventional procedure.

7.2.5 Adaptive planning adaptation on anatomy deformations during MR-guided HDR prostate brachytherapy

A strategy for intrafraction re-planning during HDR prostate brachytherapy intervention, with MR-based feedback on the anatomy deformation is presented and assessed in **chapter 6**. The strategy can be applied in the context of the MRI-brachytherapy hybrid system where the anatomy deformation during treatment is evaluated online with MRI. For each tested scenario, the accumulated dose at the end of the intervention was better when the proposed strategy was employed compared to the situation when no re-planning was performed. It is noticeable that the quality of the dose distributed without re-planning was decreasing with the number of needle insertions compared to the initial dose plan, although the difference between the initial dose plan and the final dose distributed with re-planning was moderate for all scenarios. Those observations were expected because a higher number of needle insertions will cause bigger change in anatomy over the whole course of the intervention: in the situation without re-planning, the initially planned dose may not be suited anymore to the current anatomy, leading to sub-optimal dose deposition.

Several limitations can be noticed in this study. First, the assessment of the proposed strategy is based on brachytherapy simulations: anatomy movements were modeled such that movements were induced by needle insertion and retraction al-

though in clinical practice, other motion in the pelvic region can occur, e.g. peristaltic motion (bladder or rectum filling). Moreover, the anatomy motion modeled in the simulations (prostate's rotation or translation induced by needle insertion or retraction) may not be conform to what actually happens in clinic: more complex movements may be related to the needle trauma such as prostate swelling or deformations (Stone *et al* 2002). However, the proposed strategy is designed to take into account any type of prostate and OARs movements as long as the delineations and the accumulated dose are monitored. Second, the brachytherapy simulations performed in this study were such that no needle positioning errors were assumed although in clinic, sub-optimal needle positioning can occur due to e.g. inaccuracy of needle insertion or needle bending. However, the pipeline proposed in this study is adapted from the strategy described in **chapter 2** and **chapter 4** where dose plan and needle insertion sequence are updated with feedback on sub-optimal needle positioning. Therefore, the proposed method is perfectly compatible with the update of the dose plan and needle insertion sequence while taking into account the anatomy changes as well as needle positioning errors.

7.3 Perspectives

In this thesis, we proposed new methodologies which aim to address two issues that are likely to occur during MR-guided HDR prostate brachytherapy: needle positioning errors and changes of anatomy. We also have described a MR-compatible system that can measure in real-time the needle position in the MR scanner with similar or better performance compared to MR-based needle tracking methods. All those studies were presented in the frame of the MR-brachytherapy hybrid set-up currently developed at the UMCU, which includes robotic needle insertion under MR guidance, divergent needle configuration and needle per needle dose delivery. It is important to point out that with some appropriate adjustments, the proposed dose planning methodologies and needle tracking can also be compatible with parallel needle configuration and/or CT or US guidance. Furthermore, the MR compatible needle tracking system based on FBG sensors can be used for other applications using needles as in biopsies.

The next steps of the work will be to implement clinically the MR-brachytherapy system i.e. treating a patient diagnosed with prostate cancer. For this goal, several milestones must be achieved. First, in current practice, the anatomy of the patient is assessed by manually delineating organs and tumor on MR-images acquired before and during the procedure which is time-consuming and operator-dependent: the development of a deformable registration tool and automatic delineation by contour propagation for diagnostic and intraoperative MR-images of patients receiving MR-guided HDR prostate brachytherapy would be therefore of great interest. Furthermore, image registration would allow to monitor on-line the anatomy deformation (and therefore the accumulated dose) during the course of the intervention. Knowing the anatomy delineations and accumulated dose, the dose plan and needle insertion sequence can be updated during treatment with feedback on the anatomy position (cf. **chapter 6**). This registration tool should

have the ability to register images with different contrasts (when different MRI sequences are acquired) and to deal with transient structures entering or exiting the image field of view, such as needles or tissues from peristaltic movements: the image registration algorithm developed by Denis de Senneville *et al* (2016) can be a good candidate for this purpose. Second, the single needle robotic device which can support MRI-guided needle insertions should be up and running. For that, the performance of the robot must be assessed in the MRI room: In particular, the ability of the robot to insert accurately the needle to a pre-defined location must be assessed. Finally, a clinical protocol should be developed with the aim to perform the treatment using the MR-brachytherapy system.

CHAPTER 8

Samenvatting

In dit proefschrift worden nieuwe methodes ontwikkeld om het optimale dosisplan voor focale HDR prostaat brachytherapie met divergerende naaldconfiguratie te bepalen en om twee problemen op te lossen die daarbij kunnen optreden: fouten in het plaatsen van de naald en anatomische veranderingen. Ook werd een MR-compatibel systeem, gebaseerd op FBG sensoren, ontwikkeld waarmee de positie van een naald gemeten kan worden.

In **hoofdstuk 2** werd een snelle methode gepresenteerd om het optimale dosisplan voor focale HDR prostaat brachytherapie met divergerende naaldconfiguratie te berekenen. De voorgestelde optimalisatie-workflow omvat de bepaling van (1) de positie van het rotatiecentrum, (2) de naaldhoeken en (3) de dwelltijden. Anders dan bij de huidige meest gebruikte optimalisatiemethodes, is geen a priori keuze of aanpassing van invoerparameters zoals minimum of maximum dosis of gewichtsfactoren voor doelgebied en risico-organen nodig. Om deze optimalisatiemethode te testen werd een planningsstudie uitgevoerd met 10 patienten (met doelvolumes van 8.5cm3 tot 23.3cm3), waarbij 2 tot 14 naalden werden gebruikt. De totale rekentijd van de optimalisatie-workflow bedroeg minder dan 20 minuten ten tijde van publicatie van het manuscript in 2015. Klinisch acceptabele plannen werden bereikt met gemiddeld slechts 4 naalden. De rekentijd werd daarna verkort tot minder dan 5 minuten door de broncode te optimaliseren zonder dat het effect had op de resultaten. Met name het gebruik van het geheugen werd verbeterd: de dosis werd niet langer uitgerekend voor het gehele field of view van het MR beeld, maar alleen voor de relevante organen met enige marge, hetgeen het aantal bewerkingen significant reduceerde.

Echter, twee belangrijke gebeurtenissen kunnen de geplande dosisverdeling veranderen gedurende de interventie: fouten in het plaatsen van de naald en anatomische veranderingen. Daarom is het uiteindelijke doel een volledig automatisch systeem te ontwikkelen waarmee de dosisverdeling en de volgorde van naaldplaatsing opnieuw geoptimaliseerd worden tijdens de interventie met inachtneming van de twee hiervoor genoemde verstorende gebeurtenissen.

Hoofdstuk 3 is een stap in de richting van het uiteindelijke doel. Dit hoofdstuk presenteert een strategie om de dosis aan te passen met inachtneming van eerstgenoemde gebeurtenis: bij aanvang van de interventie wordt een dosisverdeling gepland, die vervolgens elke keer wordt aangepast na plaatsing van een naald om te compenseren voor eventuele fouten in de positie van de naald. Deze feedback-strategie werd getest op 8 patiënten met variërend aantal naalden (4 tot 12). Bij 97% van de simulaties was het aantal klinisch acceptabele plannen groter met feedback-strategie dan bij de simulaties zonder feedback-strategie. De rekentijd om het plan aan te passen na elke plaatsing van een naald was minder dan 100s waardoor de feedback strategie geschikt is voor intra-operatief gebruik.

De onzekerheden in de dosisverdeling als gevolg van fouten in de naaldposities kunnen op twee manieren verkleind worden: (1) fouten in de naaldposities zo veel mogelijk beperken en (2) de dosisverdeling dynamisch aanpassen met feedback van de werkelijke naaldposities zoals beschreven in **hoofdstuk 3**. Daarvoor

is de real-time bepaling van de naaldpositie noodzakelijk, ofwel de naald moet gevolgd worden (tracking) tijdens plaatsing en gereconstrueerd worden na plaatsing. Hiertoe werd een prototype systeem voor naald-tracking, gebaseerd op fiber Bragg gratings (FBG), onderzocht in **hoofdstuk 4**. Dit FBG sensing systeem bestaat uit een MR-compatibel stylet die drie optische fibers bevat met elk negen sets geïntegreerde FBG sensoren. De stylet kan in een brachytherapie-naald ingebracht worden waarna een snelle meting van de naaldafbuiging mogelijk is. Het doel van deze studie was om het FBG sensing systeem te beoordelen voor real-time naald (catheter, slangetje) tracking tijdens een MRI gestuurde interventie. Eerst werden de MR compatibiliteit en de nauwkeurigheid van het FBG sensing systeem beoordeeld. Verschillende bekende patronen van naaldafbuiging in een fantoom werden gemeten tijdens MR imaging. Daarna werd een naald-tracking procedure geïntroduceerd waarbij het FBG sensing systeem werd gebruikt. Voorafgaand aan de interventie werd een op MRI gebaseerde kalibratie van het FBG sensing systeem uitgevoerd, waarna het systeem geëvalueerd kon worden in een experiment met een bewegend fantoom tijdens MR imaging. De nauwkeurigheid van het FBG sensing systeem werd onderzocht door bekende vormen van naaldbuiging, de handmatig gesegmenteerde naalden op MRI en de op-FBG-gebaseerde metingen met elkaar te vergelijken. De resultaten lieten zien dat met de op op-FBG-gebaseerde naaldtracking procedure de positie van de gehele naald bepaald kan worden tijdens MR imaging, met een hogere nauwkeurigheid en precisie, hoger update-tempo en minder wachttijd vergeleken met de op MR gebaseerde naald lokalisatiemethodes. Daarbij, het update-tempo van de naaldpositie metingen is 100ms en de wachttijd 300ms. Dit systeem zou geschikt zijn voor MR gestuurde brachytherapie, met name voor een verbeterde naaldsturing en reconstructie.

In the strategie van dosisplanning met compensatie voor fouten in naaldpositie, zoals gepresenteerd in hoofdstuk 3, wordt de volgorde van tracks waarin de naald geplaatst wordt overgelaten aan de dokter en hoeft niet optimaal te zijn. Een programma dat de dokter helpt om de optimale volgorde van plaatsing van de naald te bepalen, zou daarom van groot belang zijn. Bovendien is het een stap in de richting van de ontwikkeling van een volledig automatisch besturingssysteem, waarmee het dosisplan en de volgorde van plaatsing van de naald steeds automatisch worden geoptimaliseerd tijdens de interventie. **Hoofdstuk 5** presenteert een nieuwe planningsmethode welke tot doel heeft om de volgorde van de plaatsing van de naald automatisch te updaten tijdens de interventie. De strategie is gebaseerd op de bepaling van de meest gevoelige track van de naald. De gevoeligheid van een naaldtrack is gedefinieerd als de invloed op de dosisverdeling in geval van suboptimale plaatsing. Hiertoe werd een stochastisch criterium opgesteld om voor elke naaldtrack de gevoeligheid te bepalen, die gebaseerd is op simulaties van het plaatsen van de naald. De voorgestelde strategie om de volgorde van de naaldtracks te bepalen werd gesimuleerd op 11 patiënten met een variërend aantal naaldtracks, waarbij voor elke naald de suboptimale positie werd gemodelleerd als typische toevallige hoekfouten. In 91% van de scenarios werd de dosisverdeling verbeterd als de naald in de meest gevoelige track werd geplaatst, vergeleken met plaatsing in de minst gevoelige track. De rekentijd om de optimale volgorde te bepalen was minder dan 6s per naaldtrack. De geïntroduceerde methode om de volgorde

van tracks te bepalen kan daarom bijdragen tot een optimale dosisafgifte in HDR prostaat brachytherapie.

In **hoofdstuk 6**, tenslotte, werd de tweede mogelijke verstoring aangepakt, namelijk de anatomische veranderingen. Uitganspunt bij deze studie was de MR compatibiliteit van het robotische systeem voor prostaatimplantaties, dat ontwikkeld wordt in het UMCU. Een nieuw model werd onderzocht, waarbij tijdens de interventie een update van dosisplan en naaldvolgorde plaatsvindt op basis van MR-feedback met betrekking tot anatomische veranderingen. De werking van dit zogenoemde MRI- brachytherapie hybride systeem werd geëvalueerd door MRI-gestuurde HDR prostaat brachytherapie interventies te simuleren voor 15 patiënten met variërend aantal naalden (2 tot 14), voor de situaties met en zonder herplanning tijdens de interventie. Anatomische veranderingen werden als volgt gesimuleerd: het plaatsen van een naald en het terugtrekken veroorzaakt (1) een translatie en (2) een rotatie van de prostaat en daarmee ook een verplaatsing van het doelgebied en de risico-organen tijdens de behandeling. Voor elke simulatie van een interventie werd met herplanning een hogere dosis in het PTV bereikt dan zonder herplanning. Met herplanning tijdens de interventie werd gemiddeld een klinisch acceptabel plan bereikt met 6 of meer naalden. Daarbij was het verschil tussen initiëele dosisparameters (berekend bij aanvang van de procedure) en de uiteindelijke dosisparameters gemiddeld kleiner dan 0.6%. Daarentegen nam zonder replanning de $D_{95\%\ PTV}$ gemiddeld 17.5% af bij toepassing van het translatiemodel en nam de $D_{10\%\ Ur}$ met gemiddeld 16.4% toe bij toepassing van het rotatiemodel. De verschillen in dosisverdeling namen toe met een toenemend aantal naalden. Met het MRI-brachytherapie hybride systeem en de beschreven strategie kunnen anatomische veranderingen in acht genomen worden zodat klinisch acceptabele dosisverdelingen verkregen kunnen worden.

Bibliography

Alterovitz R, Lessard E, Pouliot J, Hsu I-C J, O'Brien J F and Goldberg K 2006 Optimization of HDR brachytherapy dose distributions using linear programming with penalty costs *Med. Phys.* **33** 4012–20

Atalar E and Ménard C 2005 MR-guided interventions for prostate cancer *Magn. Reson. Imaging Clin. North Am.* **13** 491-504

Banerjee R, Park S J, Anderson E, Demanes J, Wang J and Kamrava M 2015 From whole gland to hemigland to ultra-focal high-dose-rate prostate brachytherapy: A dosimetric analysis *Brachytherapy* **14** 366-72

Bergeles C, Qin L, Vartholomeos P and Dupont P E 2012 Tracking and position control of an MRI-powered needle-insertion robot *Conf. Proc. IEEE Eng. Med. Biol. Soc.* 928–31

Beaulieu L, Carlsson Tedgren , Carrier J-F, Davis S D, Mourtada F, Rivard M J, Thomson R M, Verhaegen F, Wareing T A and Williamson J F 2012 Report of the task group 186 on model-based dose calculation methods in brachytherapy beyond the TG-43 formalism: current status and recommendations for clinical implementation *Med. Phys.* **39** 6208–36

Borot de Battisti M, Maenhout M, Denis de Senneville B, Hautvast G, Binnekamp D, Lagendijk J J W, Van Vulpen M and Moerland M A 2015 An automated optimization tool for high-dose-rate (HDR) prostate brachytherapy with divergent needle pattern *Phys. Med. Biol.* **60** 7567–83

Borot de Battisti M, Denis de Senneville B, Maenhout M, Hautvast G, Binnekamp D, Lagendijk J J W, Van Vulpen M and Moerland M A 2016a Adaptive planning strategy for high dose rate prostate brachytherapy - a simulation study on needle positioning errors *Phys. Med. Biol.* **61** 2177-95

Borot de Battisti M, Denis de Senneville B, Maenhout M, Hautvast G, Binnekamp D, Lagendijk J J W, Van Vulpen M and Moerland M A 2016b Fiber Bragg gratings-based sensing for real-time needle tracking during MR-guided brachytherapy *Med. Phys.* **43** 5288–97

Borot de Battisti M, Denis de Senneville B, Hautvast G, Binnekamp D, Lagendijk

J J W, Maenhout M, Moerland M A 2017 A novel adaptive needle insertion sequencing for robotic, single needle MR-guided high-dose-rate prostate brachytherapy *Phys. Med. Biol.* **62** 4031-45

Boutaleb S, Racine E, Fillion O, Bonillas A, Hautvast G, Binnekamp D, and Beaulieu L 2015 Performance and suitability assessment of a real-time 3D electromagnetic needle tracking system for interstitial brachytherapy *J. Contemp. Brachytherapy* **7** 280-9

Boyea G, Antonucci J, Wallace M, Ghilezan M, Gustafson G, Chen P Y, Saputo K, Flynn C and Martinez A 2007 The Role of Needle Trauma in the Development of Urinary Toxicity Following Prostate High Dose Rate (HDR) Brachytherapy *Int. J. Radiat. Oncol. Biol. Phys.* **69** 357–8

Cengiz M, Grdalli S, Selek U, Yildiz F, Saglam Y, Özyar E, and Atahan I L 2008 Effect of bladder distension on dose distribution of intracavitary brachytherapy for cervical cancer: Three-dimensional computed tomography plan evaluation *Int. J. Radiat. Oncol., Biol., Phys.* **70** 464-8

Chin J, Rumble R B, Kollmeier M, Heath E, Efstathiou J, Dorff T, Berman B, Feifer A, Jacques A and Loblaw D A 2017 Brachytherapy for Patients With Prostate Cancer: American Society of Clinical Oncology/Cancer Care Ontario Joint Guideline Update *J. Clin. Oncol.* **35** 1737–43

Cunha J A , Hsu I C, Pouliot J, Roach M III, Shinoharab K, Kurhanewicz J, Reed G and Stoianovici D 2010 Toward adaptive stereotactic robotic brachytherapy for prostate cancer: Demonstration of an adaptive workflow incorporating inverse planning and an MR stealth robot *Minimal. Invasiv. Ther.* **19** 189–202

Daanen V, Gastaldo J, Giraud JY, Fourneret P, Descotes JL, Bolla M, Collomb D, Troccaz J 2006 MRI/TRUS data fusion for brachytherapy *Int J Med Robot.* **2** 256–61

Damato A L, Viswanathan A N, Don S M, Hansen J L, and Cormack R A 2014 A system to use electromagnetic tracking for the quality assurance of brachytherapy catheter digitization *Med. Phys.* **41** 101702

Damato A L and Viswanathan A N 2015 Magnetic resonance-guided gynecologic brachytherapy *Magn. Reson. Imaging Clin. North Am.* **23** 633-42

Daskalov G M, Lffler E and Williamson J F 1998 Monte Carlo-aided dosimetry of a new high dose-rate brachytherapy source *Med. Phys.* **25** 2200–8

de Oliveira A, Rauschenberg J, Beyersdorff D, Semmler W, and Bock M 2008 Automatic passive tracking of an endorectal prostate biopsy device using phase-only cross-correlation *Magn. Reson. Med.* **59** 1043-50

Denis de Senneville B, Zachiu C, Ries M and Moonen C 2016 EVolution: an edge-based variational method for non-rigid multi-modal image registration *Phys. Med. Biol.* **61** 7377–96

DiMaio S P, Pieper S, Chinzei K, Hata N, Haker S J, Kacher D F, Fichtinger G, Tempany C M and Kikinis R 2007 Robot-assisted needle placement in open MRI: system architecture, integration and validation *Comput. Aided Surg.* **12** 15–24

Dimopoulos J C, Petrow P, Tanderup K, Petric P, Berger D, Kirisits C, Pedersen E M, van Limbergen E, Haie-Meder C, and Pötter R 2012 Recommendations from gynaecological (GYN) GEC-ESTRO working group (IV): Basic principles and parameters for MR imaging within the frame of image based adaptive cervix cancer brachytherapy *Radiother. Oncol.* **103** 113-22

Dinkla A M, van der Laarse R, Kaljouw E, Pieters B R, Koedooder K, van Wieringen N and Bel A A 2014 Comparison of inverse optimization algorithms for HDR/PDR prostate brachytherapy treatment planning *Brachytherapy* **14** 279-88

Ferlay J, Soerjomataram I, Dikshit R, Eser S, Mathers C, Rebelo M, Parkin D M, Forman D and Bray F 2015 Cancer incidence and mortality worldwide: sources, methods and major patterns in GLOBOCAN 2012 *Int. J. Cancer* **136** E359-86

Fischer G, DiMaio S, Iordachita I and Fichtinger G 2007 Robotic Assistant for Transperineal Prostate Interventions in 3T Closed MRI *Med. Image Comput. Assist. Interv.* **4791** 425–33

Fischer G S, Iordachita I, Csoma C, Tokuda J, DiMaio S P, Tempany C M, Hata N and Fichtinger G 2008 MRI-Compatible Pneumatic Robot for Transperineal Prostate Needle Placement *Mechatronics* **13** 295–305

Goldman S P, Turnbull D, Johnson C, Chen J Z and Battista J J 2009 Real-time fast inverse dose optimization for image guided adaptive radiation therapy enhancements to fast inverse dose optimization (FIDO) *J. Appl. Phys.* **105** 102008

Goldman S P, Chen J Z and Battista J J 2005 Feasibility of a fast inverse dose optimization algorithm for IMRT via matrix inversion without negative beamlet intensities *Med. Phys.* **58** 1041–57

Gorissen B L, den Hertog D and Hoffmann A L 2013 Mixed integer programming improves comprehensibility and plan quality in inverse optimization of prostate HDR brachytherapy *Phys. Med. Biol.* **58** 1041–57

Groenendaal G, Moman M R, Korporaal J G, van Diest P J, van Vulpen M, Philippens M E P and van der Heide U A 2010 Validation of functional

imaging with pathology for tumor delineation in the prostate *Radiother. Oncol.* **94** 145–50

Guedea F, Venselaar J, Hoskin P, Hellebust T P, Peiffert D, Londres B, Ventura M, Mazeron J-J, Van Limbergen E and Pötter R 2010 Patterns of care for brachytherapy in Europe: updated results *Radiother. Oncol.* **97** 514–20

Hauswald H, Kamrava M R, Fallon J M, Wang P C, Park S J, Van T, Borja L, Steinberg M L and Demanes D J 2016 High-dose-rate monotherapy for localized prostate cancer: 10-year results *Int. J. Radiat. Oncol. Biol. Phys.* **94** 667–74

Henken K R, Dankelman J, van den Dobbelsteen J J, Cheng L K and van der Heiden M S 2014 Error analysis of FBG-based shape sensors for medical needle tracking *IEEE/ASME Trans. Mechatronics* **19** 1523–31

Henry A M, Al-Qaisieh B, Gould K, Bownes P, Smith J, Carey B, Bottomley D and Ash D 2010 Outcomes Following Iodine-125 Monotherapy for Localized Prostate Cancer: The Results of Leeds 10-Year Single-Center Brachytherapy Experience *Int. J. Radiat. Oncol. Biol. Phys.* **76** 50–6

Hinnen K A, Battermann J J, van Roermund J G, Moerland M A, Jrgenliemk-Schulz I M, Frank S J and van Vulpen M 2010 Long-term biochemical and survival outcome of 921 patients treated with I-125 permanent prostate brachytherapy *Radiother. Oncol.* **94** 145–50

Holm Å, Carlsson Tedgren Å and Larsson T 2013 Heuristics for integrated optimization of catheter positioning and dwell time distribution in prostate HDR brachytherapy *Ann. Oper. Res.* **236** 319-39

Hoskin P J, Bownes P J, Ostler P, Walker K, and Bryant L 2003 High dose rate afterloading brachytherapy for prostate cancer: Catheter and gland movement between fractions *Radiother. Oncol.* **68** 285-8

Hoskin P J, Colombo A, Henry A, Niehoff P, Hellebust T P, Siebert F-A and Kovács G 2013 GEC/ESTRO recommendations on high dose rate afterloading brachytherapy for localised prostate cancer: an update *Radiother. Oncol.* **107** 325-32

Hoskin P, Rojas A, Ostler P, Hugues R, Alonzi R, Lowe G and Bryant L 2014 High-dose-rate brachytherapy alone given as two or one fraction to patients for locally advanced prostate cancer: Acute toxicity *Radiother. Oncol.* **110** 268–71

Hsu I, Lessard E, Weinberg V and Pouliot J 2004 Comparison of inverse planning simulated annealing and geometrical optimization for prostate high-dose-rate brachytherapy *Brachytherapy* **3** 147–52

Hung J, Shen S, De Los Santos J F, and Kim R Y 2012 Image-based 3D treatment planning for vaginal cylinder brachytherapy: Dosimetric effects of bladder filling on organs at risk *Int. J. Radiat. Oncol., Biol., Phys.* **83** 980-5

Kaya M, Senel E, Ahmad A, Orhan O, and Bebek O Real-time needle tip localization in 2D ultrasound images for robotic biopsies *International Conference on Advanced Robotics (ICAR) (IEEE, Istanbul, Turkey, 2015)* 47-52

Karabis A, Giannouli S and Baltas D 2005 HIPO: A hybrid inverse treatment planning optimization algorithm in HDR brachytherapy *Radiother. Oncol.* **76** 29

Karabis A, Belotti P and Baltas D 2009 Optimization of Catheter Position and Dwell Time in Prostate HDR Brachytherapy using HIPO and Linear Programming *World Congress on Medical Physics and Biomedical Engineering (Germany); IFMBE Proc.* **25** 612–5

Kirisits C, Rivard M J, Baltas D, Ballester F, Brabandere M D, van der Laarse R, Niatsetski Y, Papagiannis P, Hellebust T P, Perez-Calatayud J, Tanderup K, Venselaar J L, and Siebert F-A 2014 Review of clinical brachytherapy uncertainties: Analysis guidelines of GEC-ESTRO and the AAPM *Radiother. Oncol.* **110** 199-212

Kolkman-Deurloo I K K, Visser A G, Niël C G J H, Driver N and Levendag P C 1994 Optimization of interstitial volume implants *Radiother. Oncol.* **31** 229–39

Kron T, Eyles D, Schreiner J L, Battista J 2006 Magnetic resonance imaging for adaptive cobalt tomotherapy: A proposal *J. Med. Phys.* **31** 242–54

Labanaris A P, Engelhard K, Zugor V, Ntzel R, Khn R 2010 Prostate cancer detection using an extended prostate biopsy schema in combination with additional targeted cores from suspicious images in conventional and functional endorectal magnetic resonance imaging of the prostate *Prostate Cancer Prostatic Dis.* **13** 65–70

Lagerburg V, Moerland M A, Lagendijk J J W and Battermann J J 2005 Measurement of prostate rotation during insertion of needles for brachytherapy *Radiother. Oncol.* **77** 318–23

Lagerburg E, Moerland M A, van Vulpen M and Lagendijk J J W A 2006 A new robotic needle insertion method to minimise attendant prostate motion *Radiother. Oncol.* **80** 73–7

Lamey M, Burke B, Blosser E, Rathee S, De Zanche N, Fallone B G 2010 Radio frequency shielding for a linac-MRI system *Phys. Med. Biol.* **55** 995–1006

Lessard E and Pouliot J 2001 Inverse planning anatomy-based dose optimization

for HDR-brachytherapy of the prostate using fast simulated annealing algorithm and dedicated objective function *Med. Phys.* **28** 773–79

Lindegaard J C, Fokdal L U, Nielsen S K, Juul-Christensen J, Tanderup K 2013 MRI-guided adaptive radiotherapy in locally advanced cervical cancer from a Nordic perspective *Acta. Oncol.* **52** 1510–9

Loeb S, Bjurlin M A, Nicholson J, Tammela T L, Penson D F, Carter H B, Carroll P, and Etzioni R 2014 Overdiagnosis and Overtreatment of Prostate Cancer, *J. Natl. Cancer Inst.*, **95** 868–78

Ménard C, Susil R C, Choyke P, Gustafson G S, Kammerer W, Ning H, Miller R W, Ullman K L, Sears Crouse N, Smith S, Lessard E, Pouliot J, Wright V, McVeigh E, Coleman C N and Camphausen K 2004 MRI-guided HDR prostate brachytherapy in standard 1.5T scanner *Int. J. Radiat. Oncol. Biol. Phys.* **59** 1414–23

Morton G C and Hoskin P J 2013 Brachytherapy: current status and future stategies – Can high dose rate replace low dose rate and external beam radiotherapy? *Clin. Oncol.* **25** 474–82

Muntener M, Patriciu A, Petrisor D, Mazilu D, Bagga H, Kavoussi L, Cleary K, Stoianovici D 2006 Magnetic resonance imaging compatible robotic system for fully automated brachytherapy seed placement *Urology* **68** 1313–17

Nath R, Anderson L L, Luxton G, Weaver K A, Williamson J F and Meigooni A S 1995 Dosimetry of interstitial brachytherapy sources: Recommendations of the AAPM Radiation Therapy Committee Task Group No. 43 *Med. Phys.* **22** 209–34

Park Y L, Elayaperumal S, Daniel B, Ryu S C, Shin M, Savall J, Black R J, Moslehi B, and Cutkosky M R 2010 Real-time estimation of 3-D needle shape and deflection for MRI-guided interventions *IEEE/ASME Trans. Mechatronics* **15** 906-15

Pieters B R, de Back D Z, Koning C C E and Zwinderman A H 2009 Comparison of three radiotherapy modalities on biochemical control and overall survival for the treatment of prostate cancer: A systematic review *Radiother. Oncol.* **93** 168–73

Podder T K, Beaulieu L, Caldwell B, Cormack R A, Crass J B, Dicker A P, Fenster A, Fichtinger G, Meltsner M A, Moerland M A, Nath R, Rivard M J, Salcudean T, Song D Y, Thomadsen B R and Yu Y 2014 AAPM and GEC-ESTRO guidelines for image-guided robotic brachytherapy: Report of Task Group 192 *Med. Phys.* **41** 101501

Polders D L, Steggerda M, van Herk M, Nichol K, Witteveen T, Moonen L,Nijkamp J and van der Heide 2015 U A Establishing implantation uncertainties for

focal brachytherapy with I-125 seeds for the treatment of localized prostate cancer *Acta Oncol.* **83** 1-8

Popescu T, Kacs A C, Pisla D, Kacs G 2015 Brachytherapy next generation: robotic systems *J. Contemp. Brachytherapy* **7** 510–4

Pötter R 2009 Image-guided brachytherapy sets benchmarks in advanced radiotherapy *Radiother. Oncol.* **91** 141-6

Pötter R, Haie-Meder C, Van Limbergen E, Barillot I, De Brabandere M, Dimopoulos J, Dumas I, Erickson B, Lang S, Nulens A, Petrow P, Rownd J, Kirisits C 2006 Recommendations from gynaecological (GYN) GEC ESTRO working group (II): Concepts and terms in 3D image-based treatment planning in cervix cancer brachytherapy3D dose volume parameters and aspects of 3D image-based anatomy, radiation physics, radiobiology *Radiother. Oncol.* **78** 67–77

Pötter R, Georg P, Dimopoulos J C A, Grimm M, Berger B, Nesvacil N, Georg D, Schmid M P, Reinthaller A, Sturdza A, Kirisits C 2011 Clinical outcome of protocol based image (MRI) guided adaptive brachytherapy combined with 3D conformal radiotherapy with or without chemotherapy in patients with locally advanced cervical cancer *Radiother. Oncol.* **100** 116–23

Poulin E, Fekete C C, Ltourneau M, Fenster A, Pouliot J and Beaulieu L 2013 Adaptation of the CVT algorithm for catheter optimization in high dose rate brachytherapy *Med. Phys.* **40** 111724–9

Poulin E, Racine E, Binnekamp D, and Beaulieu L 2015 Fast, automatic, and accurate catheter reconstruction in HDR brachytherapy using an electromagnetic 3D tracking system *Med. Phys.* **42** 1227-32

Prada P J, Jimenez I, González-Suárez H, Fenández J, Cuervo-Arango C and Mendez L 2012 High-dose-rate interstitial brachytherapy as monotherapy in one fraction and transperineal hyaluronic acid injection into the perirectal fat for the treatment of favorable stage prostate cancer: Treatment description and preliminary results *Brachytherapy* **11** 105–10

Raaymakers B W, Lagendijk J J W, Overweg J, Kok J G M, Raaijmakers A J E, Kerkhof E M, van der Put R W, Meijsing I, Crijns S P M, Benedosso F, van Vulpen M, de Graaff C H W, Allen J, Brown K J 2009 Integrating a 1.5 T MRI scanner with a 6 MV accelerator: proof of concept *Phys. Med. Biol.* **54** 229–37

Rivard M J, Coursey B M, DeWerd L A, Hanson W F, Saiful Huq M, Ibbott G S, Mitch M G, Nath R and Williamson J F 2004 Update of AAPM Task Group No. 43 Report: A revised AAPM protocol for brachytherapy dose calculations *Med. Phys.* **31** 633–74

Roeloffzen E M, Battermann J J, van Deursen M J, Monninkhof E M, Visscher M I, Moerland M A and van Vulpen M 2011 Influence of dose on risk of acute urinary retention after iodine-125 prostate brachytherapy *Int. J. Radiat. Oncol. Biol. Phys.* **80** 1072–9

Roesthuis R J, Kemp M, van den Dobbelsteen J J, and Misra S 2014 Three-dimensional needle shape reconstruction using an array of fiber bragg grating sensors *IEEE/ASME Trans. Mechatronics* **19** 1115-26

Rogers C L, Alder S C, Rogers R L, Hopkins S A, Platt M L, Childs L C, Crouch R H, Roger S. Hansen and Hayes J K 2012 High dose brachytherapy as monotherapy for intermediate risk prostate cancer *J. Urol.* **187** 109-16

Siauw T, Cunha A, Berenson D, Atamtrk A, Hsu I, Goldberg K and Pouliot J 2012 NPIP: A skew line needle configuration optimization system for HDR brachytherapy *Med. Phys.* **39** 4339–46

Siegel R L, Miller K D and Jemal A 2017 Cancer statistics *CA Cancer J Clin.* **67** 7-30

Steggerda M J, van der Poel H G and Moonen L M F 2010 Minimizing the number of implantation needles for prostate ^{125}I brachytherapy: An investigation of possibilities and implications *Brachytherapy* **9** 319–27

Stone N N, Roy J, Hong S, Lo Y C and Stock R G 2002 Prostate gland motion and deformation caused by needle placement during brachytherapy *Brachytherapy* **1** 154–60

Stone N N and Stock R G 2002 Complications following permanent prostate brachytherapy *Eur. Urol.* **41** 427–33

Straßmann G, Olbert P, Hegele A, Richter D, Fokas E, Timmesfeld N, Hofmann R and Engenhart-Cabillic R 2011 Advantage of robotic needle placement on a prostate model in HDR brachytherapy *Strahlenther. Onkol.* **187** 367–72

van den Bosch M R, Moman M R, van Vulpen M, Batterman J J, Duiveman E, van Schelven L J, de Leeuw H, Lagendijk J J W and Moerland M A 2010 MRI-guided robotic system for transperineal prostate interventions: proof of principle *Phys. Med. Biol.* **55** 133–40

Vargas C, Ghilezan M, Hollander M, Gustafson G, Korman H, Gonzales J and Martinez A 2005 A new model using number of needles and Androgen deprivation to predict chronic urinary toxicity for high or low dose rate prostate brachytherapy *J. Urol.* **174** 882–7

Venselaar J, Meigooni A S, Baltas D, and Hoskin P J 2012 Comprehensive Brachytherapy: Physical and Clinical Aspects *Taylor & Francis, Washington*

Wang W, Viswanathan A N, Damato A L, Chen Y, Tse Z, Pan L, Tokuda J,

Seethamraju R T, Dumoulin C L, Schmidt E J, and Cormack R A 2015 Evaluation of an active magnetic resonance tracking system for interstitial brachytherapy *Med. Phys.* **42** 7114-21

Zelefsky M J, Kuban D A, Levy L B, Potters L, Beyer D C, Blasko J C, Moran B J, Ciezki J P, Zietman A L, Pisansky T M, Elshaikh M and Horwitz E M 2007 Multi-institutional analysis of long-term outcome for stages T1T2 prostate cancer treated with permanent seed implantation *Int. J. Radiat. Oncol. Biol. Phys.* **67** 327–33

Zhou J, Sebastian E, Mangona V, and Yan D Real-time catheter tracking for high-dose-rate prostate brachytherapy using an electromagnetic 3D-guidance device: A preliminary performance study *Med. Phys.* **40** 021716

List of publications

Published papers

Borot de Battisti M, Denis de Senneville B, Hautvast G, Binnekamp D, Lagendijk J J W, Maenhout M and Moerland M A 2017 A novel adaptive needle insertion sequencing for robotic, single needle MR-guided high-dose-rate prostate brachytherapy *Phys. Med. Biol.* **62** 4031-45

Maenhout M, van der Voort van Zyp J R N, **Borot de Battisti M**, Peters M, van Vulpen M, van den Bosch M and Moerland M A 2017 The effect of catheter displacement and anatomical variations on the dose distribution in MRI-guided focal HDR brachytherapy for prostate cancer *Brachytherapy in press*

Borot de Battisti M, Denis de Senneville B, Maenhout M, Hautvast G, Binnekamp D, Lagendijk J J W, Van Vulpen M and Moerland M A 2016 Fiber Bragg gratings-based sensing for real-time needle tracking during MR-guided brachytherapy *Med. Phys.* **43** 5288–97

Borot de Battisti M, Denis de Senneville B, Maenhout M, Hautvast G, Binnekamp D, Lagendijk J J W, Van Vulpen M and Moerland M A 2016 Adaptive planning strategy for high dose rate prostate brachytherapy - a simulation study on needle positioning errors *Phys. Med. Biol.* **61** 2177-95

Borot de Battisti M, Maenhout M, Denis de Senneville B, Hautvast G, Binnekamp D, Lagendijk J J W, Van Vulpen M and Moerland M A 2015 An automated optimization tool for high-dose-rate (HDR) prostate brachytherapy with divergent needle pattern *Phys. Med. Biol.* **60** 7567–83

Submitted paper

Borot de Battisti M, Denis de Senneville B, Lagendijk J J W, Hautvast G, Moerland M A 2017 A new methodology for planning adaptation on anatomy deformation during MR-guided HDR prostate brachytherapy *manuscript submitted to Phys. Med. Biol.*

Patent

Borot de Battisti M, Hautvast G L T F, Denis de Senneville B, Moerland M A, Maenhout M and Binnekamp D Device and method for assisting in a brachytherapy procedure, WO 2017037060 A1, filed on August 30, 2016

Invited talk

Borot de Battisti M A novel adaptive planning strategy for MR-guided focal HDR prostate brachytherapy *6th Annual International Conference in Computational Surgery in May 2016*

Abstracts and Conference proceedings

Borot de Battisti M, Denis de Senneville B, Peters M, Van der Voort van Zyp J, Lagendijk J J W and Moerland M A Automatic Contour Propagation for Diagnostic and Intraoperative MR-Images Acquired During MR-Guided HDR Prostate Brachytherapy *Oral communication at the AAPM Annual Meeting in July 2017*

Borot de Battisti M, Denis de Senneville B, Hautvast G, Binnekamp D, Lagendijk J J W, Peters M, Van der Voort van Zyp J, M Maenhout M and Moerland M A Toward adaptive MR-guided HDR prostate brachytherapy - Simulation study based on anatomy movements *Oral communication at the ESTRO 36 in May 2017*

Borot de Battisti M, Denis de Senneville B, Maenhout M, Hautvast G, Binnekamp D, Lagendijk J J W, Van Vulpen M and Moerland M A Assessment of fiber bragg grating (FBG)-based sensing for real-time needle tracking during MR-guided brachytherapy *Oral communication at the AAPM Annual Meeting in July 2016*

Borot de Battisti M, Denis de Senneville B, Maenhout M, Hautvast G, Binnekamp D, Lagendijk J J W, Van Vulpen M and Moerland M A Adaptive determination of needle sequence for HDR prostate brachytherapy with divergent needle-by-needle delivery *Campus presentation at the AAPM Annual Meeting in July 2016*

Borot de Battisti M, Denis de Senneville B, Maenhout M, Hautvast G, Binnekamp D, Lagendijk J J W, Van Vulpen M and Moerland M A MR compatibility of fiber optic sensing for real-time needle tracking *Oral communication at the ESTRO 35 in May 2016*

Maenhout M, Moerland M A, Van Vliet-van den Ende K M, Schokker R I, **Borot de Battisti M**, Peters M, van Vulpen M, Van der Voort van Zyp J R N MRI guided focal primary and (secondary) salvage HDR-BT in prostate

cancer patients seems safe, *Oral communication at the ESTRO 35 in May 2016*

Borot de Battisti M, Maenhout M, Denis de Senneville B, Hautvast G, Binnekamp D, Lagendijk J J W, Van Vulpen M and Moerland M A Automatic adaptive per-operative re-planning for HDR prostate brachytherapy - a Simulation Study On Errors in Needle Positioning *Oral communication at the AAPM Annual Meeting in July 2015*

Borot de Battisti M, Maenhout M, Denis de Senneville B, Hautvast G, Binnekamp D, Lagendijk J J W, Van Vulpen M and Moerland M A An automated optimization tool for HDR prostate brachytherapy with divergent needles *Poster discussion at the 3rd ESTRO Forum in May 2015*

Acknowledgments

First, I would like to thank my promotor, Jan Lagendijk, Professor in Radiotherapy Physics at the Department of Radiotherapy of the UMCU. Your comments on articles, abstracts and presentations were always fast, concise and useful. I am pleased to have participated in the development of MR-guided robotic HDR brachytherapy and hope it will be implemented in clinics very soon.

I wish also to thank my supervisor, Rien Moerland, Clinical Physicist at the Department of Radiotherapy of the UMCU. Rien, it was a pleasure to work with you during this three and a half years. It was quite a journey! You gave me a lot of freedom in my research which I really enjoyed. You also regularly provide some very useful critiques, which helped me to take some distance of my daily research. I learned a lot around you and hope we could continue to collaborate in the future. Moreover, thank you for your help for the dutch translation of this thesis summary, together with Ellis and Anna for the revision.

A big thanks to my second supervisor, Baudouin Denis de Senneville, Researcher CNRS, CR1 HDR, with the Mathematical Institute of Bordeaux and Imaging Therapy at the UMCU. I am very happy that we met at this time of my PhD project. I really enjoyed our extensive discussions which were very fruitful and always came up with new ideas and objectives. You gave me a lot of confidence in my research which I really appreciate. I really wish to continue our productive collaboration in the near future.

I am also very grateful to the committee members, Prof. dr. Borel Rinkes, Prof. dr. ir. Viergever, Prof. dr. de Jong, Prof. dr. Raaymakers and Prof. dr. van der Heide, for evaluating this PhD thesis.

I would like to acknowledge Philips Medical Systems Nederland B.V. for financially supporting this PhD program. More specifically, I thank all the Biomedical System team of Philips Group Innovation, and in particular Gilion Hautvast, Senior Scientist at Philips Group Innovation, Alfonso Isola, Senior Scientist at Philips Research, and Dirk Binnekamp, Principal Oncology Researcher at Philips Innovation Services, whose inputs greatly strengthen the research. Furthermore, the new technologies provided by Philips, such as the fiber optic and electro-magnetic systems for the tracking of brachytherapy needle, gave us the chance to develop new projects, which led to the publications of several articles, conference abstracts,

and also to the deposition of a patent filed in 2016.

My acknowledgments go also to the Medische Technologie & Klinische Fysica (MTKF) team of the UMCU, in particular to Leonard van Schelven, Clinical Physicist, Jeroen van den Berg, Instrumentmaker, and Menno Janssen, Intern, for their great contribution in the development and testing of the brachytherapy robot.

In the context of the STARLIT project, I would like to acknowledge Jeroen Schuurman and Yury Niatsetski, Development Managers at Nucletron (Elekta) for their contribution in the development of the robot clinical workflow.

Thank you also Metha Maenhout, PhD Candidate, Max Peters, Radiotherapy oncologist in training at the UMCU, Jochem van der Voort van Zyp, Radiotherapy oncologist at the UMCU and Marco van Vulpen, Senior Medical Director at Holland Particle Therapy Centre for their clinical inputs on the articles and conference abstracts.

I am also very glad to have met a lot of people and friends from all around the world during my PhD: Markus, Charis, Matteo, Tom, Jean-Paul, Ellis, Marc, Mariska, Saman, Kim, Robin, Stefan, Stan, Filipa, Cornel, Tristan, Marielle, Ana, Charlotte, Bjorn, Cyril, Matt, Chistopher, Dhabia, Anna, Soraya, Carl, Pim, Tim, Pascal, Stefano, João, Elena, Aisha and Anna. Our US roadtrips, sport sessions (tennis, skying, gym, squash, swimming, mountain biking, volleyball, climbing), lunches, dinners, drinks, parties, etc... were all quite memorable and I am looking forward for the next ones.

A big thanks also to my family (thank you Adeline for helping me to choose the image of the thesis cover!), my friends from France and abroad, and to Kasia, for always being supportive and positive.

Finally, I would like to acknowledge Nucletron (Elekta) and CIRS for financially supporting this thesis, and the ITEA (project 12026, SoRTS).

Curriculum vitae

Maxence Borot de Battisti was born in Échirolles (France) on November 1, 1988. Maxence obtained his scientific baccalauréat in 2005. Then, he followed 3 years of physics and chemistry preparatory classes to the Grandes Écoles at the Lycée Jean-Baptiste Say (Paris 16th, France) and the Lycée Louis-le-Grand (Paris 5th, France), leading to the entrance to the École Supérieure de Physique et de Chimie Industrielles de la ville de Paris (ESPCI) in 2008, and acquired the ESPCI engineering degree in 2013. During his cursus, Maxence worked for 6 months in 2011 as R&D intern at Schlumberger in Boston, MA (USA), focusing on the development of methods to prepare drill cuttings for petrophysical analysis by infrared spectroscopy and gas sorption. Moreover, Maxence integrated the Master program in Optics and Photonics at the Imperial College of London (UK) in 2012 where he was awarded with the Master of Science degree in 2013. For his Master thesis at Philips in Eindhoven (The Netherlands), he worked on the development of a method to monitor the bending of medical needle, based on optic fibers. He started a PhD in 2014 at the Department of Radiotherapy of the University Medical Center Utrecht (The Netherlands), partly funded by Philips, and worked on the development of adaptive planning strategies for MR-guided HDR prostate brachytherapy using a single needle MR-compatible robotic system. The results of his research are presented in this thesis.

Maxence is now working as lead system engineer at General Electric, on the development of ultrasound imaging probes.